

**ESTIMATING LITHOLOGY, METAMORPHIC GRADE &
INTENSITY OF HYDROTHERMAL ALTERATION USING
REMOTE SENSING AND GEOPHYSICAL DATASETS**

**APPLIED TO THE META-VOLCANIC ROCKS IN THE
EASTERN PILBARA CRATON, W. AUSTRALIA**

GHIDEY ZERESENAY MOSAZGHI
02, 2013

SUPERVISORS:

Dr. F.J.A. (Frank) Van Ruitenbeek

Drs. J.B. (Boudewijn) De Smeth



**ESTIMATING LITHOLOGY,
METAMORPHIC GRADE & INTENSITY
OF HYDROTHERMAL ALTERATION
USING REMOTE SENSING AND
GEOPHYSICAL DATASETS**

**APPLIED TO THE META-VOLCANIC
ROCKS IN THE EASTERN PILBARA
CRATON, W. AUSTRALIA**

GHIDEY ZERESENAY MOSAZGHI
Enschede, The Netherlands, 02, 2013

Thesis submitted to the Faculty of Geo-Information Science and Earth
Observation of the University of Twente in partial fulfilment of the
requirements for the degree of Master of Science in Geo-information Science
and Earth Observation.

Specialization: [Name course (e.g. Applied Earth Sciences)]

SUPERVISORS:

Dr. F.J.A. (Frank) Van Ruitenbeek

Drs. J.B. (Boudewijn) De Smeth

THESIS ASSESSMENT BOARD:

Prof. Dr. F.D. van der Meer (Chair)

Dr. P.M. (Paul) van Dijk (External Examiner, Twente University)

DISCLAIMER

This document describes work undertaken as part of a programme of study at the Faculty of Geo-Information Science and Earth Observation of the University of Twente. All views and opinions expressed therein remain the sole responsibility of the author, and do not necessarily represent those of the Faculty.

ABSTRACT

In this research ASTER satellite imagery, geochemical, airborne gamma-ray and magnetic datasets were used to estimate lithology, grade of metamorphism and intensity of hydrothermal alteration in three areas in the Eastern Pilbara Craton, W. Australia. The study areas consist mainly of mafic volcanic rocks of the East Pilbara Granite-Greenstone terrane in the Western Australia.

From the ASTER imagery band ratio values were extracted from each pixel along the traverses of the selected transects to check their variability. ASTER band combination, band 4, 6 and band 8 and the ASTER band combination of band ratio $(4+6)/5$ with band ratio $(5+7)/6$ and band ratio $(7+9)/8$ were found useful in determining lithology, the grade of metamorphism and intensity of hydrothermal alteration. Different band ratios gave different results depending on the mineralogical composition of individual rock units. Specific band ratios are sensitive to a specific alteration mineral present in the lithological unit. ASTER band ratio $(5+7)/6$ for example was sensitive muscovite and ASTER band ratio $(7+9)/8$ was sensitive to minerals such as hornblende, actinolite and Mg-chlorite which are present in the studied areas.

Gamma-ray Ternary image technique, potassium in red, thorium in green and uranium in blue was found useful in estimating lithology. Moreover different lithologies at different grades of metamorphism and intensity of hydrothermal alteration have different radioelement contents depending on their mineral composition.

Airborne magnetic data was analysed using techniques such as analytical signal, and the 1st vertical derivative of the total magnetic field data. The 1st vertical derivative was found suitable in detecting and mapping ultramafic rock units and banded iron formations which have relatively high magnetic mineral contents and therefore cause high amplitude magnetic anomalies. Different lithologies at different grades of metamorphism and intensity of hydrothermal alteration show different magnetic strength. Intensely hydrothermally altered rocks responded by causing long wavelength magnetic anomalies since the magnetic characteristics of these rocks and their mineral content is destroyed under intense, high temperature hydrothermal alteration processes (metasomatism).

Field data such as whole rock and trace element XRF data on 88 rock samples from the three areas, spectral mineralogy, legacy geological maps and reports associated to them as well as literature was used to compare, evaluate and validate the results found from the remote sensing and geophysical datasets. The integration of all this data allowed the successful delineation of geological units, to distinguish greenschist or amphibolitic metamorphic grade and to determine if serious hydrothermal alteration had affected the rocks in the three study areas.

ACKNOWLEDGEMENTS

First and for most, I would like to thank God the almighty for he provided me with sustaining grace and strength to accomplish my work successfully. Many thanks to the Netherlands Fellowship Program (NFP) for providing me with financial support needed to make this MSc a reality.

My special thanks goes to my supervisors Dr. F.J.A. (Frank) Van Ruitenbeek and Drs. J.B. (Boudewijn) De Smeth for their guidance, critical comments and suggestions which improved the scientific level of the research profoundly; it would not have been a success without them.

Thanks to all the staff members of the AES department for their generous help and all of my classmates and friends for sharing scientific ideas and knowledge in the whole study period at ITC.

My eternal gratitude goes to my family that words are not enough to express their love, support and motivation which contributed profoundly to my overall well-being and performance.

TABLE OF CONTENTS

1.	Introduction.....	1
1.1.	Research Background	1
1.2.	Problem definition	1
1.3.	Motivation.....	1
1.4.	Research Objectives	1
1.5.	Research Questions.....	2
1.6.	Hypothesis (assumption).....	2
1.7.	Datasets used.....	2
1.8.	Organization of the thesis chapters.....	3
2.	LITERATURE REVIEW.....	5
2.1.	Regional Geological Setting.....	5
2.2.	Geological setting of the Tectonic Units	5
2.2.1.	The East Pilbara Granite-Greenstone Terrane (EP).....	5
2.2.2.	Coonterunah Subgroup	6
2.2.3.	North Star Basalt Formation	6
2.2.4.	Mount Ada Basalt Formation.....	6
2.2.5.	Duffer Formation.....	7
2.2.6.	Apex Basalt Formation.....	7
2.2.7.	Panorama Formation	7
2.2.8.	Euro Basalt Formation	8
2.2.9.	Charteris Basalt Formation	8
2.3.	Metamorphism in the East Pilbara Granite–Greenstone Terrane	8
2.4.	Hydrothermal alteration associated with the Panorama Formation(District)	9
3.	METHODOLOGY.....	11
3.1.	Introduction	11
3.2.	Image pre-processing, enhancement and analysis	12
3.2.1.	ASTER Satellite Imagery.....	12
3.2.2.	Airborne Gamma-ray Image	13
3.2.3.	Airborne Magnetic Image	13
3.3.	Field data processing and analysis methods	13
3.3.1.	Magnetic Susceptibility data.....	13
3.3.2.	Alteration Indices and alteration box plots.....	14
3.3.3.	Oxides of major elements for lithological discrimination	14
4.	ANALYSIS RESULTS.....	15
4.1.	Coonterunah Formation	15
4.1.1.	Analysis results and interpretation of ASTER satellite imagery.....	15
4.1.2.	Gamma-ray ternary image for lithological discrimination.....	15
4.1.3.	Variability of airborne gamma-ray potassium contents	16
4.1.4.	Airborne magnetic data interpretation and analysis.	21
4.1.5.	Magnetic susceptibility data analysis	21
4.1.6.	Variations in SiO ₂ , K ₂ O and MgO content with lithology.....	22
4.1.7.	Alteration box plots for intensity of hydrothermal alteration	26
4.2.	Duffer Formation.....	26
4.2.1.	ASTER satellite imagery data analysis	26
4.2.2.	Gamma-ray ternary image for lithological discrimination.....	26
4.2.3.	Airborne magnetic data analysis	27
4.2.4.	Variability of ASTER band ratio results.....	27

4.2.5.	Variability of potassium contents	27
4.2.6.	Quantitative analysis of the airborne analytical signal data	30
4.2.7.	Variability of MgO and SiO ₂ content with lithology	34
4.2.8.	Alteration box plots the intensity of hydrothermal alteration	35
4.3.	The Panorama District	35
4.3.1.	ASTER satellite imagery data analysis	35
4.3.2.	Gamma-ray ternary image for lithological discrimination.....	36
4.3.3.	Airborne magnetic data analysis	36
4.3.4.	Alteration box plot	39
5.	DISCUSSION	41
5.1.	Introduction	41
5.2.	ASTER band ratios data interpretation.....	41
5.3.	Gamma-ray data interpretation.....	44
5.4.	Airborne magnetic data interpretation.....	47
6.	CONCLUSION AND RECOMMENDATIONS.....	49
6.1.	Conclusions	49
6.2.	Research limitations	50
6.3.	Recommmendations.....	51

LIST OF FIGURES

Figure 1: Location map of the study area	3
Figure 2: Methodology Flowchart.....	12
Figure 3: ASTER and airborne gamma-ray images.....	17
Figure 4: Variability of ASTER band ratio results	18
Figure 5: Variability of ASTER band ratio, radioelement & analytical signal.....	19
Figure 6: Variability of K contents	20
Figure 7: Comparison of airborne and ground K contents	20
Figure 8: Aeromagnetic images	23
Figure 9: variability of analytical signal of airborne magnetic data	24
Figure 10: Magnetic susceptibility variations with lithology	24
Figure 11: Comparison of ground and airborne magnetic datasets.....	25
Figure 12: Variations of selected major oxides with lithology.....	25
Figure 13: Alteration box plots for intensity of hydrothermal alteration	26
Figure 14: ASTER and airborne gamma-ray imageries	28
Figure 15: Aeromagnetic images	29
Figure 16: Variability of ASTER band ratio results	30
Figure 17: Variability of ASTER band ratio, radioelement & analytical signal.....	31
Figure 18: Variability of K contents.	31
Figure 19: Variations of selected major oxides with lithology.....	32
Figure 20: Comparison of airborne and ground K contents.....	32
Figure 21: variability of analytical signal of airborne magnetic data	33
Figure 22: Magnetic susceptibility variations with lithology	33
Figure 23: Comparison of ground and airborne magnetic datasets.....	34
Figure 24: Alteration box plots for intensity of hydrothermal alteration	35
Figure 25: ASTER and airborne gamma-ray imageries	37
Figure 26: Aeromagnetic images	38
Figure 27: Alteration box plots for intensity of hydrothermal alteration	39
Figure 28: Variability of ASTER band ratio values with lithology	42
Figure 29: Variability of ASTER band ratio values with metamorphic grade	43
Figure 30: Variability of ASTER band ratio values with intensity of hydrothermal alteration	44
Figure 31: Variability of K contents	46
Figure 32: Scatter plot for the comparison of ground and airborne K contents	47
Figure 33: Variability of the analytical signal of the total magnetic intensity data	47

1. INTRODUCTION

1.1. Research Background

The EP granite greenstone terrane has been well studied using conventional petrographic and geochemical methods because of the excellent exposure and preservation of the Archean rocks and their relationship with hydrothermal volcanogenic massive sulphide (VMS). However, conventional methods require huge investments, extended time and tremendous human labour. These costs can be reduced tremendously by using remote sensing and geophysical techniques prior to detailed mapping and sampling campaigns. ASTER satellite image analysis airborne gamma-ray survey and aeromagnetic surveys provide quick and cheap tools in geological mapping and mineral exploration.

Abweny (2012) used near infrared spectroscopic technique to discriminate between different lithologies, metamorphic grade and intensity of hydrothermal alteration; but his work was limited to rock samples and laboratory data and no remote sensing datasets were used.

1.2. Problem definition

Conventional geological and geochemical methods are cumbersome activities involving extensive field work, sample taking, chemical analysis and interpretation. Samples may be sparsely distributed over the study area; remote sensing technique offers a means to indirectly enhance the spatial density provided that a relationship with the primary data of mineralogy and geochemistry can be established. ASTER satellite imagery, airborne gamma-ray and aeromagnetic survey techniques are fast and cheap methods that have been used in geological mapping. In this study, these techniques will be tested for detecting and mapping the lithological composition, metamorphic grade and intensity of hydrothermal alteration. Results will solve the problem of cost and time. Moreover they will give the possibility of effective sampling plan where representative samples can then be taken for petrographic and chemical analysis.

1.3. Motivation

The motive to study this area is because of the presence of fractionated volcanic rock types from all ranges starting from felsic, intermediate to mafic. Testing if the respective remote sensing and geophysical techniques can be used to estimate lithology, metamorphic grade and relative intensity of hydrothermal alteration in such an environment gives a good understanding of geology and the above mentioned geological processes.

1.4. Research Objectives

The main objective of the research is to test the significance of ASTER (SWIR wavelength region) satellite imagery, airborne gamma-ray and airborne magnetic data to estimate lithological composition, metamorphic grade, and intensity of hydrothermal alteration of the volcanic rocks in the Eastern Pilbara (Western Australia) Granite Greenstone Terrane. The task will be accomplished by establishing a relationship between the analysis results obtained from these remote sensing and geophysical datasets. Analysis results will be compared with the results obtained from the whole rock litho-geochemistry and reflectance spectroscopy of rock samples.

Specific research objectives:

1. To extract information from the SWIR regions of ASTER satellite imagery related to variations in lithology, metamorphic grade and intensity of any hydrothermal alteration that exist in the meta-volcanic rocks in the Eastern Pilbara GGT terrane of Western Australia.
2. To relate airborne gamma-ray spectrometry signatures to the variations in lithological composition, metamorphic grade and intensity of hydrothermal alteration in the meta-volcanic rocks in the Eastern Pilbara GGT terrane of Western Australia.
3. To relate the signatures of the airborne magnetic data to variations in lithology, metamorphic grade and intensity of hydrothermal alteration of the meta-volcanic rocks in the Eastern Pilbara GGT terrane of Western Australia.
4. To compare and evaluate the results obtained from the analysis of ASTER satellite imagery, airborne gamma-ray data and airborne magnetic data with the results from the whole-rock major elements lithochemistry and spectroscopic results.

1.5. Research Questions

1. Which lithologies can be identified from the ASTER scenes of the study area? How do the reflectance characteristics of ASTER imagery vary with grade of metamorphism and intensity of hydrothermal alteration?
2. What geochemical trend can be observed from the airborne gamma-ray data and how do that relate to metamorphic grade and intensity of hydrothermal alteration?
3. Do the patterns manifested in the aeromagnetic data agree with the geological map of the study area? What is the response of airborne magnetic data varying lithological compositions? Is this also evident from the ground magnetic susceptibility data?
4. Do the results found from the ASTER satellite image data, airborne gamma-ray and airborne magnetic surveys agree with the ground spectroscopic results and results from whole rock geochemistry.

1.6. Hypothesis (assumption)

Mineralogy changes systematically according to lithology, metamorphic grade and hydrothermal alteration. These variations in mineralogy can be detected and mapped using ASTER satellite imagery, airborne gamma-ray and aeromagnetic datasets.

1.7. Datasets used

1. ASTER satellite imagery
2. Airborne gamma-ray data
3. Airborne magnetic data
4. Whole rock geochemistry data (XRF) on 88 rock samples

5. Spectral mineralogy of 88 rock samples
6. Magnetic susceptibility data on 37 rock samples (measured in ITC laboratory)
7. Legacy geological map (1:100,000 scale)
8. Literature

1.8. Organization of the thesis chapters

Chapter 1: Introduction

Chapter 2: Literature review

Chapter 3: Methodology

Chapter 4: Analysis results

Chapter 5: Discussion

Chapter 6: Conclusion and recommendations

Location Map of the study area

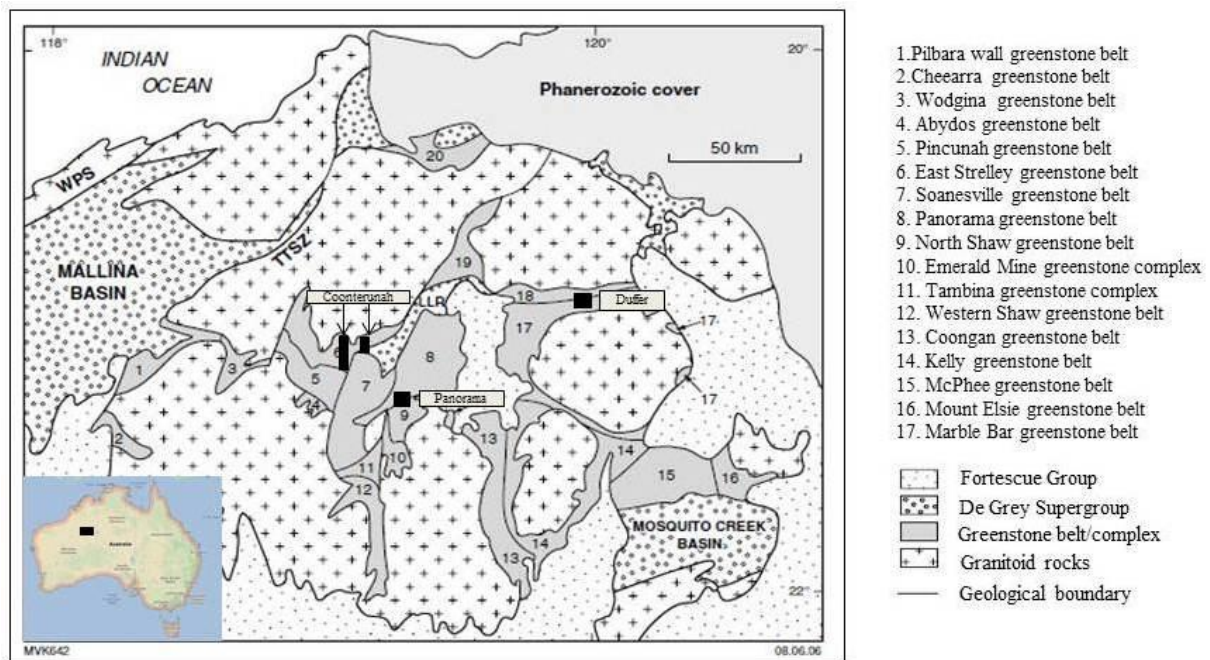


Figure 1: Location map of the study area, the black rectangles are the locations of the study areas. To the right of the map are the list of the greenstone belts and granitoid complexes present in the vicinity

2. LITERATURE REVIEW

2.1. Regional Geological Setting

The Pilbara Craton generally consists of the Archean (3655–2830 Ma) granite greenstone basement rocks and overlying Neoproterozoic to Palaeoproterozoic (2770–2400 Ma) (Trendall, 1990) of weakly deformed and metamorphosed (greenschist facies) successions of volcano-sedimentary rocks. It is divided into the East Pilbara Granite-Greenstone terrane (3.53–3.17 Ga), the West Pilbara Super-terrane (3.27–3.11 Ga), the Kurrana Terrane (3.2–2.93 Ga), Sholl Terrane and Karratha Terrane (Van Kranendonk, Smithies, et al., 2007). Each terrane has its own characteristic lithostratigraphy, structures, geochemistry and tectonic history (Van Kranendonk et al., 2006) and they are separated by intervening clastic sedimentary basins (Van Kranendonk et al., 2002). These five terranes are unconformably overlain by the (3.02 Ga–2.93 Ga) De Grey Supergroup (Hickman, 1990). The East Pilbara terrane and the West Pilbara Super-terrane were merged together at about 3.07 Ga whereas the Kurrana Terrane amalgamated with the East Pilbara Terrane at 2.905 Ga (Smithies et al., 2007).

The Pilbara Craton, provides an excellent exposure (an exposed area of about 183 000 km², from Blake (2001)) of low metamorphic grade, relatively undeformed rocks (Brauwart et al., 1998). The state of preservation, of the Pilbara craton has made it valuable for the investigation of Earth processes of all times (Cudahy et al., 2000).

Regardless of the intensive previous research work and advent of technology that improved the analytical capabilities in geochemistry and geochronology, there is still a debatable on the style of Archean tectonics. There are controversies on whether it operated in a similar way to modern style plate tectonics (the uniformitarian view, horizontal tectonics) or was basically different and was dominated by mantle plumes and recycling of primitive crust through drip tectonics (vertical tectonics) (Be´dard, 2006.; Cawood et al., 2006; Davies, 1995; de Wit, 1998.; Hamilton, 2003; Smithies et al., 2003; Stern, 2005; Van Kranendonk, 2004a). In an attempt to resolve this, Van Kranendonk, Hugh Smithies, et al. (2007) have proposed that a secular change from vertical-dominated to horizontal-dominated tectonic processes at c. 3.2 Ga and he proved that both processes included a component of their counterpart throughout the history of the crustal growth from 3.53 to 2.83 Ga.

2.2. Geological setting of the Tectonic Units

2.2.1. The East Pilbara Granite-Greenstone Terrane (EP)

Three main volcanic events (3515–3240 Ma) were responsible for the formation of the East Pilbara Granite-Greenstone Terrane (EP) (Van Kranendonk et al., 2002; Smithies et al., 2005b). The West Pilbara Super-terrane, and the Kurrana were juxtaposed against the EP by subduction–accretion processes from 3120–2930 Ma (Van Kranendonk, Smithies, et al., 2007). The sutures created by the juxtaposition event are buried under syn- to late-tectonic clastic basins, and the basins in turn are filled by the De Grey Supergroup (Van Kranendonk et al., 2002, 2004b; Smithies et al., 1999, 2005a). The EP contains the 3.525–3.165 Ga Pilbara Supergroup, the 3.72–3.6 Ga sialic basement, and five 3.500–3.165 Ga granitic supersuites (Van Kranendonk et al., 2006). The Pilbara Supergroup in turn comprises four autochthonous 3.52 and 3.20 Ga volcano-sedimentary units (Van Kranendonk et al., 2006). These sedimentary groups are the Warrawoona; Kelly; Sulphur Spring (Buick et al., 2002); and Soanesville. The supergroup with a maximum preserved thickness ~20 km. has no stratigraphic repetitions. The absence of stratigraphic repetitions have been proven by recent studies on the geological setting of the area and extensive sensitive high-resolution ion microprobe (SHRIMP) geochronology (Van Kranendonk et al., 2002). The lithological

units in the Pilbara Supergroup are dominated mainly by low- to medium-grade metamorphic grade (Van Kranendonk et al., 2006)

2.2.2. Coonterunah Subgroup

The 3.515 Ga Coonterunah Subgroup includes the Table top, the Coucal, the Double Bar and the Dresser Formation from bottom to top. The contact at its lower end is intruded by granitic rocks. In some places, the upper contact is unconformably overlain by the Kelly Group (Van Kranendonk, 2000); and in other places it is a disconformity with the younger Talga Talga or Coongan Subgroups. It occurs in the type locality of the East Strelley greenstone belt, and in this belt, the predominantly amphibolite- to greenschist-facies metabasalt reaches up to 6000 m in thickness (Green et al., 2000). The outcrops of the Coonterunah Formation are also present on the western limb of the Warralong greenstone belt (Van Kranendonk & Pirajno, 2004).

The Table Top Formation (AOt) is generally composed of fine-grained doleritic tholeiitic basalts. Rocks at the contact with the Carlindi Granitoid complex contain hornfels due to contact metamorphism. The hornfelsic contact metamorphic aureole extends up to 100m away from the granitoid complex. The Coucal Formation overlies conformably the Table Top Formation. Thick beds of banded iron formation (AOci) are present at the base of this Formation. Fine grained doleritic andesite and basalt (AOcbi) is present in the southern margin of the Carlindi Granitoid Complex and they mark the transition zone between the Table Top and the Coucal Formations. The felsic volcanic rocks (AOcf) of dacite and rhyolite were affected by metamorphic recrystallization. This was proved by the presence of Amygdales filled with carbonate and epidote after carbonate-sericite alteration in dacite of the felsic volcanic lithology. Plagioclase is altered to actinolite, carbonate and epidote. The Double Bar Formation (AOd) is composed of mainly fine-grained tholeiitic basalt and basaltic volcanoclastic rocks. The recrystallization of all of the mafic minerals present in the lithologies of this formation resulted in the metamorphic mineral assemblages of actinolite-chlorite-epidote.

2.2.3. North Star Basalt Formation

The North Star Basalt (Hickman, 1977) up to 2000m thick, consists mainly of pillowed and massive basalts, minor gabbro, and comprises a large number of mafic and ultramafic dykes. Geochemical studies have revealed that the upper part of the North Star Basalt comprises enriched tholeiitic basalts, probably due to contamination of the magmas by assimilation of crustal material. The lower contact is intruded by the Muccan Granitoid complex in the Warralong greenstone belts and it is intruded by the Mount Edgar Granitoid complexes in the Marble Bar greenstone belts. The McPhee Formation (in both Marble Bar and Warralong Greenstone Belts) and the Dresser Formation conformably overlay the North Star Basalt Formation. The grade of metamorphism in this Formation ranges from greenschist facies to lower amphibolite facies.

2.2.4. Mount Ada Basalt Formation

The 3.47 Ga Mount Ada Basalt Formation (Hickman, 1977) comprises a succession of pillow and massive basalt flows, dolerite sills, and minor thin chert units. 80% of the 2000 to 2500m thick Formation is composed of basalt. Chert, BIF and siltstone are present on the top of the Mount Ada Basalt and they wedge out south-westwards. It also contains two central bands of pelite, ferruginous chert and felsic tuff. The formation conformably overlies either the McPhee Formation or the Dresser Formation in different greenstone belts and is conformably overlain by the Duffer formation.

2.2.5. Duffer Formation

3.474-3.463 Ga Duffer Formation (Lipple, 1975) consists of predominantly dacitic lava, tuff and agglomerate, with subordinate rhyolite, basalt, chert and porphyritic intrusions. Feldspar-porphyritic subvolcanic intrusions are common. The base of the formation is marked by thinly-bedded, fine-grained felsic volcanoclastic rocks and coarse-grained phyric dacite-andesite sills. Pillowed andesitic basaltic rocks are metamorphosed at greenschist facies. It occurs in the EP block, from Salgash mining center through Marble Bar to Coppin Gap, and in the McPhee Creek, copper hills, and Glen Herring. Thickness and facies variations are a pronounced feature of the Duffer Formation (Hickman, 1983) and the maximum thickness is reached in the Marble Bar Greenstone Belt (4750m thick). The formation thins out moving from the Marble Bar and Coppin Gap towards north. A facies change is manifested in the Duffer Formation by its compositional variations where the thickest section is composed chiefly of agglomerate, but thinner sections generally contain a greater proportion of lava and tuff. The formation conformably overlies the Mount Ada Basalt Formation and is unconformably overlain by the younger formations.

2.2.6. Apex Basalt Formation

The apex basalt (Hickman, 1977) generally consists of tholeiitic pillow basalt, several thin members of grey and white banded chert, and sills of dolerite, gabbro and rare altered ultramafic rocks. The pillowed amygdaloidal and fine-grained tholeiitic and high-Mg basalt is about 2km thick and interlayered with meta-sedimentary rocks. It forms the lower part of the Salgash Subgroup and is about 2.5km thick. The Formation is located in the Marble Bar and Warralong greenstone belts. It is discordantly intruded by the Mount Edgar Granitoid Complex and as a result the rock units in this Formation are contact metamorphosed to low amphibolite facies. It unconformably overlies the Duffer Formation and is conformably overlain by the Panorama Formation or Euro Basalt Formation in the absence of the Panorama Formation. The formation generally is metamorphosed to a low-grade (greenschist facies) regional metamorphism except in the zone adjacent to the granitoid complex where it is of low amphibolite facies. The Apex Basalt Formation is dominated by of greenschist facies metamorphosed pillowed komatiitic basalt in the Warralong Greenstone Belt.

2.2.7. Panorama Formation

The Panorama Formation (Lipple, 1975) consist of a succession of metamorphosed felsic volcanoclastic rocks with agglomerate, silicified tuffaceous volcanoclastic rocks and minor volcanic breccia. The 3.458 to 3.426 Ga (VanKranendonk, 2006) which reaches up to a thickness of 2 km was erupted after the Mt. Ada ultramafic-mafic sequence and Apex Basalt. During the deposition of the Panorama formation, a high-temperature alteration (300°C) due to intense hydrothermal activity began and led to the formation of highly schistose and pyrophyllite-rich horizon. The rhyolitic Panorama Formation which forms the base of the Kelly greenstone belt has been extensively silicified (Cullers et al., 1993) and is intruded by the Corunna Downs Granitoid Complex. The formation structurally overlies the Apex Basalt and is overlain by the Strelley Pool Chert or unconformably by the Euro Basalt. Hydrothermal veins and dykes of black chert are found crosscutting the tuffaceous unit (AWpft) at the top of the Formation. These veins and dykes are said to be the feeders for the overlying Strelley Pool Chert. The Panorama Formation is about 800m thick in the Marble Bar greenstone belt and it rapidly thins out eastwards to less than 100m. The felsic unit (AWp) comprises of altered, siliceous, porphyritic and fine-grained rhyolite to dacite and tuffaceous rock units. The phenocrysts in the porphyritic felsic volcanic rocks are Quartz and altered feldspar whereas rutile, zircon, chlorite and leucosene are present as accessory minerals.

The formation is consisted of felsic volcanoclastic rocks with subordinate felsic lava and chert interbedded with andesitic basalt (AWpfa) in the McFee greenstone belt. In this belt sericite, carbonate, epidote and chlorite (after hornblende) are the main secondary minerals. In the Panorama greenstone belt, the Formation consists of massive, orange-weathering rhyolite unit (AWpr) at its base. The matrix of this unit under the microscope is finely recrystallized quartz and feldspar with sericite-altered plagioclase laths. The

Monzogranite laccolith in the North Pole Dome is syn-volcanic to the Panorama Formation and is believed to be the feeder.

2.2.8. Euro Basalt Formation

The Euro Basalt (Hickman, 1977) is mainly composed of tholeiitic and high-Mg basalt, mafic schist, amphibolite and dolerite (AWeb). The dolerite in this Formation is typically fine to medium grained, schistose to massive, and locally contains fine-grained magnetite and sulphides (Blewett & Champion, 2005). The 3.350-3.325 Ga Euro Basalt Formation conformably overlies the Strelley Pool Chert in the east Strelley, Panorama and North Shaw greenstone belts. It is also unconformably overlain by the Wymen Formation and the Gorge Creek and Fortescue Groups in the McPhee greenstone belt. The 9.4 km thick Euro Basalt Formation is intruded by the Yilgalong Granitoid Complex and is lithologically indistinguishable from the Apex Basalt Formation. It is less mafic than the Apex Basalt Formation and dolerite and gabbro sills are less common in this formation. In the southern part of the Camel Creek, spinifex textured basaltic rocks containing tremolite, chlorite, epidote and clinozoisite are dominant. The amphibolite in this Formation contains lenticular structures which seem to represent pillow structures but no clear evidence was found (Hickman, 1983).

2.2.9. Charteris Basalt Formation

The Charteris Basalt (Hickman, 1983) has a thickness of about 1 km. and it consists of pillowed komatiitic basalt and minor tholeiitic basalt (AWcbk). Moreover it consists of basalt interlayered with dolerite and minor komatiitic basalt (AWcbd). The komatiitic basalt commonly contains chlorite pseudomorphs after pyroxene. It outcrops both in the Charteris Creek on the eastern margin of the Kelly greenstone belt, and in the northern part of NULLAGINE. It overlies conformably the Wyman Formation and is unconformably overlain by the Budjan Creek Formation, Gorge Creek Group, and Fortescue Group. Petrographic and geochemical studies have revealed that the basalt in the Charteris Basalt Formation is similar that in the Euro Basalt Formation (Glikson & Hickman, 1981).

2.3. Metamorphism in the East Pilbara Granite–Greenstone Terrane

The grade of metamorphism in the East Pilbara Granite Greenstone Terrane (EPGGT) ranges from greenschist facies to amphibolite or hornblende-hornfels facies. The lithologies in this terrane which are metamorphosed at amphibolite facies are found near the base of the Warrawoona Group and basalt in this Group typically contains secondary actinolite, plagioclase (albite), chlorite, and quartz. Moreover the high-Mg basaltic rocks of the same Group commonly contain tremolite (pseudomorphs after pyroxene-spinifex texture), chlorite, and quartz assemblages that are characteristic of greenschist-facies metamorphism. Within about 1 km from the granitic complex contacts, basaltic rocks commonly contain hornblende–titanite–plagioclase–quartz assemblages, retrogressed in places to actinolite–epidote–albite–sericite; pelitic rocks locally contain biotite–garnet–muscovite. These assemblages are characteristic of the hornblende-hornfels facies (amphibolite facies) of contact metamorphism with retrogression to the albite–epidote-hornfels facies. The retrogression as well as Ar–Ar dating of metamorphic minerals in this area prove that contact metamorphism was a prolonged event (Davis et al., 1997).

Mafic and ultramafic xenoliths, rafts, and enclaves from the Warrawoona Group which are common in the central and northern parts of the Corunna Downs Granitoid Complex, typically contain clinopyroxene altered to chlorite, chlorite, rare brown hornblende, and plagioclase replaced by albite, clinozoisite or epidote. These mineral assemblages are typical of hornblende-hornfels (amphibolite facies) or slightly higher metamorphic facies (Turner, 1981). Widespread greenschist-facies metamorphism in this area is manifested by the presence of clinozoisite as well as epidote in the granitic rocks. Greenstones in the Coongan greenstone belt show evidence of two episodes of metamorphism. These include an early period of amphibolite-facies metamorphism, which Ar–Ar dating indicates may be as old as c. 3400 Ma, but is more likely to be 3240 ± 8 Ma (Davis et al., 1997). Greenschist-facies retrograde metamorphism,

overprinting shearing in the core of the Coongan greenstone belt, occurred at 3197 ± 44 Ma (Zegers et al., 1999) and 2941 ± 11 Ma (Davis et al., 1997).

2.4. Hydrothermal alteration associated with the Panorama Formation

An intense period of hydrothermal alteration occurred during or just after the deposition of Panorama Formation. This has happened following the deposition of Mt. Ada Basalt. This alteration event is represented by a highly schistose, intensely altered, golden brown pyrophyllite-rich horizon (Van Kranendonk & Pirajno, 2004). This horizon extends around the edge of the North Pilbara Dome (NPD) in the contact between the Mount Ada Basalt and Panorama Formation, in and adjacent to granite dykes radiating out from the North Pole Monzogranite. The hydrothermal event and the associated deformation that gave rise to the pyrophyllite schists in the Mt. Ada Basalt and Panorama Formation is older than the unconformably overlying Kelly Formation. This can be proven by the fact that the former have manifestations of pervasive schistosity and high temperature intense hydrothermal alteration which are not present in the Kelly Formation (Brown et al., 2006).

3. METHODOLOGY

3.1. Introduction

The present study deals with the use of remote sensing and geophysical data sets for the estimation of lithology, metamorphic grade and intensity of hydrothermal alteration. Whole rock lithochemistry, magnetic susceptibility data, spectral mineralogy, legacy geological maps and reports associated with them were used to compare, evaluate and validate the results from remotely sensed data and geophysical datasets.

Samples that were used in this study are 88 rock samples collected from traverses of three study areas namely, the Duffer formation, the Coonterunah subgroup and Panorama district. Samples from the Panorama district were intensely hydrothermally altered whereas the rest of the samples are all fresh. These intensely hydrothermally altered samples were included in order to be able estimate the intensity of hydrothermal alteration. The fresh samples were sampled in such a way that no visible veins or alteration minerals are included in the specimen. There is however some low degree of carbonate and silicification alteration in some of the mafic and ultra-mafic rock samples. More details about how samples were collected can be found from (Smithies et al., 2007). The hydrothermally altered samples from Panorama district are from the PhD work of Brauhart (1999) and Publications that were derived from it such as Brauhart et al. (1998) and Brauhart et al. (2001).

The analytical methods used to analyse the samples were as follows; XRF spectrometry was used to analyse major elements on fused disks. The precision of this analytical method is plus or minus 1%. XRF method using a pressed pellet was used to analyse trace elements like Ba, Cr, Cu, Ni, Sc, V, Zn, and Zr .Cs, Ga, Nb, Pb, Rb, Sr, Ta, Th, U, and Y. The REE were analysed by ICP-MS. Trace element precision was better than -10%. Gravimetry and electrochemical titration methods were used to determine the abundance of LOI and Fe²⁺ Concentration. In the case of the hydrothermally altered samples from the Panorama district care was taken that only un-weathered rocks were sampled. Major and trace element X-ray fluorescence (XRF) analyses were performed on fused disks and pressed pellets. Additional trace element analyses including Th were performed by inductively coupled plasma mass spectrometry(ICP-MS) (Brauhart et al., 2001)

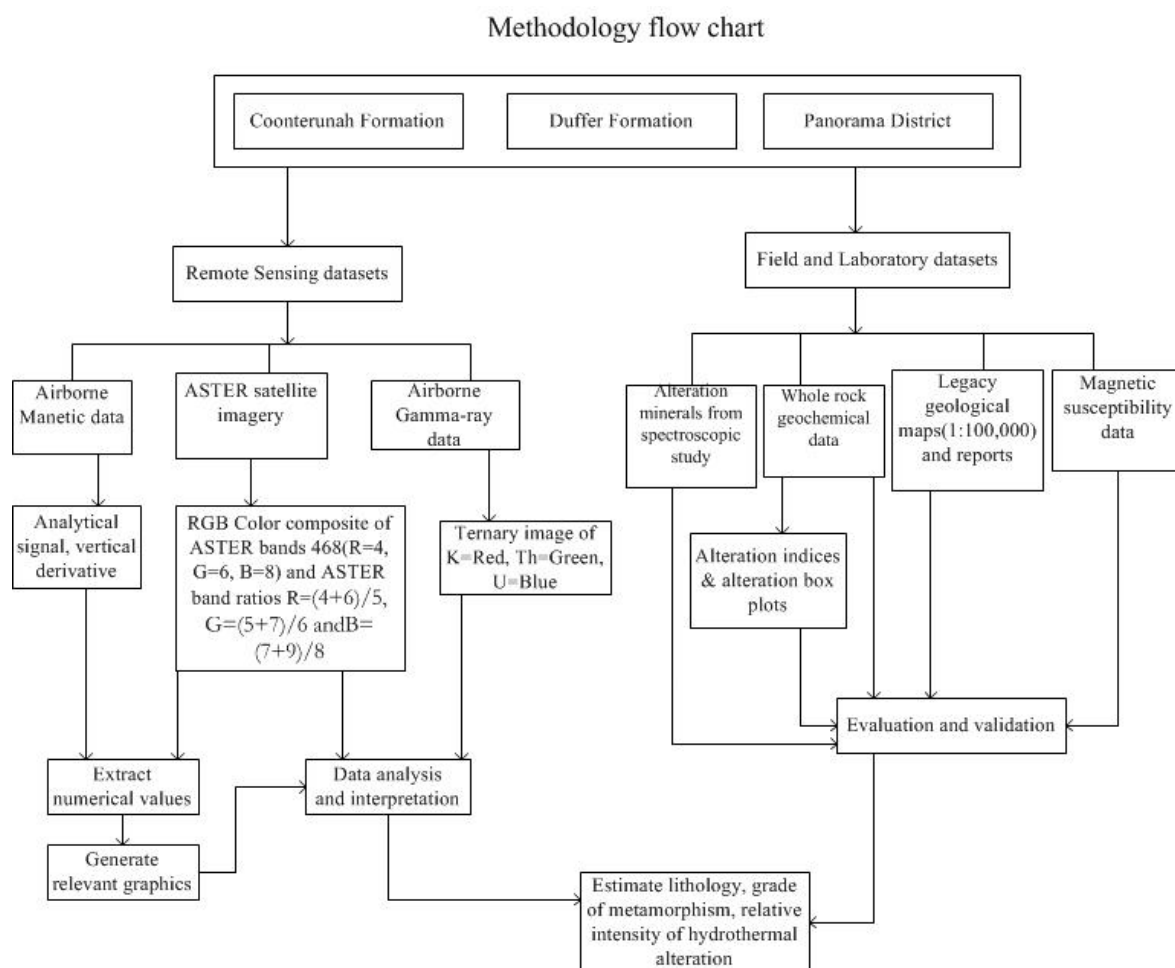


Figure 2 Methodology Flowchart

3.2. Image pre-processing, enhancement and analysis

3.2.1. ASTER Satellite Imagery

The satellite-borne, multispectral ASTER satellite imagery is cheap and easily accessible. The three VNIR spectral bands measure visible reflected radiation in the wavelength region between 0.52 and 0.86 μm , with 15m spatial resolution. In addition, ASTER records the data in band 3B (0.76–0.86 μm) in a backward looking mode so that digital elevation model (DEM) can be generated. The six SWIR spectral bands measure infrared reflected radiation in the wavelength region between 1.6 and 2.43 μm , with 30m spatial resolution. Moreover the five spectral bands (TIR) receive emitted radiation in the wavelength region between 8.125 and 11.65 μm , with 90m spatial resolution. ASTER data has created an opportunity for geological mapping including alteration products in addition to other applications (Gomez et al., 2005). The three VNIR bands are important in the identification of transition metals, especially iron and some rare-earth elements (REE). The six SWIR bands and the five TIR bands of the ASTER imagery are the most important bands in mineral identification. In this study, the six SWIR bands will be used.

Color composite image of band 4:6:8 (figure 3A) was used to identify the different lithological units in the study area. Moreover another color composite image of band ratios $(4+6)/5:(5+7)/6:(7+9)/8$ was also used to complement the above mentioned composite image. Band ratios were calculated using ENVI software with the band math functionality. Band ratio $(4+6)/5$ enhance the visibility of minerals such as alunite, kaolinite, and pyrophyllite. Band ratio $(5+7)/6$ represents sericite, muscovite, illite and smectite and band ratio $(7+9)/8$ enhances the prominence of minerals such as carbonate, chlorite and epidote (Gozzard, 2006).

The values of each pixel of all ASTER band ratios of selected transects were extracted and they were plotted against lithology and spectral mineralogy to see the compositional and mineralogical variations in each lithological unit.

3.2.2. Airborne Gamma-ray Image

Airborne gamma-ray survey was flown in 1996 in an east west flight line direction and a north south tie line direction with the sensor mounted in a boom attached to the rear of the aircraft. The flight line spacing is 400 m and the tie line spacing is 4000m. Exploranium gamma-ray spectrometer, incorporating two DET1024 crystal detectors with a total volume of 33.56 litres, was used to acquire the gamma-ray image data. The crystal gains were controlled by an Exploranium GR820 spectrum processor (Richardson, 1996).

The method provides estimates of apparent surface concentrations (to one foot depth) of, the most common naturally occurring radioactive elements, potassium (K), uranium (U) and thorium (Th) (Erdi-Krausz et al., 2003). The use of this method is based on the assumption that absolute and relative concentrations of these radioelements vary measurably and significantly with lithology (Kumar et al., 2008).

Ternary image (U in blue, Th in green, and K in red) was used to enhance the airborne gamma-ray image. Simplified geological outline was superimposed on the gamma-ray ternary image map to help to discriminate between different lithologies. Radioelement values of the gamma-ray image were extracted using spatial analyst tools functionality in ArcGIS and they were plotted against lithology and spectral mineralogy to see the corresponding mineralogical variability.

3.2.3. Airborne Magnetic Image

Airborne magnetic survey was also flown in an east west flight line direction and a north south tie line direction with the sensor mounted in a boom attached to the rear of the aircraft. The flight line spacing is 400 m and the tie line spacing is 4000m. The instrument used in this Campaign was G833 helium magnetometer with an operating range of 20,000 to 95,000 nT. The survey area covers the Marble Bar 1:250 000 map Sheet area which is bounded by the coordinate degrees of 118° 30' east and 21° 00' south, 120° 00' east and 21° 00' south, 120° 00' east and 22°00' south, 118° 30' east and 22°00' south (Richardson, 1996).

In general, variations in aeromagnetic image data are resulted from the contrast of magnetic properties between rock bodies (Reeves, 2005). This contrast arises due to the variations in the magnetic mineral content of rock units, such as magnetite, pyrrhotite, and titanohematite. Airborne magnetic data has reliably been used in mineral exploration and geological mapping since early 1960s. It can readily outline banded iron formations in greenstone belts, magnetite-rich granitoids and structural features such as large-scale folds, faults, and dykes (Parsons et al., 2006).

The total magnetic field of the airborne magnetic data was processed using Oasis montaj software to find the vertical derivative and the analytical signal. Rock types are best represented using the total field and vertical derivative of the magnetic data, whereas contacts between rock types are best defined using the horizontal derivative of the total magnetic field and the analytical signal. Unfortunately the horizontal gradient was not found useful for this research. Values of the analytical signal image was extracted and plotted against lithology and spectral mineralogy to figure out the mineralogical variability in different lithologies along respective transects.

3.3. Field data processing and analysis methods

3.3.1. Magnetic Susceptibility data.

Magnetic susceptibility data was collected from the three study areas and other transects which were not studied in this research; all in all magnetic susceptibility of 138 rock samples of which only 37

measurements were used was measured using SM-20 magnetic susceptibility meter. Two readings were taken for each rock sample for quality control. The airborne magnetic data values extracted from the pixels where sample points are located were compared to the magnetic susceptibility data values for evaluation and validation. Moreover the measured values were plotted against lithology and spectral mineral assemblages for evaluation and validation reasons.

3.3.2. Alteration Indices and alteration box plots

Alteration indices are multivariate numerical expressions that calculate the relative proportion between altered and unaltered components. This method uses major elements expressed as oxides, to characterize alteration halos around ore bodies and to determine the intensity of hydrothermal alteration Piche and Jebrak (2004). The enriched components are represented in the numerator whereas the depleted ones are represented in the denominator. VMS-type deposits generally can make use of many different types of alteration indices such as the Ishikawa index (AI) (Ishikawa et al., 1976), the CCPI (=chlorite, carbonate and pyrite index), Modified Hashimoto, chlorite, Alkali, Hashiguchi, Sericite, and Spitz etc. Ishikawa alteration index measures the intensity of chlorite and sericite alterations in Kuruko type VMS deposits (Kuruko type VMS deposits are deposits formed when an island arc collides with inter-arc basin in an ocean-ocean collision environment). CCPI alteration index measures the intensity of chlorite, carbonate and pyrite alterations. These two alteration indices are only valid for areas where the primary minerals that are involved in the original reactions were highly preserved and not for highly metamorphosed (deformed) rocks (Theart et al., 2011).

$$AI = \frac{\text{enriched}}{\text{enriched} + \text{depleted}} \times 100 \quad \quad CCPI = \frac{\text{enriched}}{\text{enriched} + \text{depleted}} \times 100$$

$$AI = \frac{(K_2O + MgO)}{(K_2O + MgO) + (Na_2O + CaO)} \times 100 \quad \quad CCPI = \frac{(MgO + FeO)}{(MgO + FeO) + (Na_2O + K_2O)} \times 100$$

Where enriched components considered in AI are K_2O and MgO whereas depleted minerals considered are $Na_2O + CaO$. In the case of CCPI, enriched components considered are MgO and FeO (In the case of Panorama district, Fe_2O_3 was provided and it was recalculated to FeO); whereas depleted minerals considered are $Na_2O + K_2O$.

Alteration box plots proposed by Large et al. (2001) were generated to separate hydrothermally altered and unaltered rock samples. These box plots show the CCPI alteration index on the y axis and AI alteration index on the x axis. Alteration box plots were plotted both with lithology and spectral mineralogy.

3.3.3. Oxides of major elements for lithological discrimination

The oxides of the major elements SiO_2 , K_2O and MgO are also good indicators of compositional variability between different lithologies. There for the values of this elements in weight% was plotted against lithology to assess the compositional variability of different lithologies in terms of this important oxides.

4. ANALYSIS RESULTS

4.1. Coonterunah Formation

4.1.1. Analysis results and interpretation of ASTER satellite imagery

Aster band combination 468 (R=4, G=6 & B=8, figure: 3A) was found useful in lithological discrimination. It clearly shows lithologies such as high Mg basalt (block A) which is the mainly light greenish unit with variegated reddish color. All the lithologies mentioned here are referred from legacy geological map (VanKranendonk, 2000) (figure: 3D). The reliability of the geological map was proven using lithologies from the petrographic classification of Smithies et al. (2007), for more details see appendix 2 and 5. The variegated green (block B, mainly green) and reddish unit is Tholeiitic basalt. The reddish unit (block C) is felsic volcanic lithology. Directly to the north of this unit (block D) which is dark greenish, locally interrupted by reddish felsic units ranges from andesite to basalt? The last lithological unit (block E) is the deep green unit which is meta-basalt, meta-dolerite and amphibolite.

The color composite image (figure: 3B) of ASTER band ratios ($R = (4+6)/5$, $G = (5+7)/6$ & $B = (7+9)/8$) also gave a good information on lithology and was used as a complementary image in addition to the color composite image of ASTER band combination 468 (R=4, G=6 & B=8, figure: 3A).

Different lithologies show different ASTER band ratio values. (Figure: 4) shows the variability ASTER band ratios $(4+6)/5$, $(5+7)/6$ and $(7+9)/8$ with lithology and alteration intensity. Strikingly deepest features for ASTER band ratio $(4+6)/5$ occur in the High Mg basalt and tholeiitic basalt and this is caused by the presence of less amount of muscovite as an alteration mineral due to metamorphism. This lithology is dominated by Fe-chlorite and intermediate chlorite mineral assemblages which are typical for greenschist facies of metamorphism. In the case of band ratio $(7+9)/8$, the deepest features occur in meta-basalt, meta-dolerite, and amphibolite. This is due to the abundance of the alteration minerals hornblende, Mg chlorite and actinolite in the respective lithologies. These alteration mineral assemblages in turn are associated to high metamorphic grade being amphibolite facies.

4.1.2. Gamma-ray ternary image for lithological discrimination

Close inspection of the ternary composite image (Figure: 3 C) in comparison to the geologic map ((Figure: 3 D)) reveals the following: The reddish unit (block A) which is mapped as high Mg basalt in the legacy geological is represented in a reddish color in this image. Even though the reddish color representation of this lithology helps to easily identify it from the rest of the lithologies; reddish color which means high potassium content is not expected from basaltic rocks. Basaltic rocks in nature contain very low amount of potassium which is 0.8% on average. The airborne gamma-ray potassium content of this lithology ranges from 0.85% up to 1.14%. The potassium content of rock samples from the same lithology from XRF laboratory analysis ranges from 0.09% to 0.7%. The laboratory result is in a good agreement with the average abundance of potassium in basaltic rocks in nature. Figure: 7 shows the comparison of XRF potassium contents with airborne gamma-ray potassium contents of the sampled lithologies. The clearly shows the exaggeration in the potassium content of the high Mg basalt and for the rest of the lithologies airborne gamma-ray potassium contents are in a good agreement with the ground measurements.

This shows that an error was introduced in to the airborne gamma-ray data in this lithology. The error could probably be an error from interpolation due to flight line spacing (400m) and direction (East West). Flight line spacing affects the signals received by the sensor in such a way that the survey lines were far from the target area and errors might have been introduced from interpolation. The negative effect of flight line direction is that the transect is north south and the flight line direction was east west. This flight line direction must have missed many of the samples along the transect and for that matter errors are introduced.

The meta-basalt, meta-dolerite, and Amphibolite (block E) is fairly clearly distinguishable from the rest of the rock units with a mixture of dark reddish, bluish and greenish colour reflecting relatively low

background concentration of the three radioelements. In fact this lithology contains the least amount of potassium in this transect. This least amount of potassium is clearly visible in the line plot (Figure 5) and box plot (Figure 6A). Block C (fig: 3C) can also be easily identified in the radioelement ternary map. This unit is mapped as felsic volcanic rocks from the geological map and it has got yellowish to light greenish colour reflecting the presence of thorium in a relatively higher amount than the rest of the radio elements. Block B shows red, blue and light green colors localized in patches indicating the presence of all the three radioelements in this block. The occurrence of the three radioelements in this unit is not homogeneous; hence no clear boundary can be distinguished. Block D is dominated by blue units, to a lesser extent light green and some faint brownish color. The blue color occurs when the radioelement contents are low and might represent noise in the data or errors due to radon at the surface. This also indicates the presence of the three radioelements unevenly distributed throughout the lithological unit. All the colors in this block are slightly darker in comparison to the adjacent block B indicating the presence of the three radioelements in relatively lesser amounts.

4.1.3. Variability of airborne gamma-ray potassium contents

Potassium, a volatile lithophile element in natural conditions, is the most important radioelement in identifying different rock types. Different rock types are characterized by different potassium concentrations. The average concentration of potassium in the Earth's upper crust being 2.33 wt. % most of it is contained in the alkali feldspar and micas in felsic rocks, mainly granitoids, which contain 3.5 wt. % K. Mafic and ultramafic rocks contain much lower concentrations, ranging from 0.58 to 0.75 wt. %. Almost all the potassium in metamorphic and magmatic rocks is contained in the feldspar mineral series, the feldspathoids leucite and nepheline, and the micas biotite and muscovite. Amphiboles in some cases contain up to 1 wt. % of potassium. (Erdi-Krausz et al., 2003).

Ultramafic rocks contain relatively less amount of K than just mafic rocks. This is manifested in figure 5; in this transect plot, variability of radioelement concentrations with lithology is very apparent and it decreases going from mafic rocks in the southern end of the transect to the ultramafic rocks in the northern end. Box plot (6A) also clearly shows the variability of potassium contents of with lithology. It also shows decreasing potassium content as we go from mafic to ultramafic rocks.

Figure 6B shows the variability of radioelement content with metamorphic mineral assemblages. It is apparent that rocks at different grades of metamorphism have different potassium contents. These different grades of metamorphism are represented by indicator mineral assemblages. Rocks at greenschist facies of metamorphism are represented by Fe-chlorite and Intermediate chlorite in this transect and lithologies at the amphibolite facies of metamorphism are represented by metamorphic mineral assemblages such as Mg-chlorite, hornblende and to lesser extent actinolite.

Scatter plot (figure 7) comparing results from gamma-ray data with the results from XRF laboratory analysis (K from xrf was provided in the form of K_2O and it was recalculated to K) was generated to check the reliability of the values found from airborne magnetic data. The plot shows a similar trend of the values from both datasets of potassium except in the high magnesium basalt. The reason for this mismatch could be the consequence of flight line direction and or survey line spacing. The flight line direction is east west and the transect is north south, hence there is high probability that the survey lines didn't hit the target and errors arise due to interpolation. Similarly, survey lines are spaced 400m from each other and there is quite a large chance that the signal was not coming directly from the area of interest and the mismatch might have been caused due to errors from interpolation

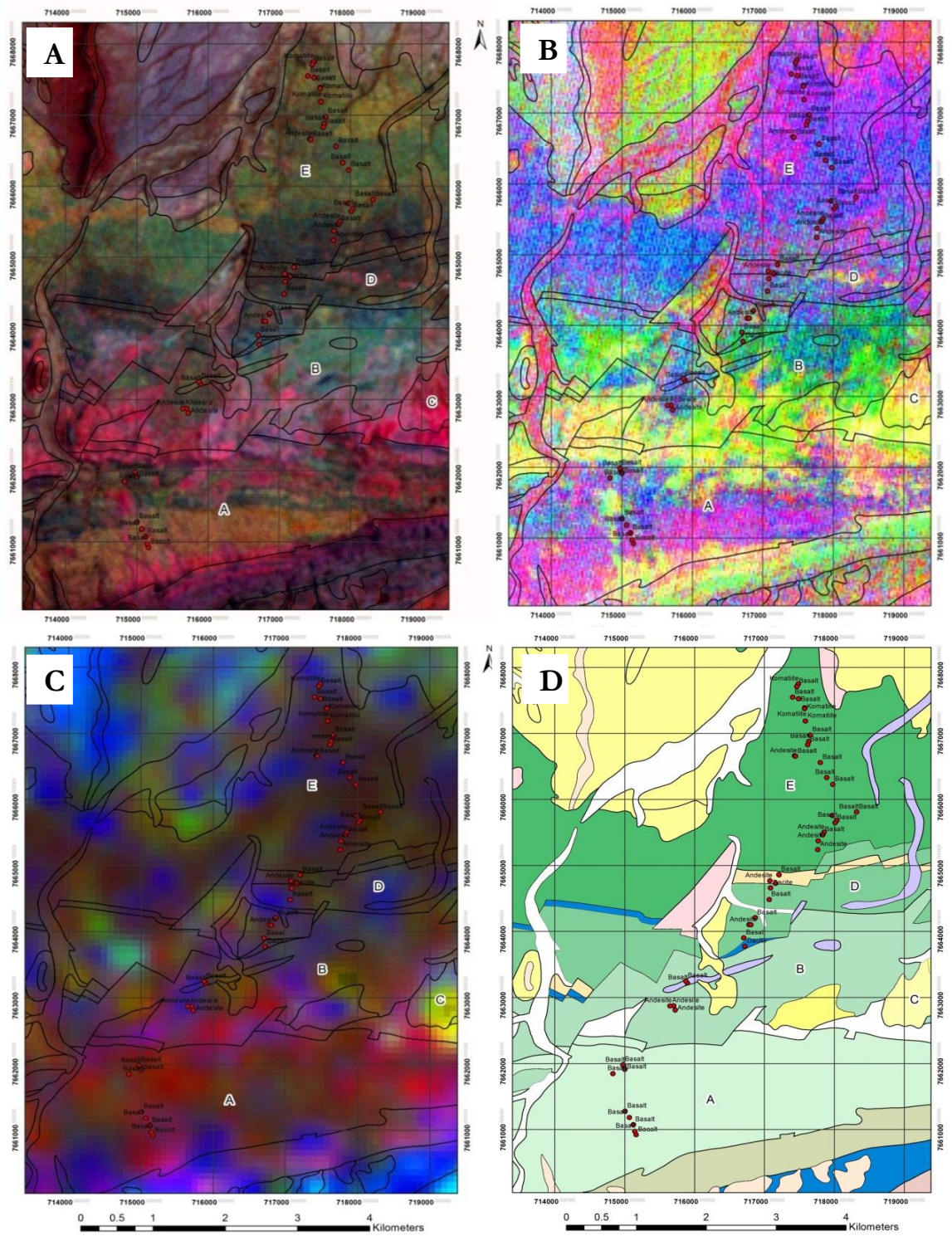


Figure 3: A: ASTER band combination 468(R=4, G=6, B=8). B: ASTER band ratio image R= (4+6)/5, G= (5+7)/6 and B= (7+9)/8. C: Gamma-ray ternary image R=K, G=Th, B=U. D: Legacy geological map

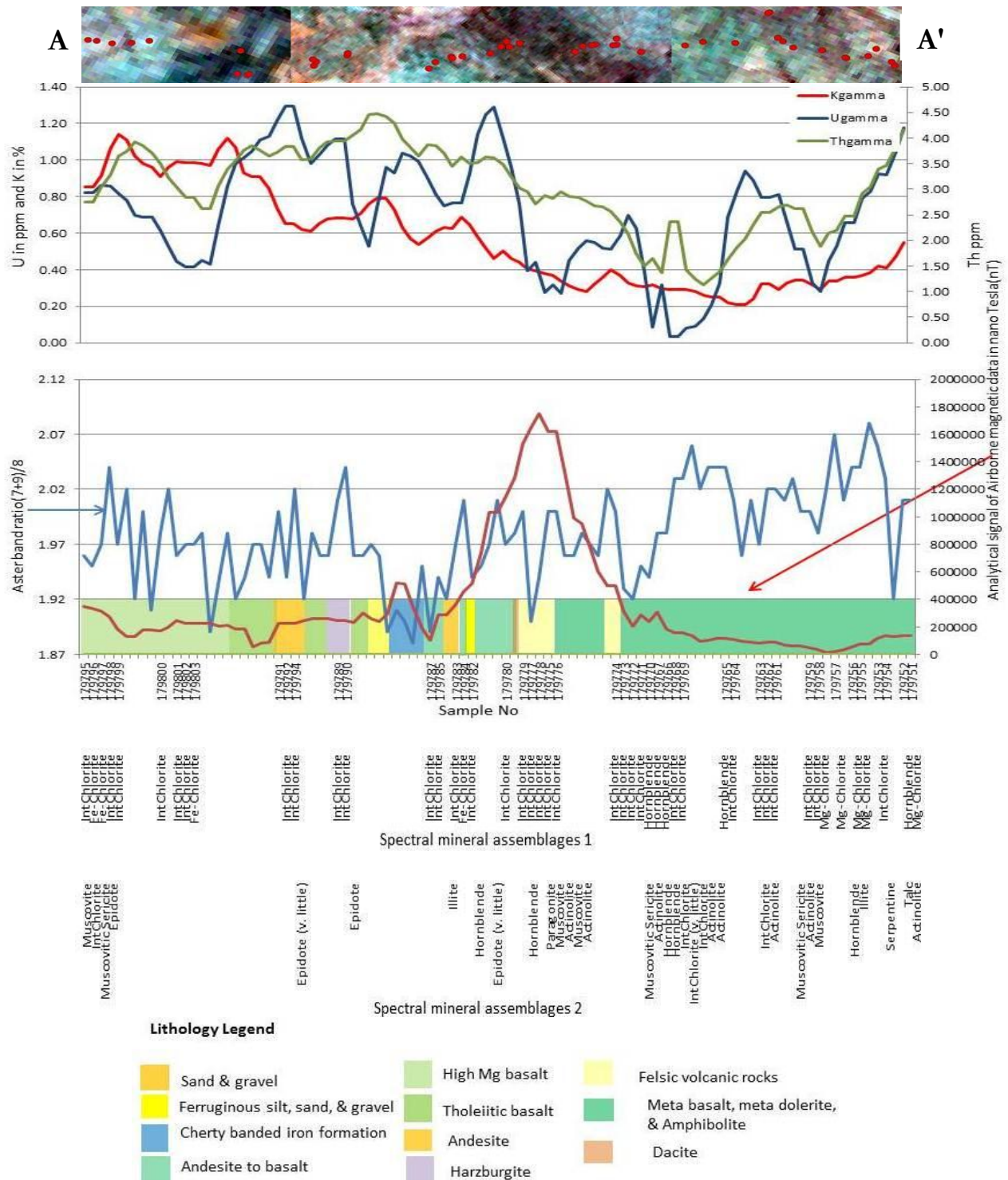


Figure 5: Radioelement concentrations, analytical signal of airborne magnetic, and ASTER band ratio data plotted against lithology. Mineral assemblage 1 represents alteration minerals that occur in a relatively larger amount and mineral assemblages 2 represents minerals that are present in a lesser amount

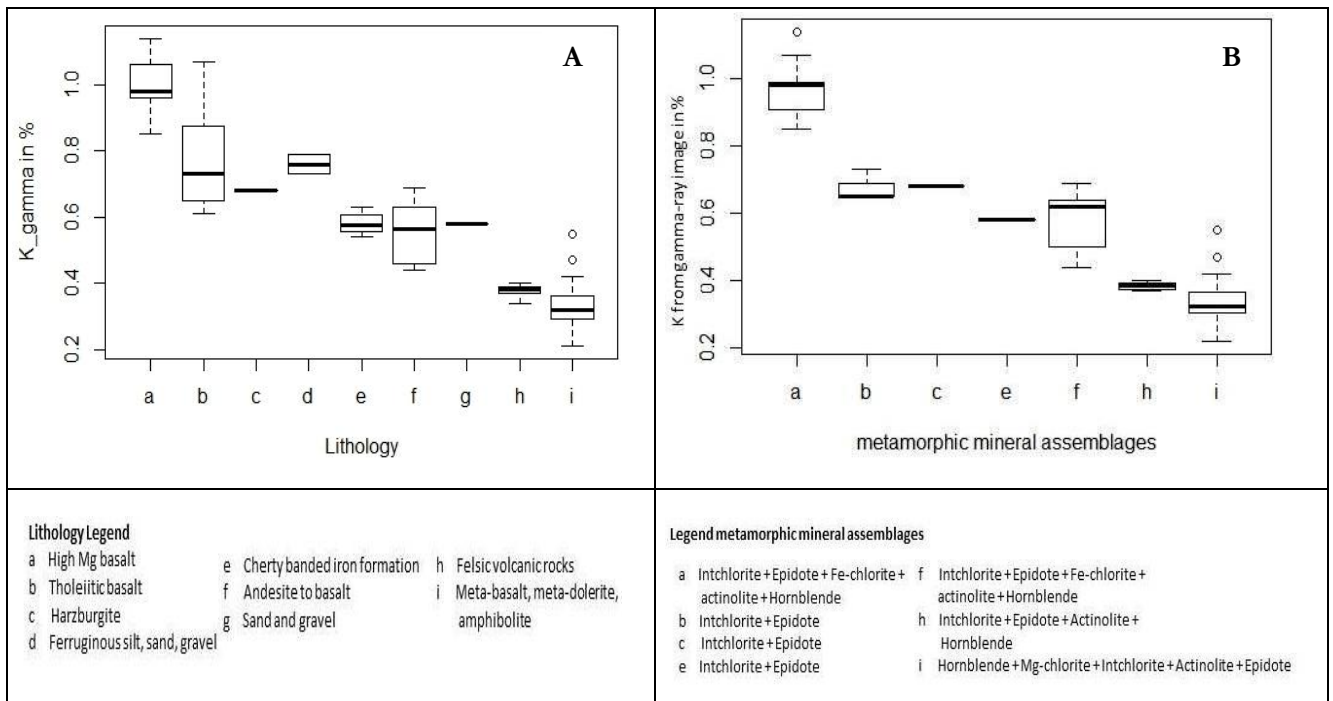


Figure 6: box plot of Potassium value from gamma-ray data (A) against lithology and (B) against metamorphic mineral assemblages.

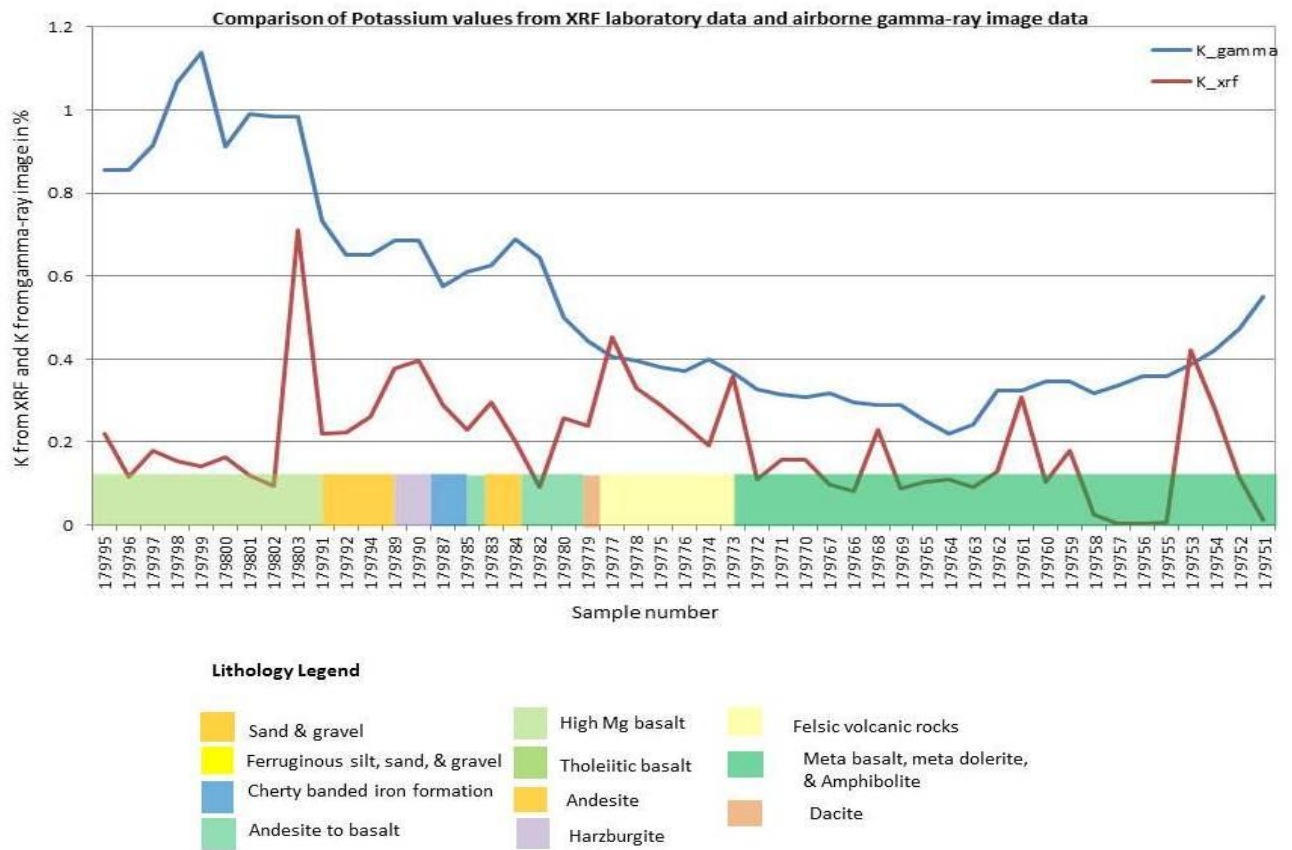


Figure 7: Comparison of potassium values from airborne gamma-ray data and XRF laboratory data

4.1.4. Airborne magnetic data interpretation and analysis.

The airborne magnetic data from Coonterunah Formation was found to be erroneous. The combined lithology of meta-basalt, meta-dolerite and amphibolite is generally expected to show high amplitude magnetic anomaly and it was reflected in the magnetic susceptibility data from rock samples though this high values didn't occur in the entire lithological unit. On the contrary, the combined lithology of meta-basalt, meta-dolerite and amphibolite except on the area directly to the north of the anomalous felsic volcanic lithology show low amplitude magnetic anomalies. This high amplitude on this combined lithology directly to the north of the high amplitude magnetic anomaly felsic volcanic lithology is not supported by the magnetic susceptibility measurements of rock samples which gave weak response to magnetic field strength.

The felsic volcanic lithology is expected to show low amplitude magnetic anomalies in nature except in some exceptional cases where felsic rock units which are rich in magnetic minerals can show high amplitude magnetic anomalies. This high amplitude magnetic anomaly in the felsic volcanic lithology is not supported from the magnetic susceptibility data obtained by measuring rock samples. The magnetic susceptibility measurements from rock samples gave weak magnetic response in the felsic volcanic lithology. Therefore there is an error in the airborne magnetic data.

The highest magnetic susceptibility measurements were found in the combined lithology of meta-basalt, meta-dolerite and amphibolite (179756, 179751). This combined lithology with mafic to ultramafic nature is normally expected to show high magnetic field strength and it was reflected in the magnetic susceptibility data from rock samples though this high values didn't occur in the entire lithological unit. The cause of this unexpected result could most probably be the interference of subsurface anomalies, errors from the flight line direction, the flight line spacing and the interference of banded iron formation. The flight line direction as explained in the methodology part is in east west direction when the transect is in a north south direction and the flight line (survey line) spacing is 400m.

Anomalies in the subsurface cause strong distortion of the airborne magnetic anomalies and may produce magnetic highs and lows in pairs due to the distortion of the shape of the total magnetic intensity data depending on the magnetic latitude of the study area. Banded iron formations are highly magnetic due to the amount of iron present in them (figure 8D). Hence; at airborne scale, they might interfere with the magnetic field strength of the area of interest and cause unexpected results. Records in such situation may show high magnetic anomalies when low magnetic anomaly is expected from a specific location based on ground rock samples.

Although the airborne magnetic data was found to be erroneous in this transect; it showed a contrast between different lithologies after the analytical signal and the 1st vertical derivative were calculated. The contrast between different lithologies helped in discriminating between different lithologies. Simplified geology outline was superimposed on the total magnetic field intensity, analytical signal and the 1st vertical derivative maps of the aeromagnetic data to help to identify different lithologies. Horizontal gradient of the total magnetic field was also calculated to check if it more closely reflect the lithological units in the geological map and it was not found useful.

The box plot (fig 9B) shows variability of analytical signal data values with metamorphic mineral assemblage to test the usability of aeromagnetic data in estimating the grade of metamorphism. As it was explained above, even though the airborne magnetic data contains errors, it showed some variability with the different metamorphic mineral assemblages.

4.1.5. Magnetic susceptibility data analysis

Magnetic susceptibility is an easy to measure petrophysical parameter both in the laboratory and in the field. It is controlled by the type and amount of magnetic minerals contained in a rock. It is mainly

controlled by ferromagnetic minerals (iron oxides or sulphides, represented for instance by magnetite and/or pyrrhotite, respectively) Sometimes, by paramagnetic minerals (mafic silicates such as olivine, pyroxenes, amphiboles, micas, tourmaline, garnets), and occasionally by diamagnetic minerals (calcite, quartz). Most of the ferromagnetic minerals belong to accessory minerals that are profound indicators of geological processes. Magnetic susceptibility also depends on subsequent metamorphic and alteration processes; hence it plays a great role in solving some geological problems (Hroudá et al., 2009).

Graphical (figure 10) representation of the magnetic susceptibility data of several rock samples showed that only two samples; sample number 179756 and sample number 179751 have strong magnetic response to magnetic susceptibility measurements and the rest of the rock samples didn't show significant variability with lithology. This strong magnetic response occurred in the combined lithology of the meta-basalt, meta-dolerite and amphibolite from the geological map and from the petrographic classification; this two samples are from komatiite which is an ultramafic rock. Ultramafic rocks in nature are expected to show strong magnetic response to magnetic susceptibility estimates.

4.1.6. Variations in SiO₂, K₂O and MgO content with lithology

The transect plot (figure 12) shows the systematic variations of the three oxides with lithology. This illustration was used to check if the analytical results were reliable. All lithologies used in this analysis are from the petrographic classification of Smithies et al. (2007) and it is explained in which category the samples discussed fall in the geological map. The petrographic classification is most of the time in agreement with the geological map. This makes the geological map reliable.

The typical SiO₂, K₂O and MgO contents in the meta-basalt, meta-dolerite and amphibolite are 41.49%, 0.005% and 29.95%. These typical values are found from the same sample; sample number 179757 which is komatiitic from the petrographic classification. In the geological map this sample falls in the generalized lithology of meta-basalt, meta-dolerite and amphibolite. Ultramafic rocks in nature contain very low amount of SiO₂ which is less than 45%, generally greater than 18% MgO, high FeO, and low potassium. The typical SiO₂, K₂O and MgO contents of basalt in the Coonterunah transect are 45.41%, 0.23% and 5.474 %, respectively in the geological map these sample (179802) falls in the combined lithology of meta-basalt, meta-dolerite and amphibolite. Basalts in nature contain 45-55% SiO₂, they are high in Fe, Mg, Ca, and low in K. Therefore what is observed from this typical value is to be expected in nature.

In nature, andesite contains SiO₂ of about 55-65%, it is intermediate in Fe, Mg, Ca, Na, K contents. Andesite (sample number 179775) in Coonterunah transect contains typically 60.03% SiO₂, 0.7% K₂O and 3.17% MgO. Therefore results from the XRF laboratory analysis and the natural occurrence of these oxides in andesite coincide. This sample in the geological map occurs in the felsic volcanic lithology. The typical SiO₂, K₂O and MgO contents of dacite (sample number 179779) are 60.15%, 0.57% and 2.7% respectively. This contents are to be expected since dacite, 63%-68% in SiO₂ content, is generally intermediate in composition between andesite and rhyolite (rhyolite contains 65-75 % SiO₂, low in Fe, Mg, Ca, high in K, Na). This sample is categorized under andesite to basalt in the geological map; in this case we find a mismatch between the rock classification of Smithies et al. (2007) using REE (rare earth elements). The generalized geological map shows some mismatches with the petrographic classification, but generally it is a good geological map (for more details about the similarities and differences between the legacy geological map and the petrographic classification from Smithies et al. (2007), see appendix 4A and B).

Sample number 179751 and 179756 of the komatiitic lithology show high magnetic susceptibility values (figure 10); this coincides with high Mg content and low K content (figure 12). In nature, ultramafic rocks contain high Mg, low K and they are rich in magnetic minerals and hence show strong positive magnetic response to magnetic susceptibility measurements. This is manifested in this transect where the high Mg content, low potassium content and high magnetic susceptibility coincide for komatiite which is an ultramafic rock.

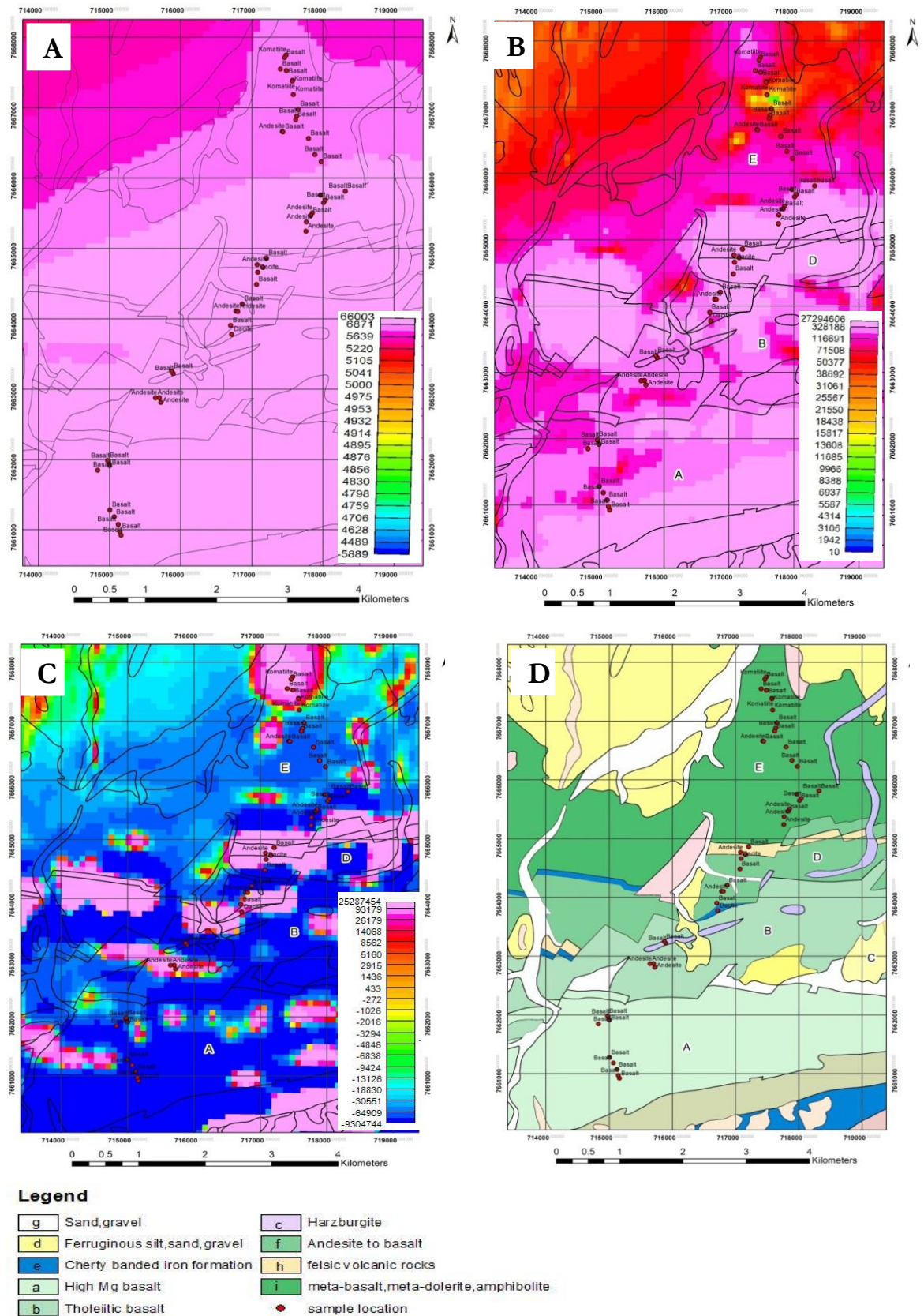


Figure 8: Aeromagnetic data in nano Tesla (nT) (A) total magnetic data, (B) analytical signal, (C) 1st vertical derivative. D is legacy geological map.

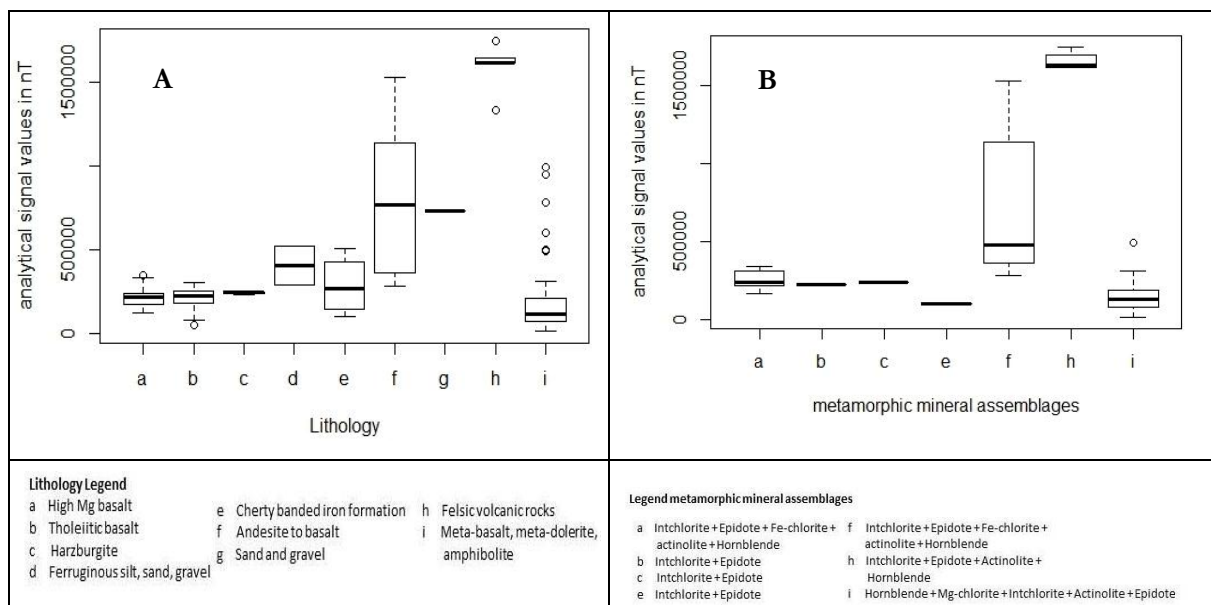


Figure 9: box plot showing the variability of analytical signal with lithology, B: box plot showing the variability of analytical signal with metamorphic mineral assemblages

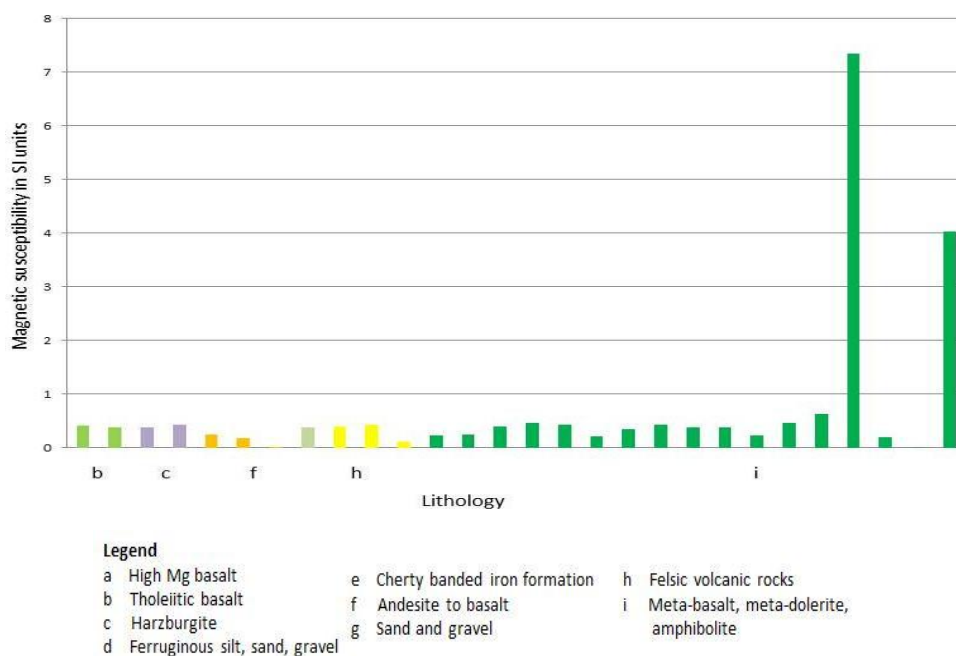


Figure 10: Magnetic susceptibility variations with lithology

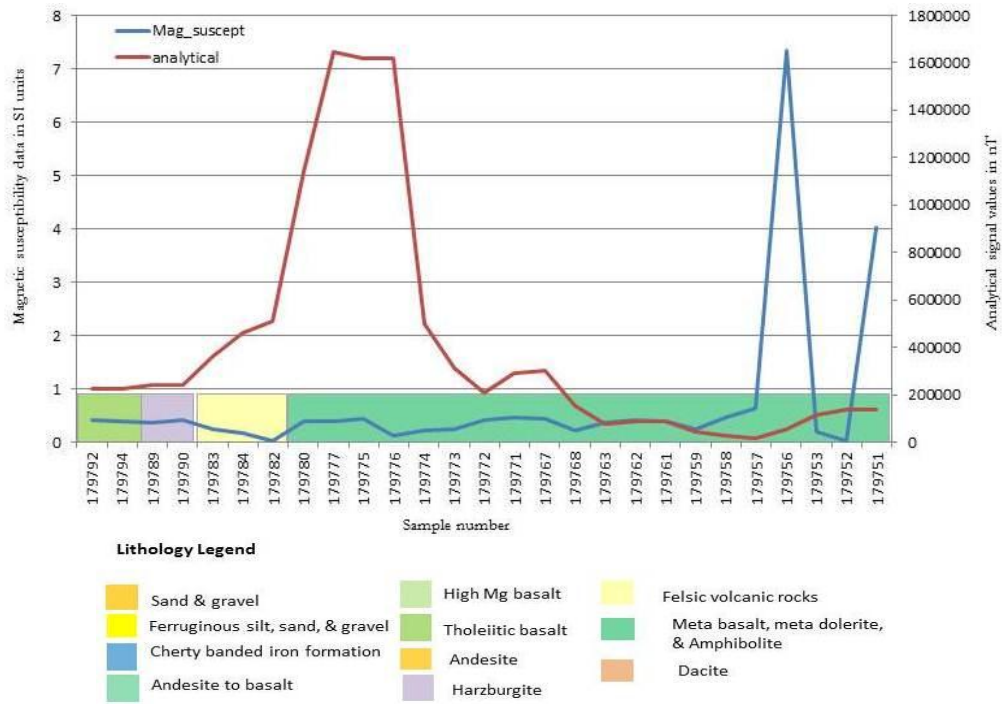


Figure 11: Comparison of magnetic susceptibility data with the analytical signal of airborne

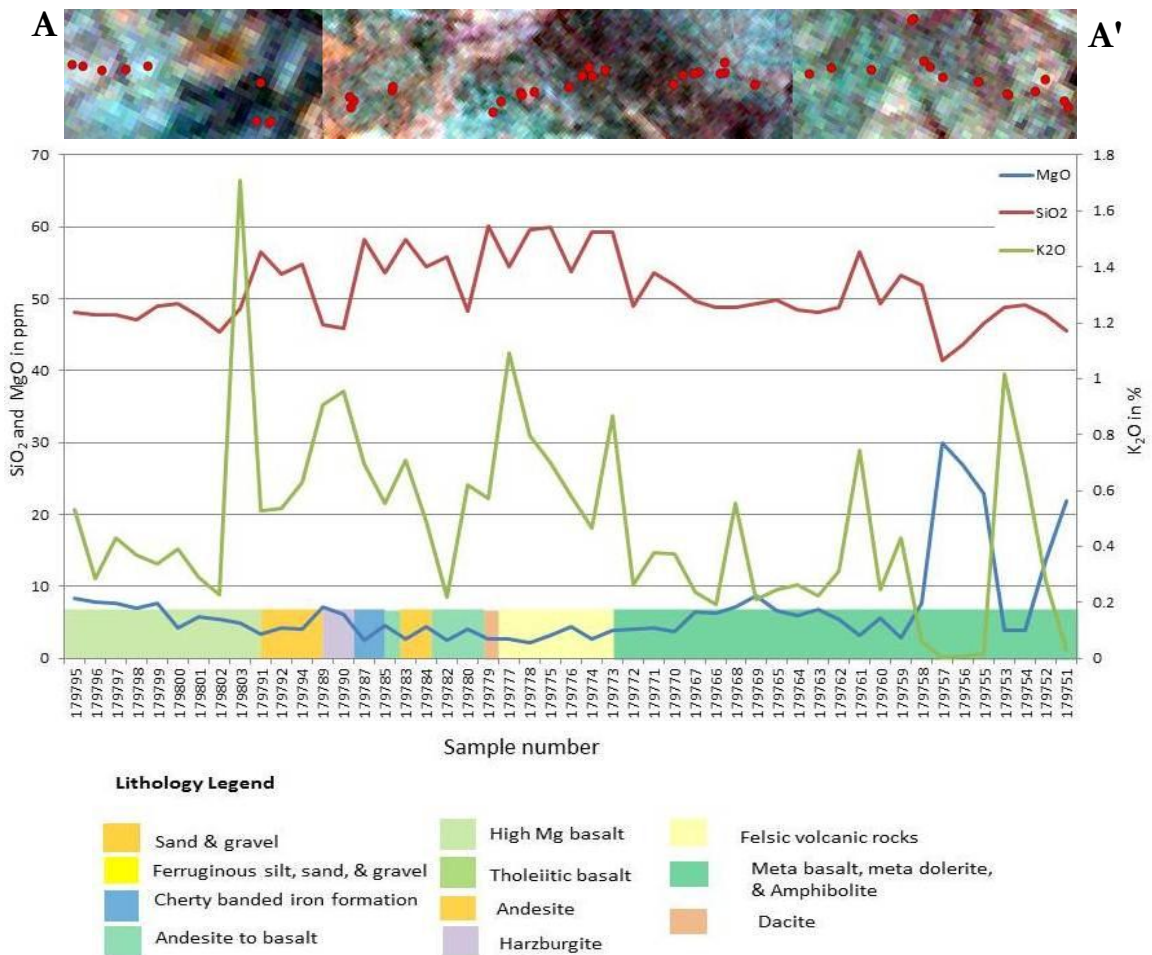


Figure 12: Variations of three major oxides (SiO₂, K₂O and MgO) with lithology

4.1.7. Alteration box plots for intensity of hydrothermal alteration

Alteration box plot (figure 13) method as discussed in the methodology section was used to separate samples which are hydrothermally altered and unaltered ones. Two box plots were generated for both lithology and metamorphism. Most of the samples from coonterunah transect fall inside the least altered rocks box and some fall outside of the box because of their mafic nature of lithology. For rock samples to be called as hydrothermally altered and with substantial metasomatism (i.e. change in chemical composition), we need to find samples falling outside the list altered box and near sericite, K-feldspar standard alteration minerals mentioned in the box plot image. Therefore none of our samples from this transect are hydrothermally altered.

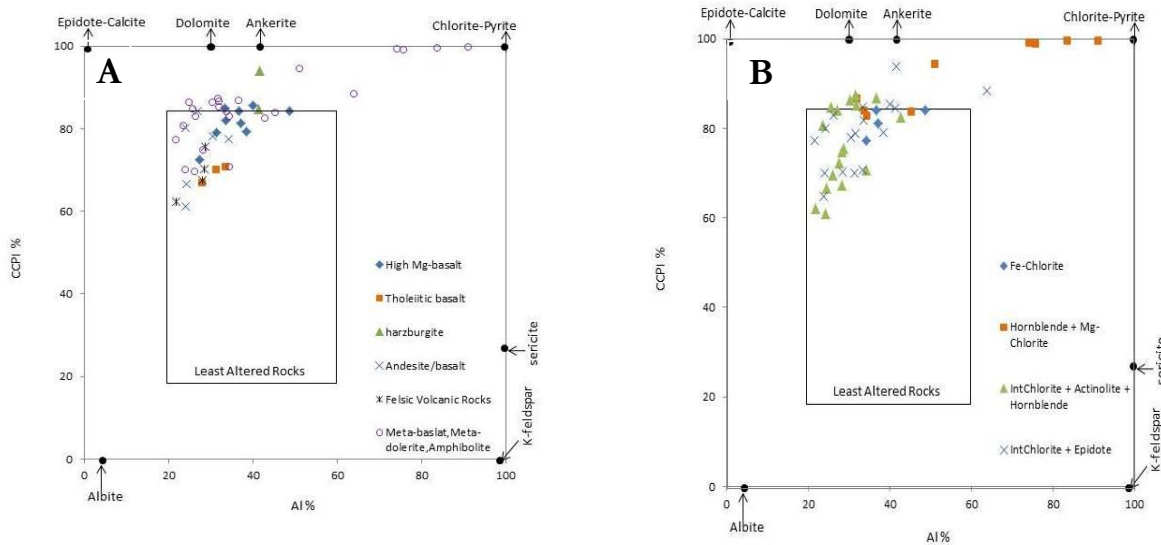


Figure 13: Alteration box plots plotted CCPI (Chlorite Carbonate Pyrite Index) on the Y axis and AI (Ishikawa Alteration Index). A is plotted with lithology, and B is plotted with alteration mineral assemblages from the work of (Abweny, 2012)

4.2. Duffer Formation

4.2.1. ASTER satellite imagery data analysis

The discrimination of different lithologies in this formation is not very apparent in both of the ASTER images (Figure: 14A and 14B). This is because the transect is short with restricted number of samples. However we see distinct boundary between the bluish and reddish unit separated by a south east North West running imaginary line. This has something to do with surface alterations and is not related to the lithological boundaries on the geological map. The sand and gravel unit which is not very important for this research is also standing out in the ASTER satellite imagery. Another unit which is clearly visible is the combination of shale and banded iron formation. Almost the same scenario is apparent in the aster band ration image but the shale and banded iron formation lithological unit in here is faint.

4.2.2. Gamma-ray ternary image for lithological discrimination

The gamma-ray image (figure 14C) shows clearly the sand and gravel unit, unfortunately the rest are not distinctive. The gamma-ray image generally shows more details in a large scale, hence the reason why we do not see distinct geological features here is that the transect is quite short. The sand and gravel unit is rich in potassium which is manifested by the bright reddish color. The rest are thorium rich manifested by the greenish color. Uranium occurs in a very small amount, it is represented by the bluish color.

4.2.3. Airborne magnetic data analysis

The airborne magnetic intensity data shows similar behaviour in all of the transects. Though there is no correlation between the litho-contacts in the geological map and the contacts of the magnetic field strength data, analytical signal (15B) and the 1st vertical derivative (15C) of the airborne magnetic data show much variability in the magnetic field strength among different rock units especially the banded iron formation (BIF). The only lithological unit, in Duffer formation, clearly visible in the airborne magnetic survey maps is andesite to dacite, and this lithology do not show the same characteristics throughout the area. This, as explained in the Coonterunah formation is most likely due to the inhomogeneity in the magnetic mineral content of the rocks. The response from the airborne magnetic data matches with the response from the ground magnetic susceptibility data.

4.2.4. Variability of ASTER band ratio results

(Figure 16) shows the variability of aster band ratios $(4+6)/5$, $(5+7)/6$ and $(7+9)/8$ with lithology and alteration mineral assemblages. ASTER band ratio $(4+6)/5$ shows strong variability with lithology. Deep features are observed for band ratio $(7+9)/8$ on the andesite to dacite and felsic tuff+ greywacke + chert lithologies. This is caused by the intermediate chloritic alteration. Band ratio $(5+7)/6$ generally shows deeper features when rocks are felsic and shallower features when lithologies are mafic.

4.2.5. Variability of potassium contents

Although the variability of potassium with lithology is not quite pronounced in the scatter plot (figure 17), it is clearly visible in the box plot (figure 18A) which shows the variability of potassium concentration with lithology. The combination of felsic tuff, greywacke and chert as well as the combination of dacite and andesite also contain considerable amount of potassium. The potassium content of rocks is obviously dependent on the amount of potassium rich minerals present in the rock unit. Therefore it is to be expected that rocks with more mafic nature of lithology might also contain relatively higher amount of potassium than felsic rocks in the vicinity if they contain relatively higher amount of potassium rich minerals. In either case potassium remains to be an important element in discriminating between different rock types.

The box plot (figure 18B) shows the variability of potassium content with metamorphic mineral assemblages. In this formation the grade of metamorphism as referred from the attributes of the geological map and the report associated with it is greenschist facies. Though the rock units in this formation are metamorphosed to only one facies, the potassium value from gamma-ray shows variability with metamorphic mineral assemblages which when there are differences in metamorphic grade such as in Coonterunah formation (rocks in this formation are metamorphosed to greenschist and amphibolite facies), are key indicators of metamorphic grade.

In order to check the reliability of the data extracted from airborne gamma-ray data, a scatter plot (figure 17) showing the variability of potassium from airborne gamma-ray data and potassium from XRF laboratory analysis was generated and they show a similar trend confirming that the airborne gamma-ray data is reliable.

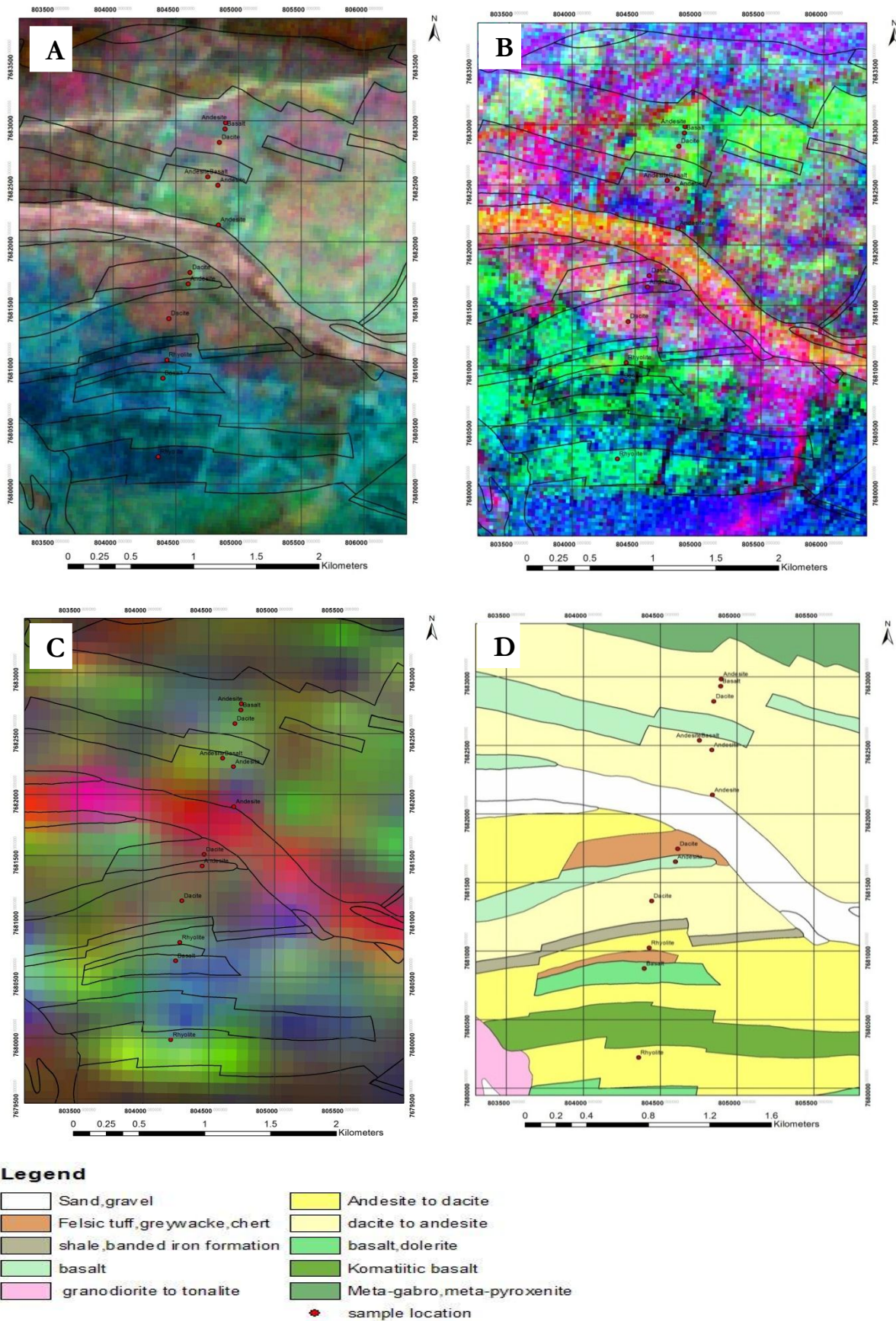


Figure 14: ASTER band combination 468(R=4, G=6, B=8). B: ASTER band ratio image $R = (4+6)/5$, $G = (5+7)/6$ and $B = (7+9)/8$. C: Gamma-ray ternary image $R=K$, $G=Th$, $B=U$. D: Legacy geological map

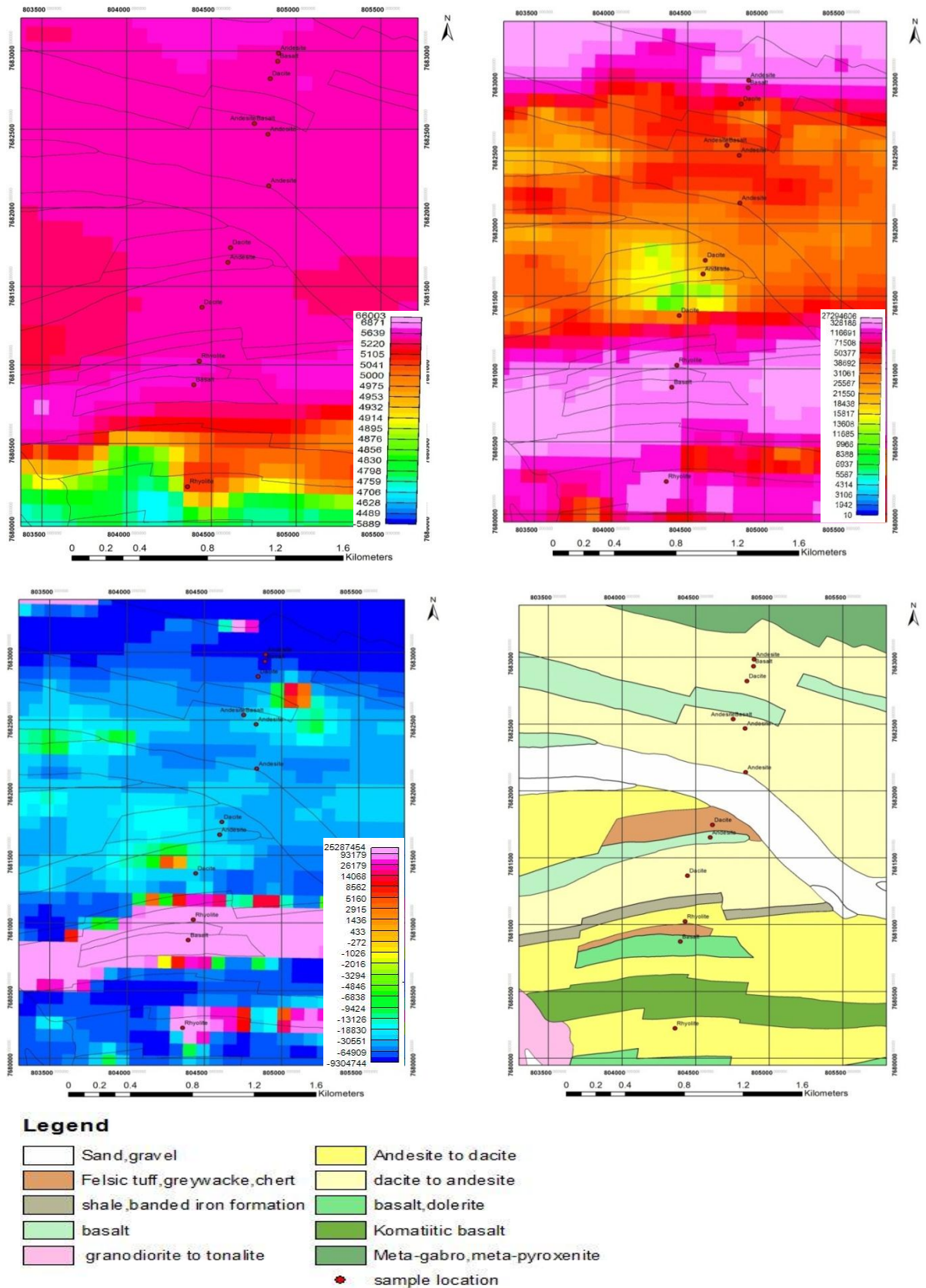


Figure 15: Aeromagnetic magnetic data in nT (A) total magnetic data, (B) analytical signal, and (C) 1st vertical derivative. (D) Legacy geological map.

4.2.6. Quantitative analysis of the airborne analytical signal data.

The magnetic field strength from aeromagnetic data is as expected in the (figure 17) clearly shows that the rocks with mafic nature of lithology generally show high magnetic anomaly and felsic ones show the least magnetic strength values. This is also manifested in the ground data from rock specimens (figure 22 and 23).

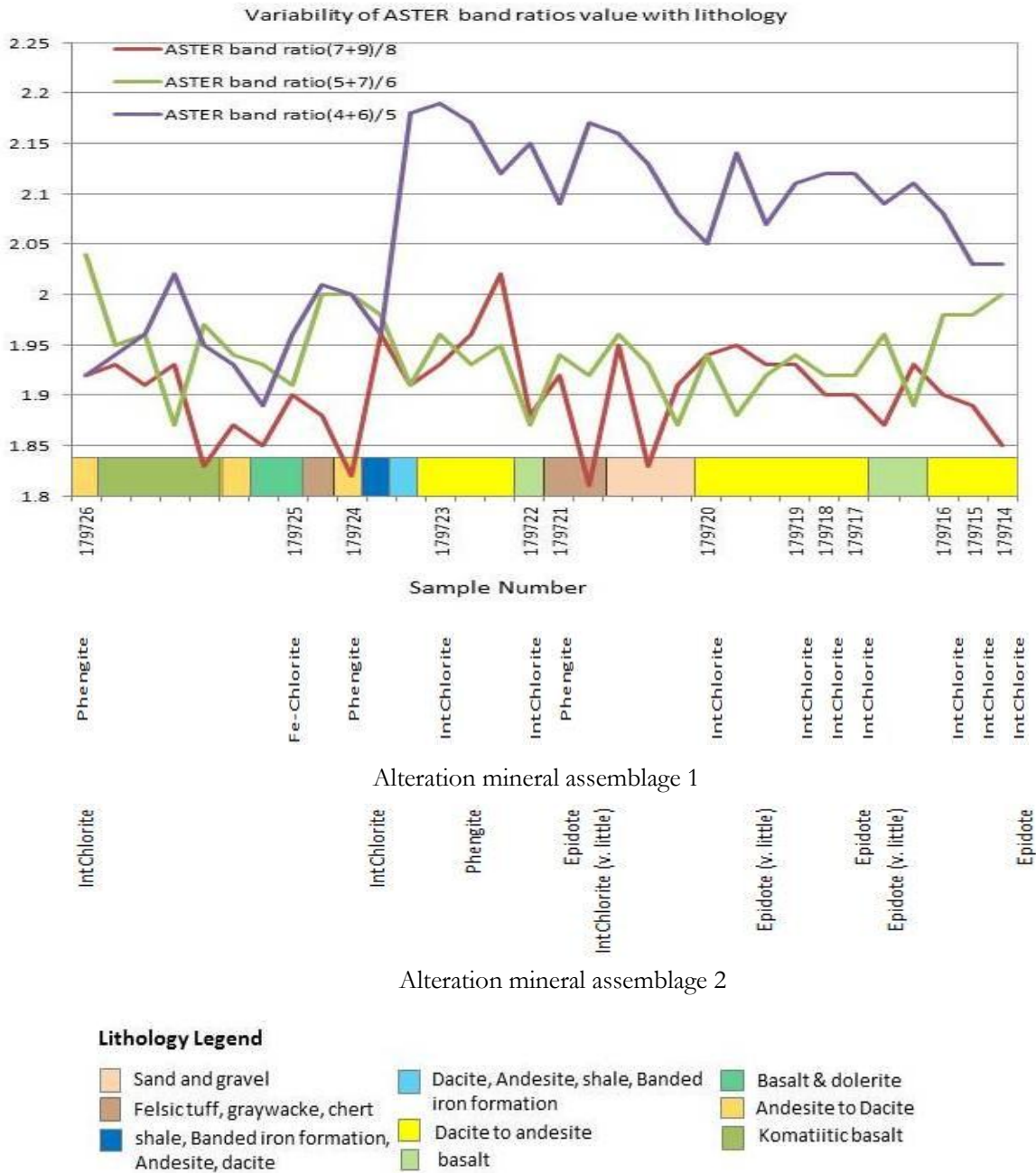


Figure 16: ASTER band ratio values plotted against lithology and alteration mineral assemblages to show the response to lithological variations and relative intensity of alteration.

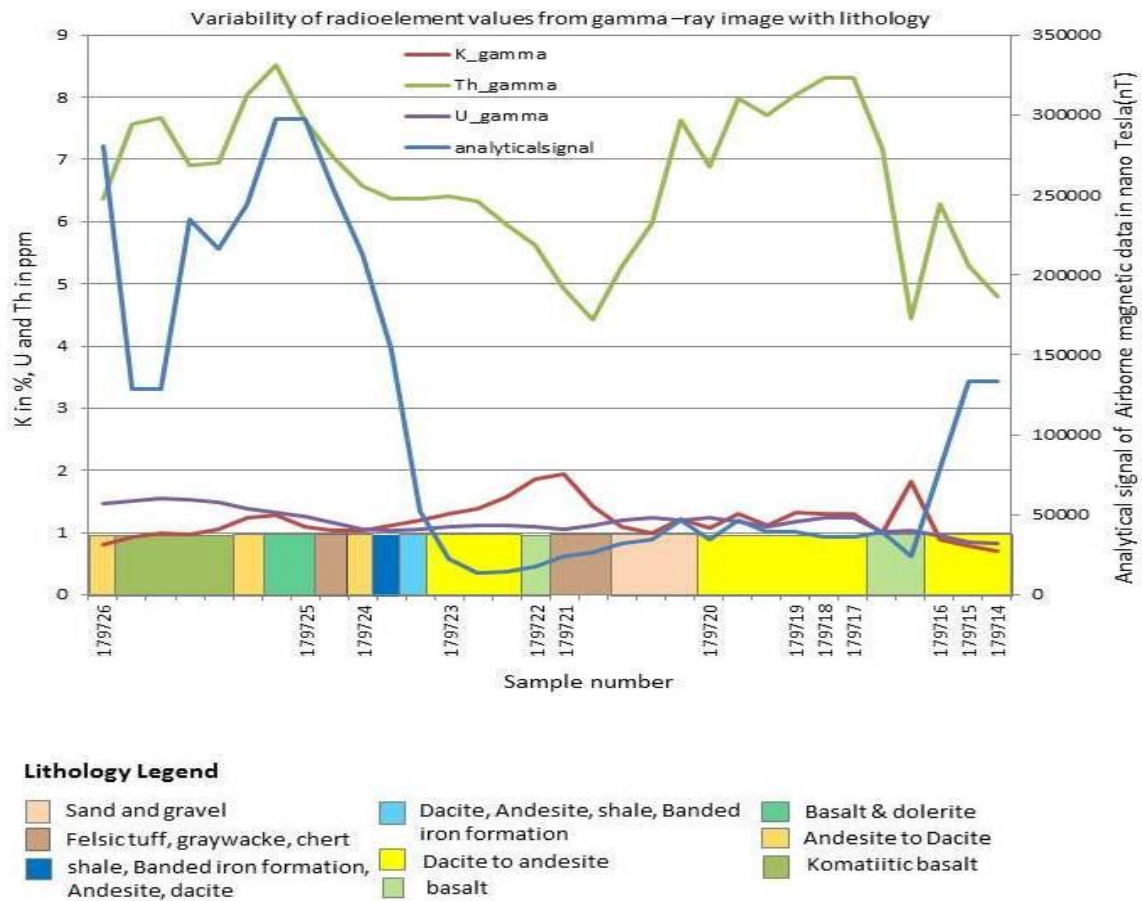


Figure 17: Radioelement concentrations, airborne total magnetic, and ASTER band ratio data plotted against lithology.

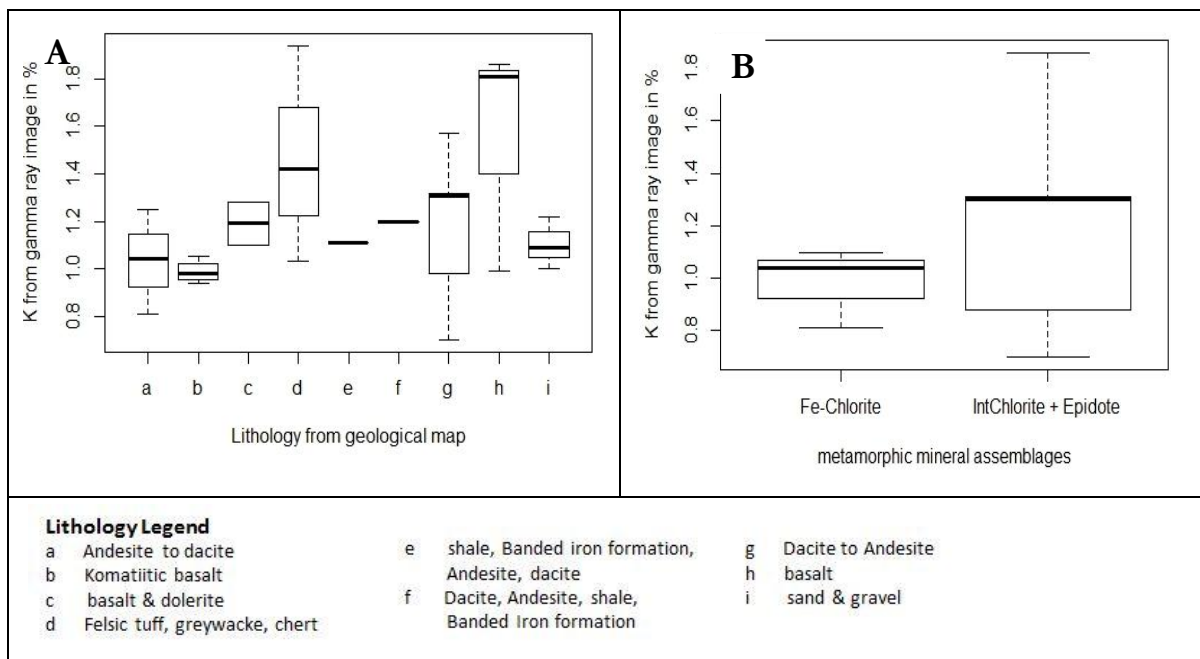


Figure 18: box plot of Potassium value from gamma-ray data (A) against lithology and (B) against metamorphic mineral assemblages.

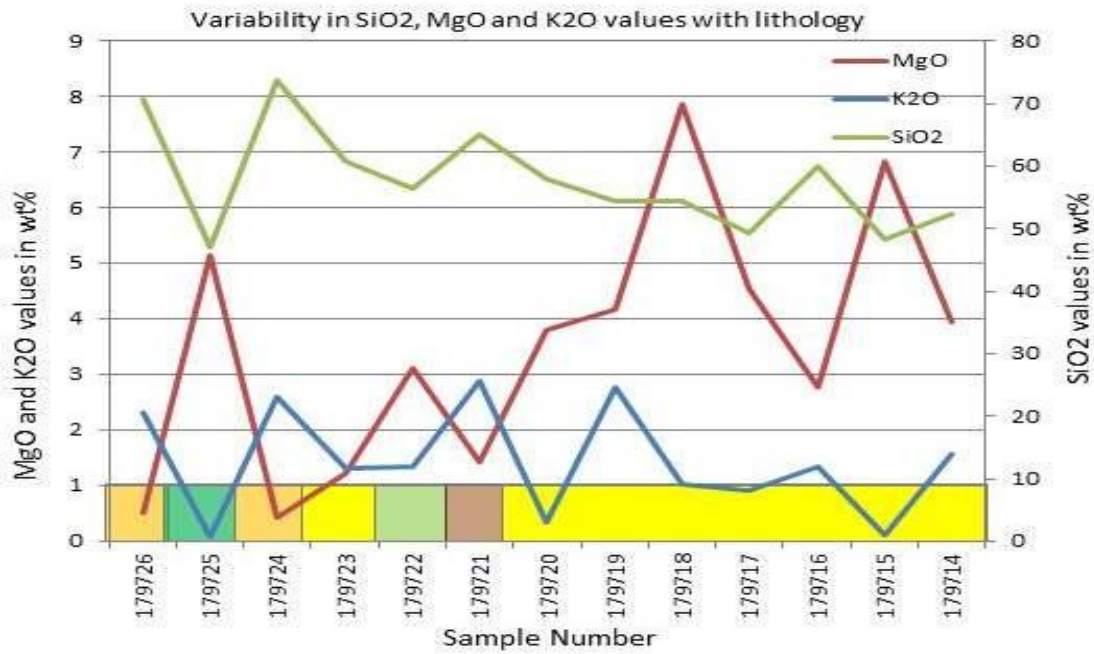
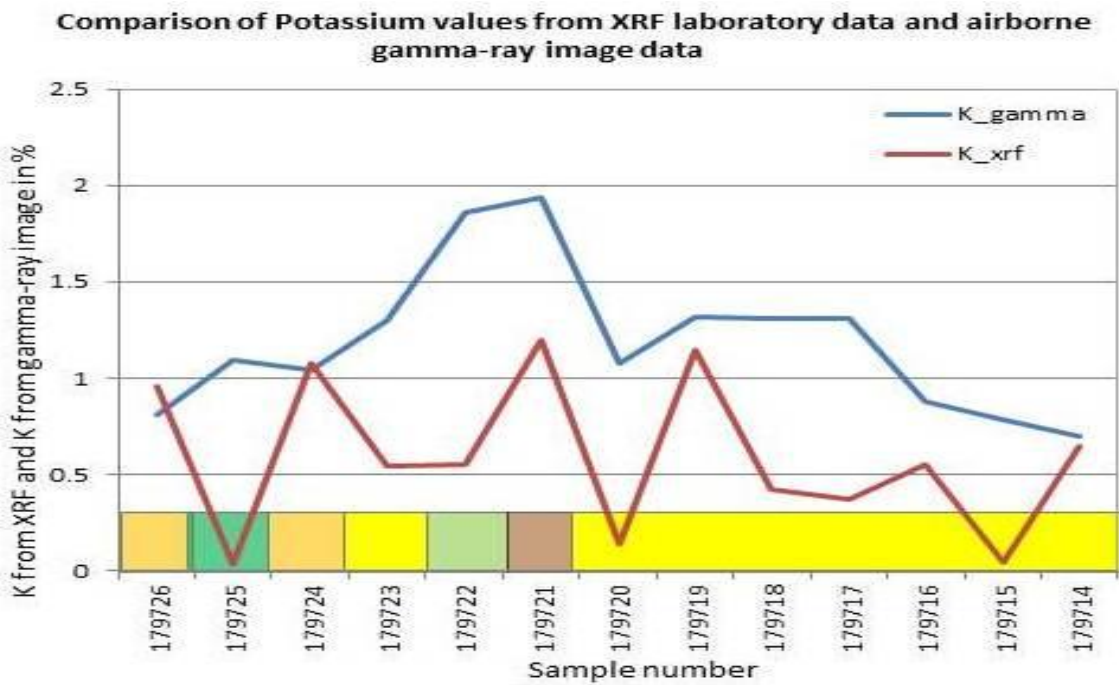


Figure 19: Variations of three major oxides (SiO₂, K₂O and MgO) with lithology



Lithology Legend

- Sand and gravel
- Dacite, Andesite, shale, Banded iron formation
- Basalt & dolerite
- Felsic tuff, graywacke, chert
- Dacite to andesite
- Andesite to Dacite
- shale, Banded iron formation, Andesite, dacite
- basalt
- Komatiitic basalt

Figure 20: Comparison of potassium values from airborne gamma-ray data and XRF laboratory data

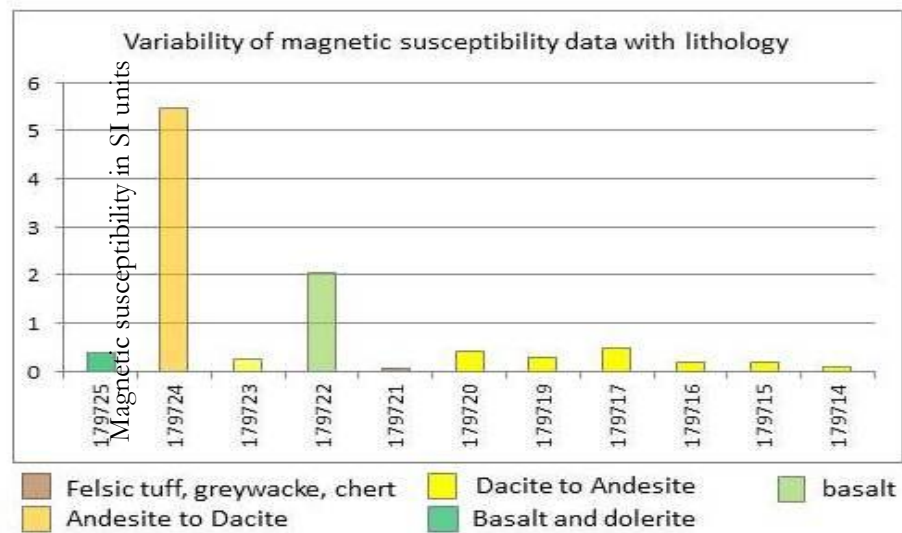
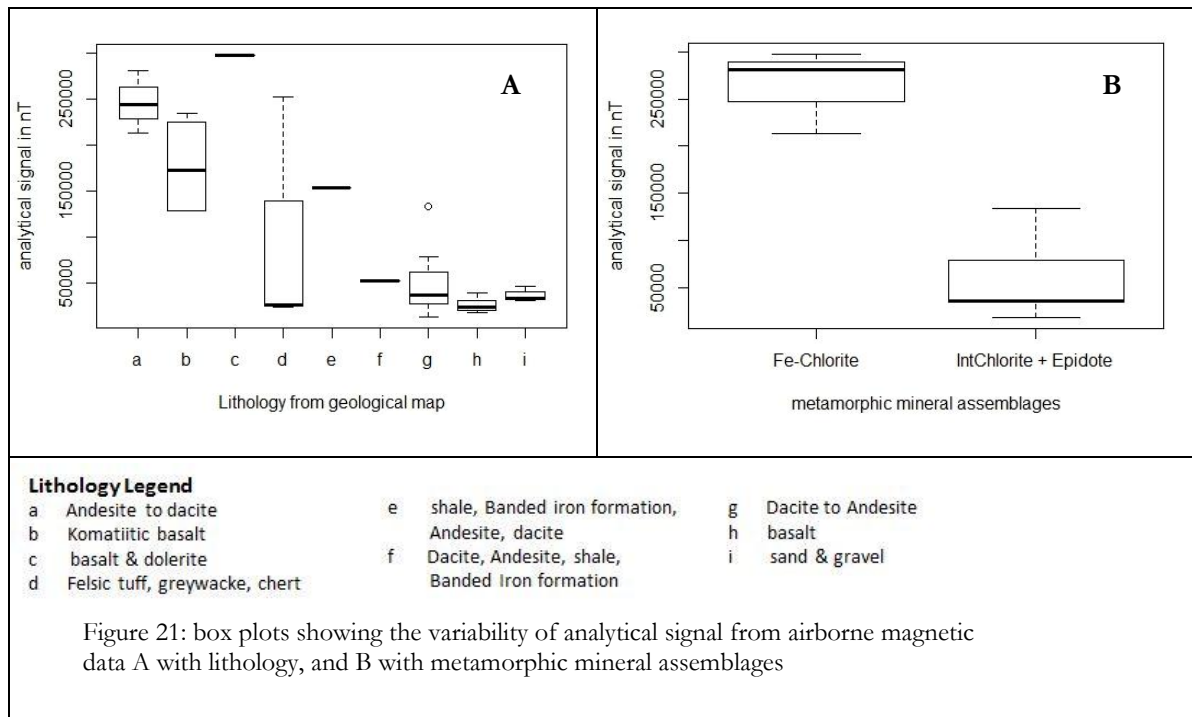


Figure 22: Magnetic susceptibility variations with lithology

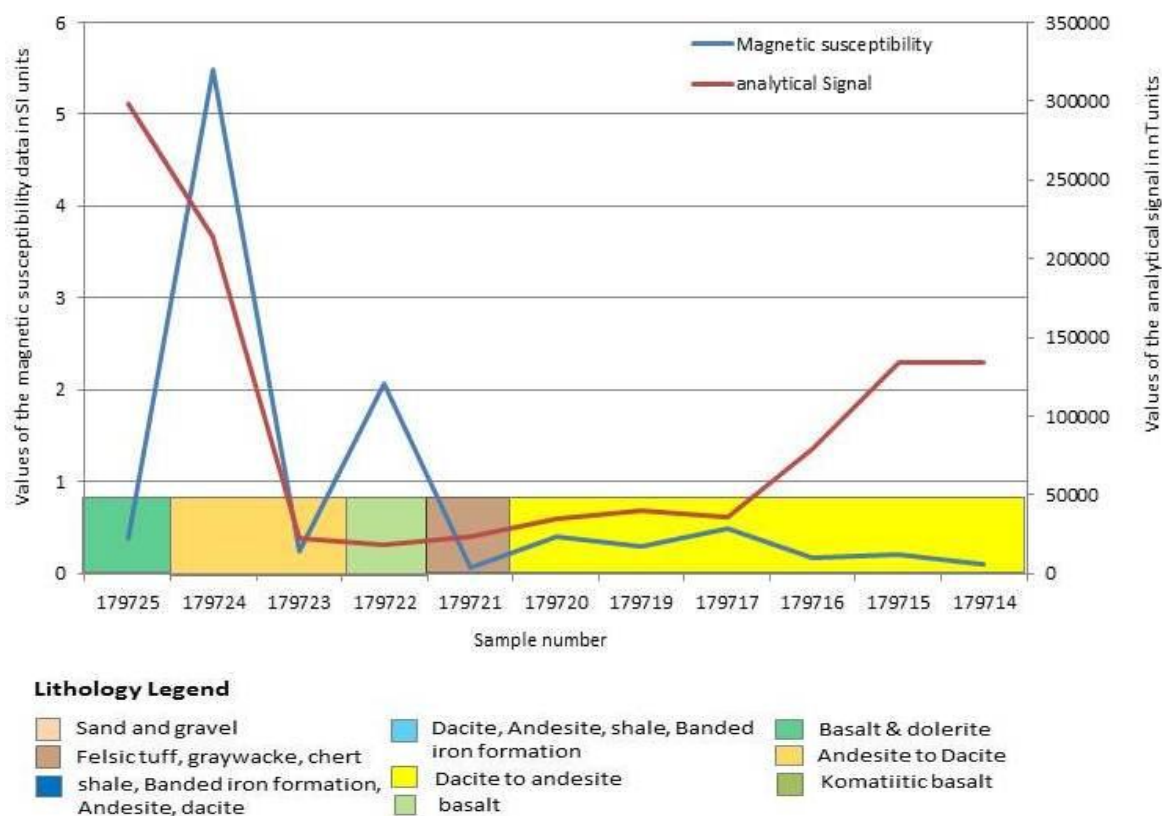


Figure 23: Comparison of analytical signal of airborne magnetic data and magnetic susceptibility data from rock samples.

4.2.7. Variability of MgO and SiO₂ content with lithology

The line plot (figure 19) illustrates the variations of the three oxides SiO₂, K₂O and Mg with lithology. This illustration, in the same manner as in the Coonterunah Formation was used to check if the analytical results were reliable. All lithologies used in this analysis are from the petrographic classification of Smithies et al. (2007) and it is explained in which category the samples discussed fall in the geological map. The petrographic classification is most of the time in agreement with the geological map. This makes the geological map reliable. This analysis in the same way as in the Coonterunah Formation is made to check the reliability of analytical results.

The typical SiO₂ content of basalt (from petrographic classification) in this transect is 47.16% (sample number 179725). As it is explained in the Coonterunah Formation, basalts in nature contain 45-55% SiO₂, there for the analytical SiO₂ content of basalt agrees with the average occurrence of this oxide in basalt in nature. The typical K₂O value of basalt from the same sample number is 0.09%, this is a very low content and it is to be expected since basalts in nature contain low amount of potassium. Moreover the typical MgO content of basalts from the same sample number is 5.14% and this matches with the natural abundance of MgO in basalts which contain high MgO content. In the geological map this sample number is part of basalt and dolerite lithology.

The typical SiO₂, K₂O and MgO contents of andesite (sample number 179720) in this transect are 58.1%, 0.34% and 3.81% respectively. In nature andesite contains about 55-65% SiO₂; it is intermediate in K and Mg. The fore the results from analytical chemistry are reliable. This sample is grouped under the dacite to andesite lithology in the geological map which fairly matches with the petrographic classification. Dacite (sample number 179721) typically contains 65.2% SiO₂, 2.88% K₂O and 1.43% MgO. Dacite in nature contains about 63%-68% SiO₂ and it is generally intermediate between andesite and rhyolite in

compositon. This sample is categorized in the combined lithology of felsic tuff, greywacke and chert in the generalized geological map.

The typical SiO_2 , K_2O and MgO contents of rhyolite (sample number 179724) in this transect are 73.73%, 2.59% and 0.42% respectively. This contents are to be expected since rhyolite in nature contains (rhyolite 65-75 % SiO_2 , and is low in Mg and K contents. This lithology is categorized under Andesite to dacite from the geological map.

4.2.8. Alteration box plots for the intensity of hydrothermal alteration

The alteration box plots (figure 24A and 24B) plotted with lithology and alteration mineral assemblages respectively show that almost all the samples fall inside the least altered box except few samples falling close to the dolomite and Ankerite standard alteration minerals. The reason for the few samples falling outside of the list altered rocks and next to the above mentioned standard alteration minerals have to do something with their compositon and have nothing to do with hydrothermal alteration. Hence all the samples from duffer formation are hydrothermally unaltered.

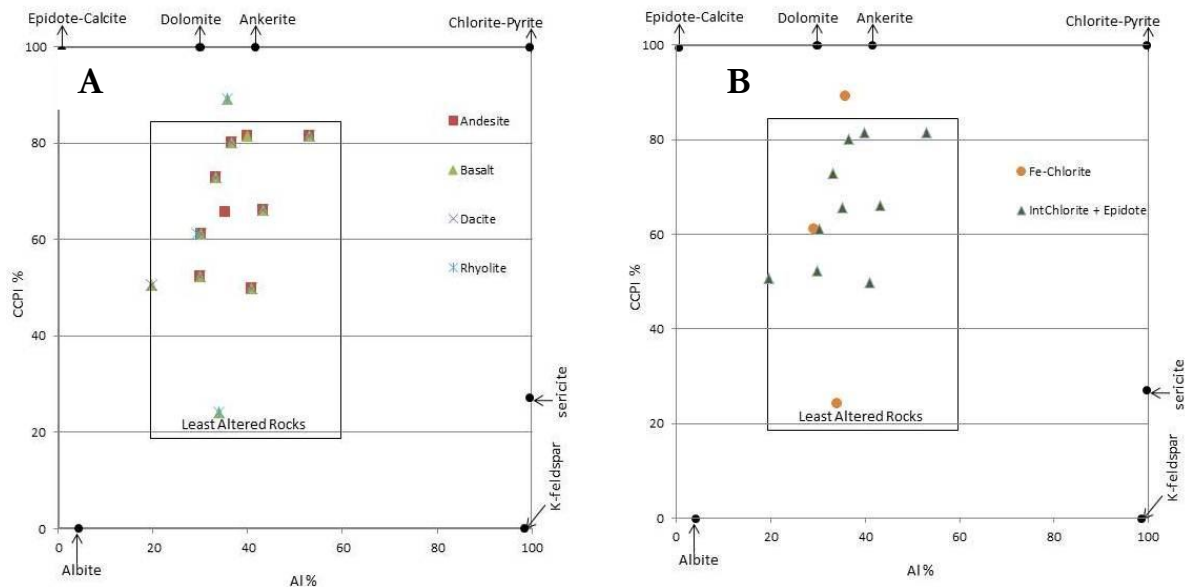


Figure 24: Alteration box plots plotted CCPI (Chlorite Carbonate Pyrite Index) on the Y axis and AI (Ishikawa Alteration Index). A is plotted with lithology, and B is plotted with metamorphic mineral assemblages from the work of (Abweny, 2012).

4.3. The Panorama District

4.3.1. ASTER satellite imagery data analysis

The samples in Panorama district are restricted to 3 lithologies, hence the spatial dimensionality is limited hence we do not expect to see much variability in both of the ASTER satellite images (figure 25A and B). The boundaries in the ASTER satellite images generally do not match with the contacts in the geological map. The only lithology with clear boundary is the combination of dacite and rhyolite. The other lithology with a clear boundary is Monzogranite, no sample is taken from this lithology, and hence it is not our point of interest. The boundary between the two lithologies where almost all of our samples are taken is shifted north wards, this most likely is due to the gradual mineralogical change between this two lithologies.

4.3.2. Gamma-ray ternary image for lithological discrimination

The gamma-ray survey image (25C) of the Panorama district doesn't show clear boundaries between lithologies too. This very short transect is dominated by almost one color, bluish. This is a manifestation of the dominance of uranium in this district. The greenish color represents thorium. The faintly greenish brown and bluish brown represents the presence of potassium in combination to thorium and uranium respectively.

4.3.3. Airborne magnetic data analysis

In the Panorama district (figure 26A, B and C), all the samples are concentrated in 2 lithologies as it was explained previously, microdiorite and diorite and andesite to basalt. One sample occurs in the dacite to rhyolite rock unit. The most mafic lithology microdiorite and diorite shows the highest amplitude magnetic anomaly and andesite to basalt rock unit shows intermediate magnetic field strength. The dacite to rhyolite rock unit shows relatively low magnetic field strength in all cases which might be expected in nature.

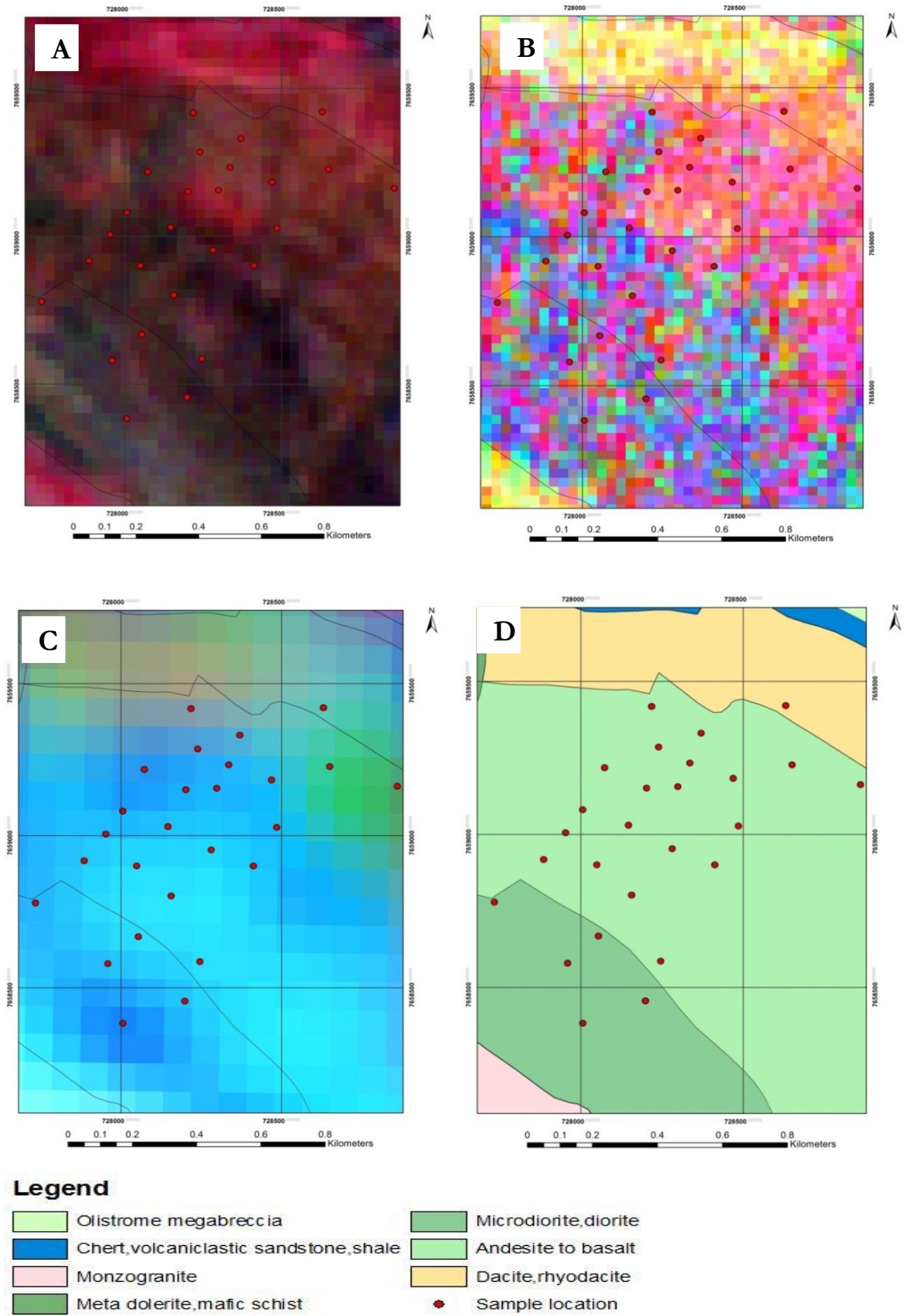


Figure 25: ASTER band combination 468(R=4, G=6, B=8). B: ASTER band ratio image $R = (4+6)/5$, $G = (5+7)/6$ and $B = (7+9)/8$. C: Gamma-ray ternary image $R=K$, $G=Th$, $B=U$. D: Legacy geological map

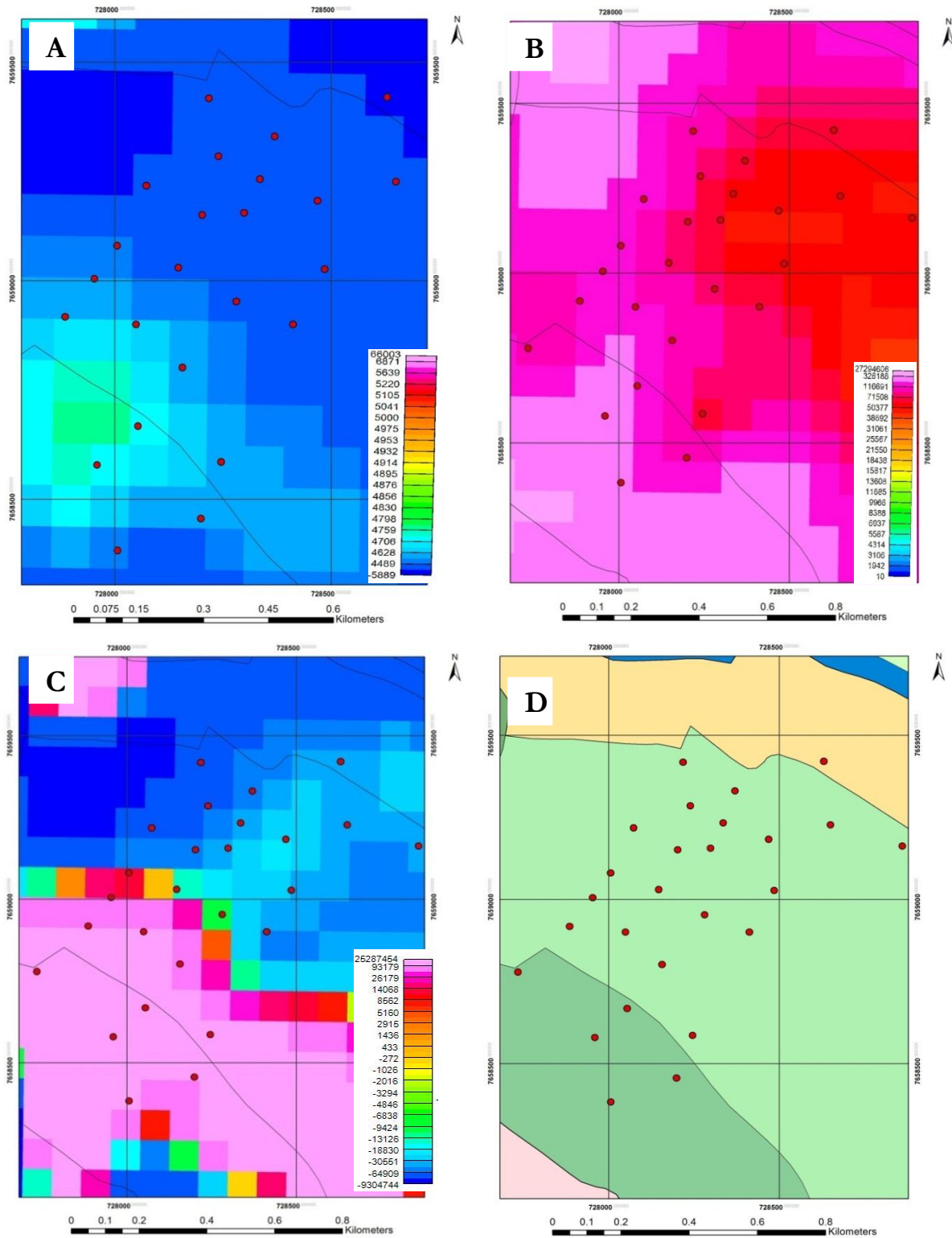


Figure 26: Aeromagnetic data in nT (A) total magnetic data, (B) analytical signal, (C) 1st vertical derivative. D legacy geological map.

4.3.4. Alteration box plot

Figure 27A and B show alteration boxplots for the Panorama district. In this district all of the samples fall outside of the least altered box indicating intense hydrothermal alteration. Hence all these samples in contrast to the samples from Coonterunah formation and Duffer formation are hydrothermally altered. The type of alteration is mainly chloritic. The spectroscopic study of the samples from this district was done by Van Ruitenbeek et al. (2012).

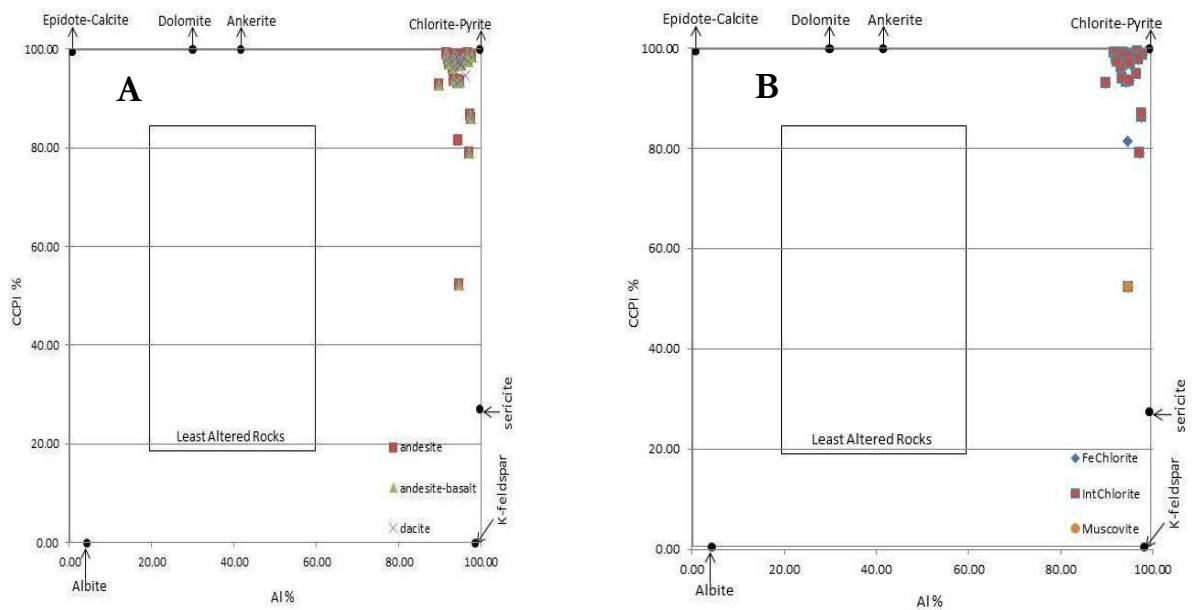


Figure 27: Alteration box plots plotted CCPI (Chlorite Carbonate Pyrite Index) on the Y axis and AI (Ishikawa Alteration Index). A is plotted with lithology, and B is plotted with alteration mineral assemblages.

5. DISCUSSION

5.1. Introduction

The purpose of studying the Coonterunah formation was to determine if ASTER satellite imagery, airborne gamma-ray data and airborne magnetic data can be used to estimate lithology, grade of metamorphism and relative intensity of alteration of the mafic meta-volcanic rocks. The Coonterunah Formation is dominated by mafic and ultramafic meta-volcanic rocks. Whereas the purpose of studying the Duffer formation was to check if the above mentioned datasets used in the Coonterunah Formation can also be used for the felsic meta-volcanics too. The Duffer Formation is dominated by felsic meta-volcanic rocks ranging from andesite, dacite to rhyolite. Moreover the Panorama district was investigated in order to get the information on the response of remote sensing and geophysical datasets towards intense hydrothermal alteration.

The results found from the three transects are compiled together to give a complete information about the variability of the remote sensing and geophysical datasets with lithology, grade of metamorphism, and intensity of hydrothermal alteration. The Coonterunah Formation as it is mentioned above is dominated by mafic volcanics metamorphosed at greenschist to amphibolite facies of metamorphism. This transect can give how the remote sensing and geophysical datasets respond to rocks ranging dominantly from mafic to ultramafic lithologies and rocks metamorphosed in the mentioned range of metamorphism. The Duffer Formation in turn can give information on the response of the remote sensing and geophysical datasets used to area which is mainly dominated by felsic lithologies at greenschist facies of metamorphism since rocks in the Duffer Formation are metamorphosed to greenschist facies. The intensely hydrothermally altered Panorama district was studied in order to get the information on the characteristics of the remote sensing and geophysical datasets in response to intensely hydrothermally altered lithologies.

5.2. ASTER band ratios data interpretation

In this analysis samples from all the transects (Coonterunah, Duffer and Panorama) were used. This gives a complete idea of the response of ASTER band ratio values with lithology. Figure 28B shows the response of ASTER band ratio $(5+7)/6$ values to lithological variations. It shows an increasing trend going from the ultramafic, mafic to felsic lithologies. This is due to variations in mineralogy. Felsic rocks are rich in felsic minerals while ultramafic and mafic rocks are rich in mafic minerals. The ASTER band ratio $(5+7)/6$ is good in detecting felsic minerals such as muscovite and sericite which are present in our study area in different concentrations. This mineralogical variation in different lithologies responds for ASTER band ratio $(5+7)/6$. The richer the rock unit in the above mentioned minerals is the higher the band ratio results. Rhyolite (figure 28B) has the highest band ratio result. This is due to the presence of phengite in this lithology. Illite, muscovite and phengite are responsible for the high band ratio result in dacite. Figure 28C also shows the variability of ASTER band ratio value of $(7+9)/8$ with lithology. It shows a decreasing trend and going from ultramafic, mafic to felsic lithologies. The high band ratio result in komatiite and basalt is due to the presence of Mg-chlorite, hornblende and actinolite.

For the analysis of the response of ASTER band ratios to varying grades of metamorphism, basalt from Coonterunah and Duffer Formations was used. Figure 29B shows the variability of ASTER band ratio result $(5+7)/6$ with metamorphic facies (grade of metamorphism). This band ratio gives higher results in the greenschist facies of metamorphism. Moreover figure 29C shows variability of ASTER band ratio result $(7+9)/8$. Higher band ratio results are apparent in amphibolite facies of metamorphism for this band ratio. The minerals responsible for this result are hornblende, actinolite and Mg-chlorite.

The response of ASTER band ratio to the intensity of alteration was interpreted using andesite from the three transects. The rocks in the Coonterunah and Duffer Formations are altered due to metamorphism and only mineralogical change occurs in such conditions. The rocks in the Panorama district are intensely hydrothermally altered. In intense hydrothermal alteration (metasomatism) rocks change their chemistry and mineralogy. Analysing samples from all the transects gave a complete image of the response of ASTER band ratios with regard to the intensity of alteration. Figure 30C shows the variability of band ratio $(7+9)/8$ with the intensity of alteration. Andesite samples from the intensely hydrothermally altered Panorama district showed higher results than the andesite from Coonterunah and Duffer Formations which consist of altered rocks due to metamorphism only. This is caused by the intense chloritic alteration in this district.

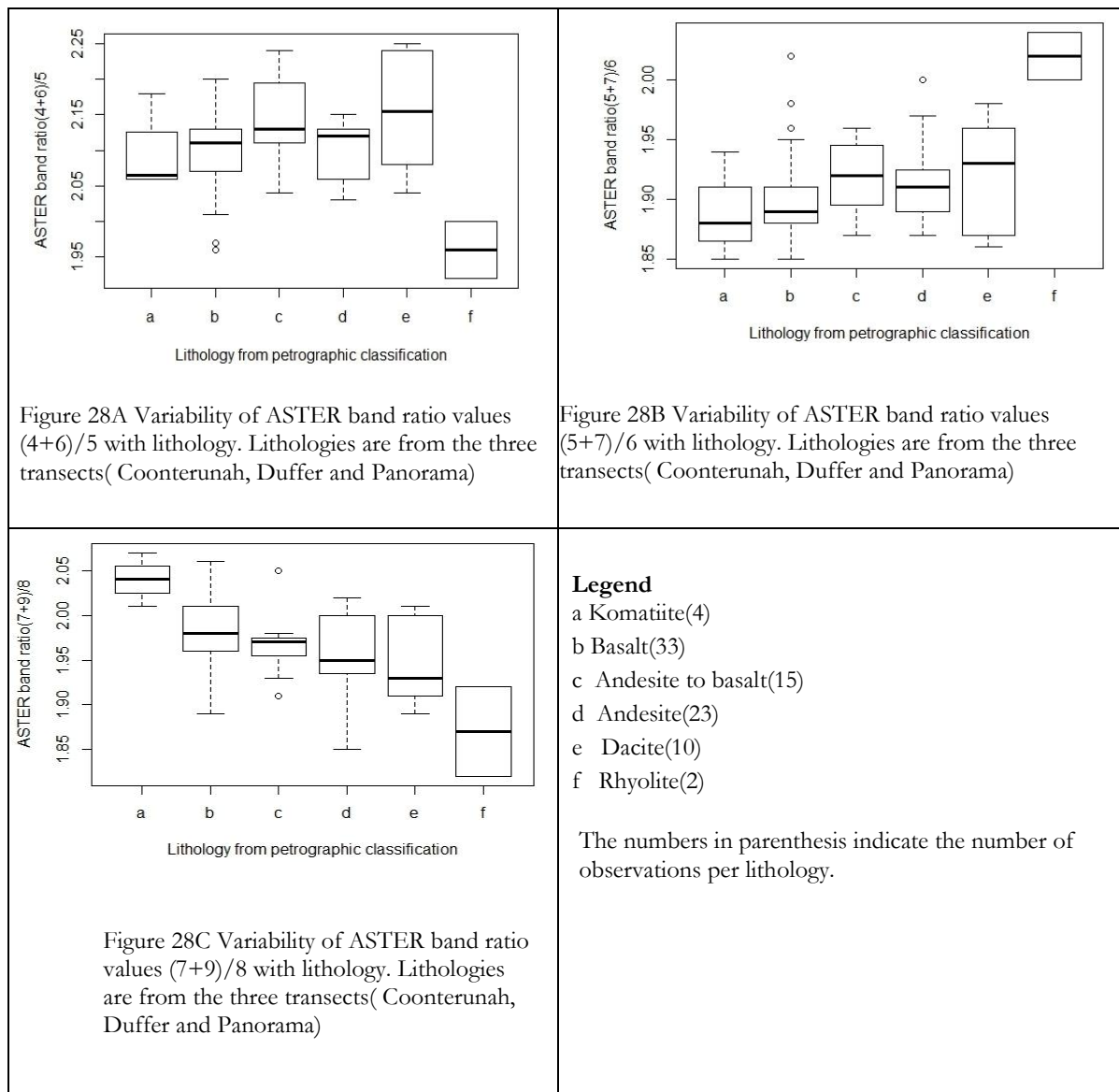


Figure 28: Variability of different band ratio values with lithology

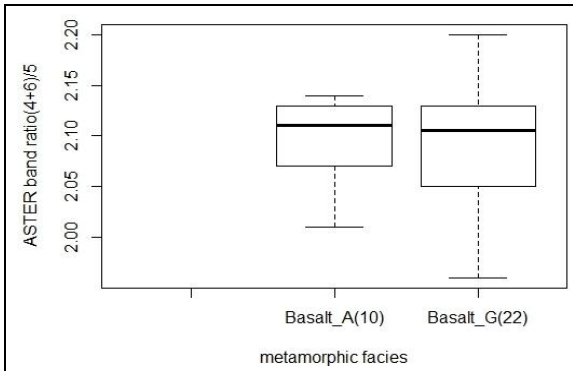


Figure 29A Variability of ASTER band ratio values (4+6)/5 with grade of metamorphism; Observations are from Coonterunah, Duffer Formations(numbers in parenthesis are number of observations)

Basalt_A Basalt at amphibolite facies
 Basalt_G Basalt at greenschist facies

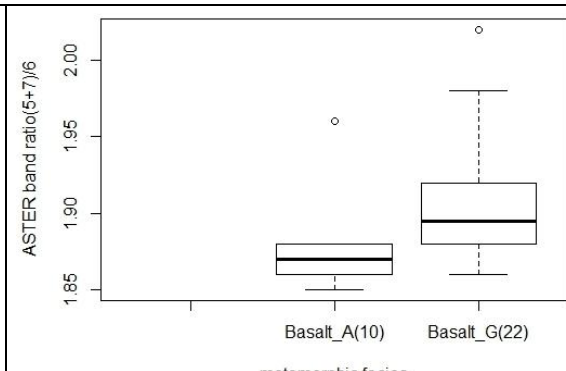


Figure 29B Variability of ASTER band ratio values (5+7)/6 with grade of metamorphism; Observations are from Coonterunah, Duffer Formations(numbers in parenthesis are number of observations)

Basalt_A Basalt at amphibolite facies
 Basalt_G Basalt at greenschist facies

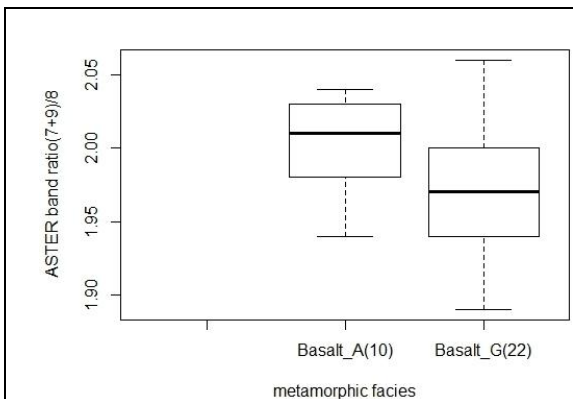


Figure 29C Variability of ASTER band ratio values (7+9)/8 with grade of metamorphism; Observations are from Coonterunah, Duffer Formations(numbers in parenthesis are number of observations)

Figure 29: Variability of different ASTER band ratio values with the grade of metamorphism

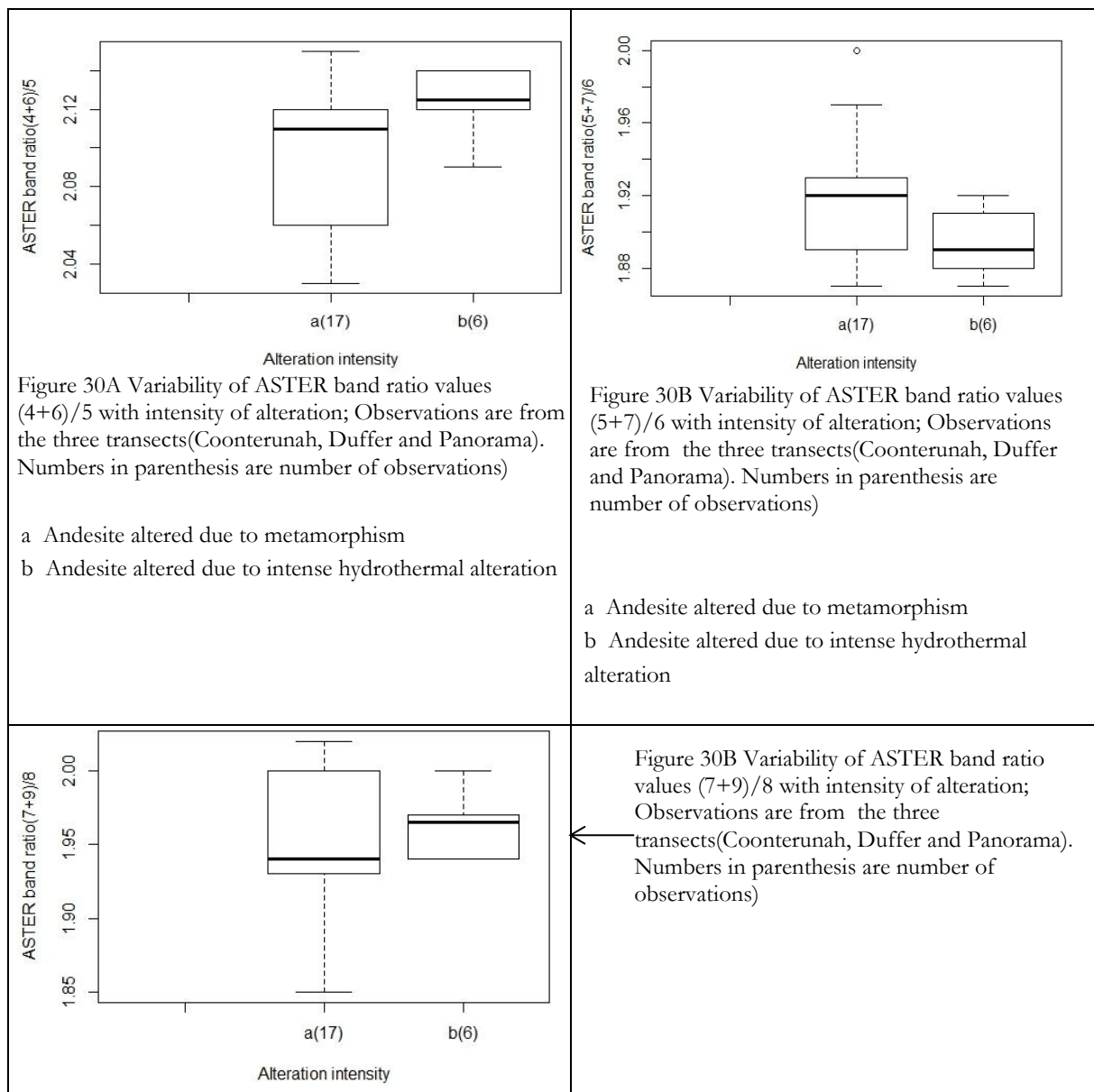


Figure 30: Variability of different ASTER band ratio values with intensity of hydrothermal alteration

5.3. Gamma-ray data interpretation

Figure 31A shows the variability of potassium content from airborne gamma-ray data with lithology (all lithologies used here are from petrographic classification of Smithies et al. (2007)). The K content increases going from ultramafic through mafic to felsic lithologies. This is an expected trend since ultramafic and mafic rocks in nature contain low amount of K and felsic rocks generally contain high amount of K. The same trend is apparent from the ground data. The XRF laboratory result originally was provided in the form of K_2O ; this was recalculated back to K. It also increases going from ultramafic through mafic to felsic rocks. Even though the K from gamma-ray data and the K from XRF data have similar trend the K content of rocks from the XRF data are quite low in comparison to the K contents from the gamma-ray data (figure 32). This is most probably caused by the interpolation errors since the survey line spacing was wide (400m). The flight line direction could also be another cause of the error.

1. **The effect of flight line direction:** The flight line direction affects the amount gamma ray total count received by the sensor in such a way that the survey lines might miss the actual sampled pixels and as a consequence errors arise from interpolation of lines to find the average estimated value of the subsequent sampled pixels.

2. The effect of flight line spacing: When flight lines or survey lines are widely spaced, there is a high probability that they miss the sampled pixels and hence errors arise due to interpolation.

Figure 31B shows the variability of K content of lithologies with the grade of metamorphism. It clearly shows that basalt in the amphibolite grade of metamorphism contain less potassium than basalt in the greenschist facies of metamorphism.

Figure 31C shows the variability of K with intensity of alteration. Potassium content is plotted against andesitic samples from the three studied areas. The altered samples (due to metamorphism) are both from Coonterunah and Duffer Formations. The intensely hydrothermally altered ones are from the Panorama district. The andesitic samples from the Panorama district show lower potassium content than those of the other two formations. The reason for this could most probably be due to the fact that potassium is leached from the rocks under intense hydrothermal alteration. High temperature intense hydrothermal activity causes minerals to change their chemistry (metasomatism).

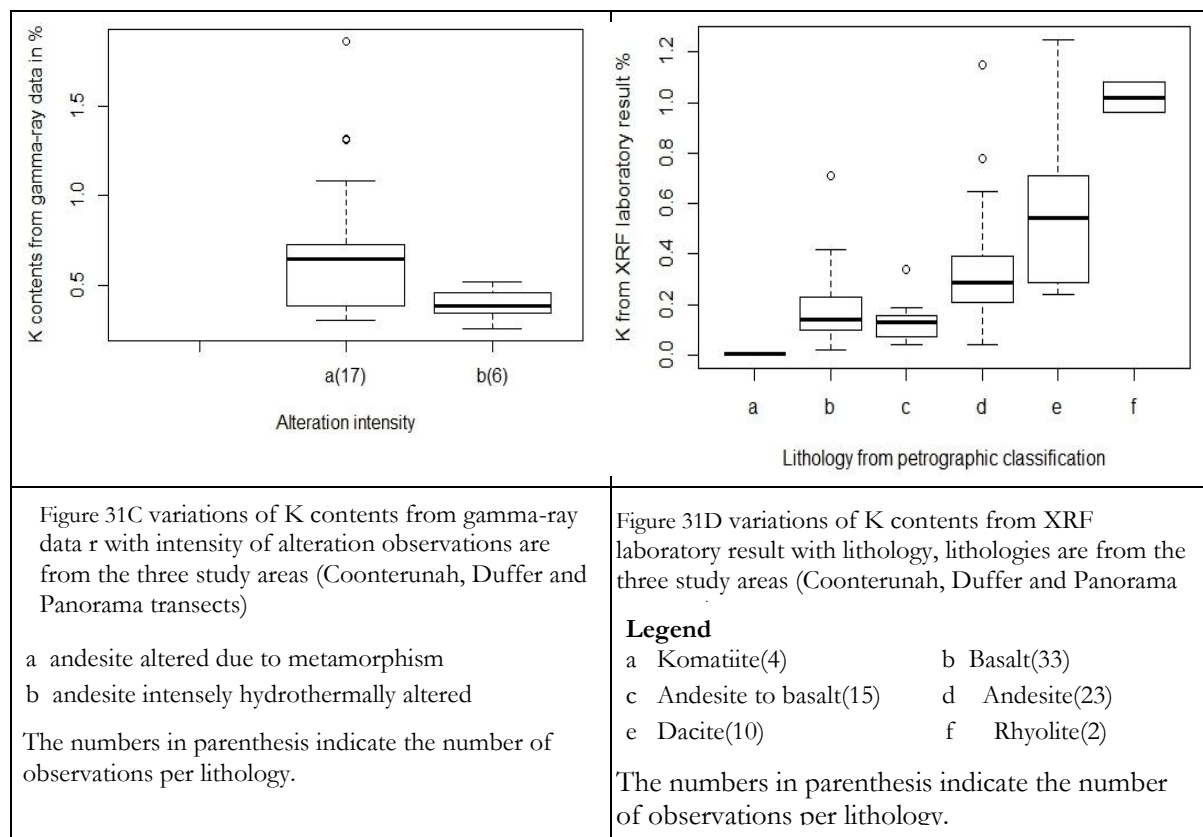
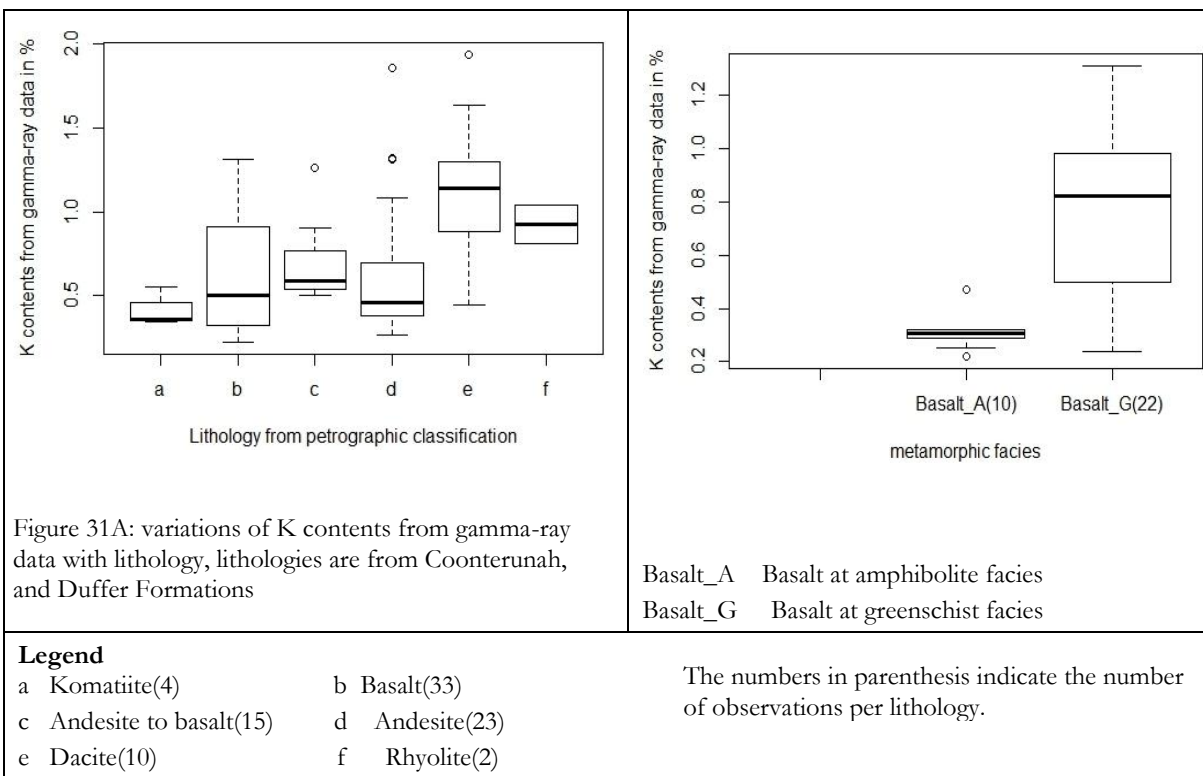


Figure 31: Variability of K contents with lithology, the grade of metamorphism and intensity of hydrothermal alteration

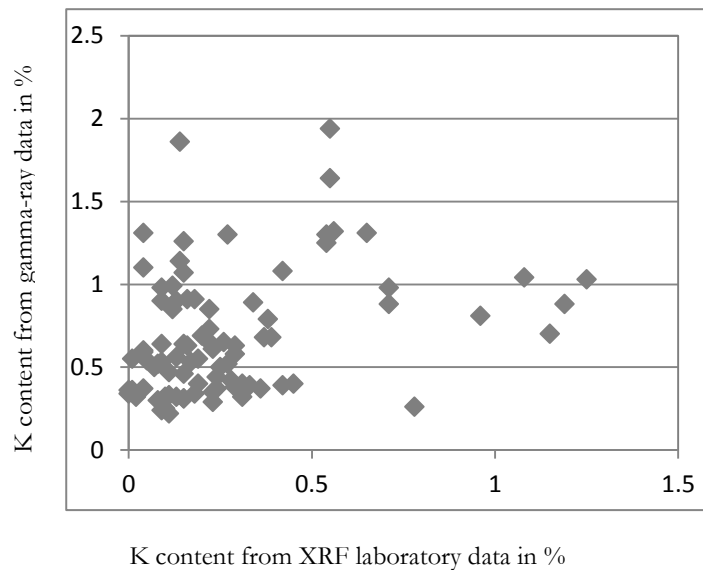


Figure 32: Scatter plot showing the correlation of K contents from XRF laboratory data and airborne gamma-ray data

5.4. Airborne magnetic data interpretation

The 1st vertical derivative of airborne magnetic intensity data was useful in identifying ultramafic rock units and banded iron formations in all the three study areas. Banded iron formations are strongly magnetic and they were easily detected by the vertical derivative of the total magnetic intensity data. Ultramafic rocks such as komatiite and harzburgite respond with high amplitude magnetic anomalies because they are rich in magnetic minerals and this was apparent in our study area. Rocks lose their magnetic behaviour under intense hydrothermal alteration (metasomatism). This is apparent in the box plot (figure 33) which shows the variability of analytical signal of the total magnetic intensity data results. In this box plot it is apparent that the intensely hydrothermally altered andesitic rock samples from the Panorama district have quite low analytical signal results than the ones which are just altered due to metamorphism.

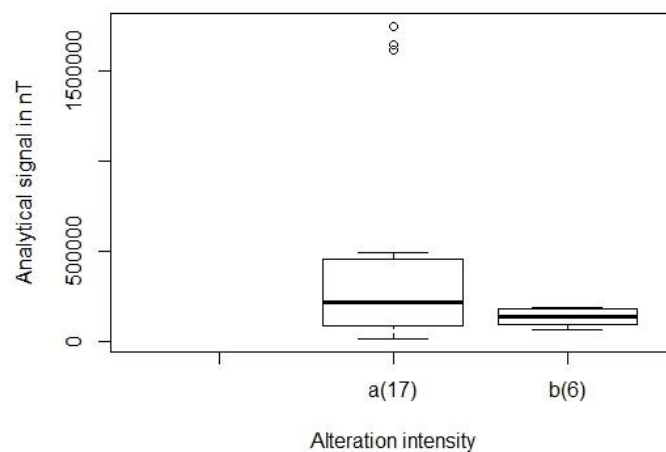


Figure 33: Variability of the analytical signal of the total magnetic intensity data with the intensity of alteration (Numbers in parenthesis are number of observations)

- a andesite altered due to metamorphism
- b andesite intensely hydrothermally altered

6. CONCLUSION AND RECOMMENDATIONS

6.1. Conclusions

- ASTER satellite imagery was found useful in detecting and mapping both mafic and felsic volcanic lithologies depending on their mineralogical variations. Rocks behave differently towards ASTER satellite imagery depending on their mineral content. These variations help in differentiating between different lithologies. ASTER band ratio (Red=4, G=6 and B=8) in the Coonterunah for example mafic to ultramafic rocks show greenish to deep greenish color respectively and felsic ones generally show reddish color. Felsic rocks can also be differentiated well using ASTER satellite imagery. In the RGB color composite image (Red=4, G=6 and B=8) rocks with more felsic nature show generally light reddish to light greenish color and those with andesitic nature show bluish color. The rocks with more felsic nature of lithology in the color composite image of RGB $(4+6)/5$: $(5+7)/6$: $(7+9)/8$ respectively, rocks of more felsic nature respond by giving dominantly reddish color and those of andesitic nature show bright greenish color.
- ASTER band ratio results of $(4+6)/5$, $(5+7)/6$ and $(7+9)/8$ were also found helpful in discriminating between different lithologies. Different band ratios are sensitive to specific minerals present in different lithologies. ASTER band ratio $(5+7)/6$ for example was sensitive to muscovite and $(7+9)/8$ was sensitive to hornblende, actinolite and Mg-chlorite which are present in the studied areas.
- It was also found useful in estimating the grade of metamorphism depending on the characteristic indicator minerals found in the respective metamorphic grade. Greenschist facies of metamorphism is characterized by the metamorphic mineral assemblages such as mainly intermediate chlorite, Fe-chlorite and epidote and the amphibolite facies is characterized by the presence of mainly hornblende, actinolite and Mg-chlorite. These mineral assemblages behave differently towards ASTER satellite imagery. RGB color composite image (Red=4, G=6 and B=8) of the Coonterunah formation (figure 3A) for example shows deep greenish color at amphibolite grade of metamorphism and it shows light greenish to greenish color in the greenschist facies of metamorphism. ASTER band ratio $(7+9)/8$ also gives a good quantitative information where the band ratio results are higher in the amphibolite facies of metamorphism than in the greenschist facies due to the presence of mainly hornblende, actinolite and Mg-chlorite in this facies.
- Intensity of alteration can also be estimated using ASTER satellite imagery. The intensely hydrothermally altered rock units of the Panorama district are dominated by intense chlorite and quartz alteration (Brauhart et al., 1998) alteration minerals. As it was mentioned previously ASTER band ratio $(7+9)/8$ is sensitive in detecting chloritic alterations and hence it shows higher band ratio results (figure 30C) than the rocks which are altered due to metamorphism.
- Airborne Gamma-ray data was found useful in estimating different lithologies depending on their radioelement contents. RGB color composite image (K=Red, Th=Green and U=Blue) was used to detect and map lithologies. Different lithologies at different grades of metamorphism and intensity of hydrothermal alteration have different radioelement contents. It was apparent in the study areas that the rocks in the amphibolite facies of

metamorphism have lower potassium contents than those at the greenschist facies of metamorphism.

- Moreover intensely hydrothermally altered rocks have generally lower potassium contents in our study area than the rocks altered only due to metamorphism. This is due to the leaching of potassium from the respective rock units due to intense high temperature hydrothermal alteration which causes a change in both chemistry and mineralogy of individual rock units.
- Different lithologies at different grades of metamorphism and intensity of hydrothermal alteration have different magnetic susceptibilities depending on the magnetic mineral content of the respective lithologies. In our study area, ultramafic rocks and banded iron Formations show high amplitude magnetic anomalies in the 1st vertical derivative of the total magnetic intensity data. This is obvious since these lithologies in nature are rich in magnetic mineral contents.
- To assess the correlation between the K content from airborne geophysical data and the XRF datasets a scatter plot was made (figure 32). The scatter plot showed that results from airborne geophysical data are not strongly correlated with the XRF laboratory results from the actual field samples. This as discussed in the discussion chapter was caused most probably by the interpolation errors from the flight line spacing and flight line direction. Therefore care should be taken in the interpretation potassium contents from the airborne geophysical data and extrapolation to the ground contents. Better results could have been found if the gamma-ray survey data was not affected by interpolation errors.

6.2. Research limitations

The following are the limitations encountered in the research:

- The extent of the sampled area in the Duffer formation was short. This made the lithological variability of the felsic volcanic lithologies limited; wider sampling range would have provided richer information.
- There was not ground magnetic susceptibility data for the Panorama district. Even though the literature gave clear information that magnetic properties of rocks and minerals get destroyed under intense hydrothermal activity and this is apparent from our airborne magnetic intensity data, it would have been necessary to check it from the ground magnetic susceptibility data too.
- Airborne magnetic data was affected by interpolation errors, better results would have been obtained if the airborne magnetic data happened to be very close to reality i.e. to the XRF laboratory results.
- No hyperspectral image data was available. The results found from multispectral remote sensing would have been better validated using hyperspectral remote sensing methods.

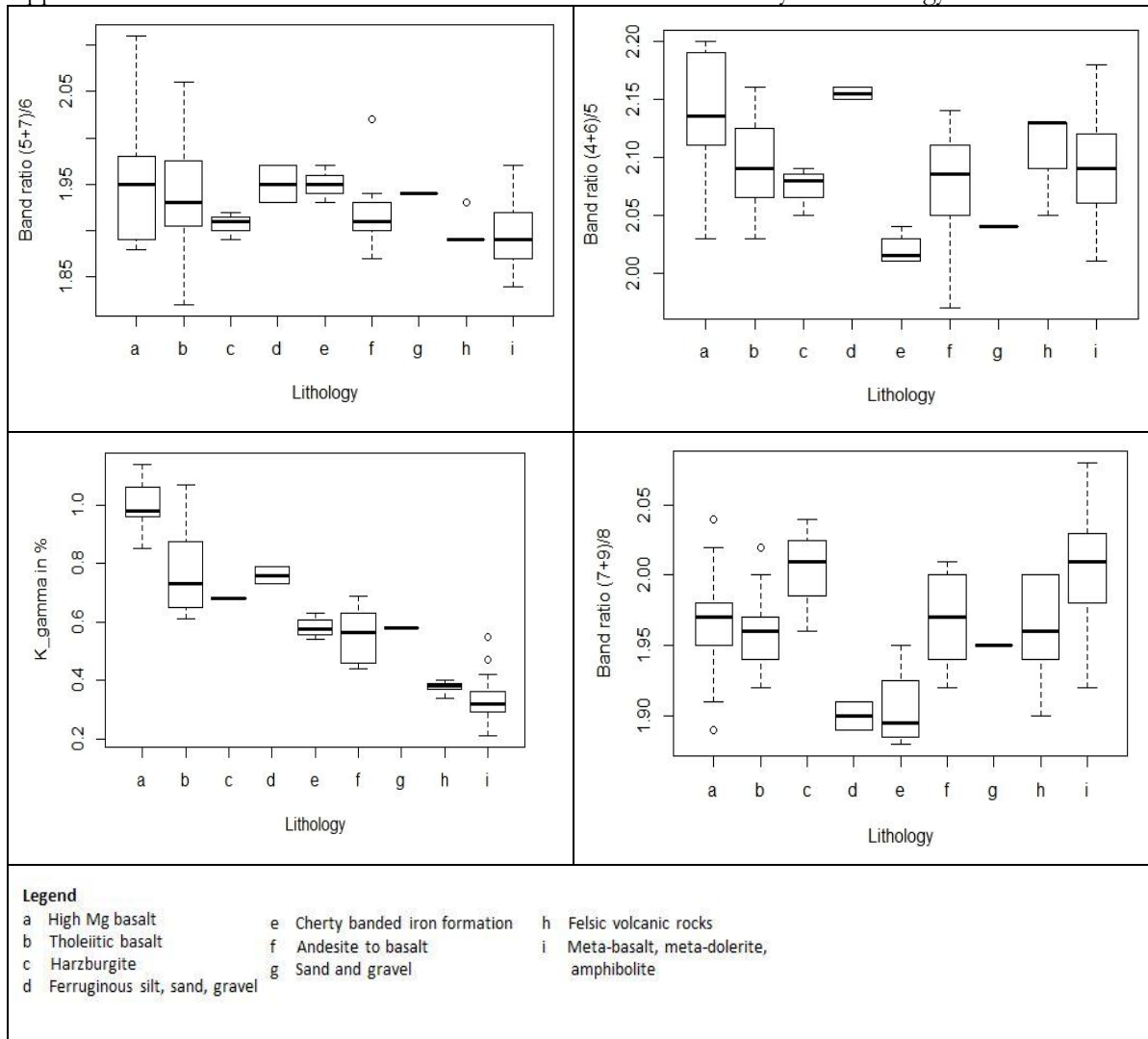
6.3. Recommendations

- More samples should be collected from the felsic volcanic lithologies under different metamorphic grades and alteration intensities to better understand their response to remote sensing and geophysical datasets.
- Hyperspectral remote sensing should be used to compare, evaluate and validate results found from remote sensing and geophysical datasets for improved results.
- Better resolution (narrow survey line spacing) airborne gamma-ray survey data should be used for farther research. Airborne surveys should also be flown in the same direction as the geological traverses to minimize interpolation errors.
- The magnetic susceptibility data of the samples from the Panorama district; which were intensely hydrothermally altered should be collected to verify the magnetic response of volcanic lithologies under high temperature intense hydrothermal alteration.

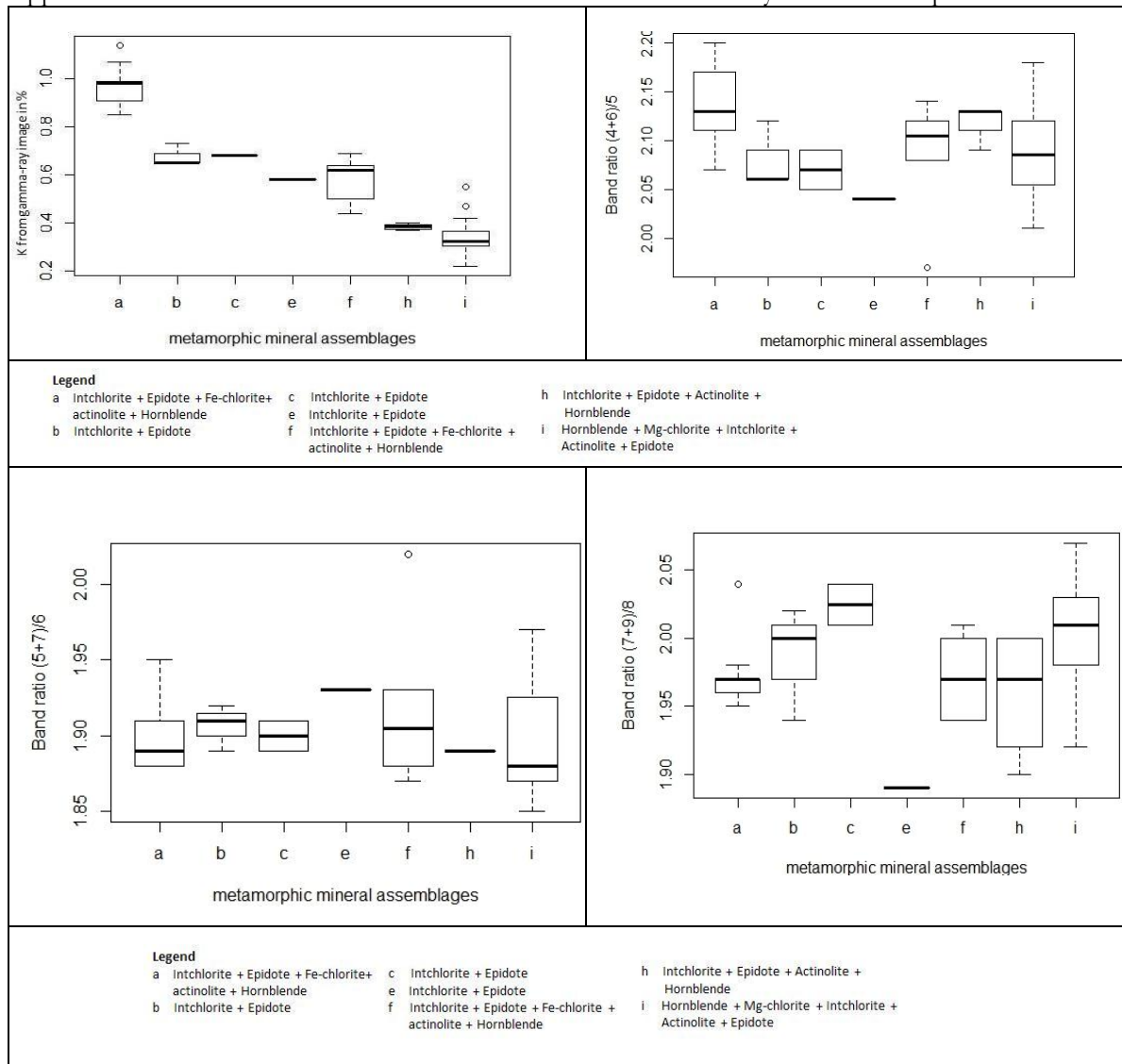
APPENDICES

Coonterunah Formation

Appendix 1A: Potassium value and ASTER band ratio values variability with lithology



Appendix 1B: Potassium value and ASTER band ratio values variability with metamorphism



Appendix 2: Comparison of lithology from geological map and lithology from petrographic classification of Coonterunah Formation (Lith_geol_Map stands for lithology from geological map and Lith-Petro stands for lithology from petrographic classification)

Sample No	Easting	Northing	Lith_geol_Map	Lith-Petro	Matching	score	
179795	715162	7660930	High Mg basalt	Basalt	Matching	100%	
179796	715145	7660983	High Mg basalt	Basalt	Matching		
179797	715122	7661082	High Mg basalt	Basalt	Matching		
179798	715065	7661192	High Mg basalt	Basalt	Matching		
179799	715004	7661288	High Mg basalt	Basalt	Matching		
179800	714831	7661854	High Mg basalt	Basalt	Matching		
179801	715001	7661921	High Mg basalt	Basalt	Matching		
179802	714983	7661983	High Mg basalt	Basalt	Matching		
179803	714973	7661991	High Mg basalt	Basalt	Matching		
179791	715722	7662818	Tholeiitic basalt	Andesite	Not matching		0%
179792	715700	7662882	Tholeitic basalt	Andesite	Not matching		
179794	715646	7662881	Tholeitic basalt	Andesite	Not matching		
179789	715895	7663227	Harzburgite	Basalt	Highly matching	100%	
179790	715873	7663258	Harzburgite	Basalt	Highly matching		
179787	716716	7663784	Banded Iron Formation	Dacite	Not matching	0%	
179785	716702	7663911	Andesit/Basalt	Basalt	similar	83.3%	
179783	716777	7664113	Andesit/Basalt	Andesite	similar		
179784	716802	7664108	Andesit/Basalt	Andesite	similar		
179782	716865	7664216	Andesit/Basalt	Basalt	similar		
179780	717066	7664492	Andesit/Basalt	Basalt	similar		
179779	717084	7664667	Andesit/Basalt	Dacite	Matching		
179777	717157	7664736	Felsic volcanic rocks	Andesite	Matching		75%
179778	717076	7664775	Felsic volcanic rocks	Andesite	Matching		
179775	717208	7664864	Felsic volcanic rocks	Andesite	Matching		
179776	717205	7664869	Felsic volcanic rocks	Basalt	Not matching		
179774	717760	7665248	meta-Basalt,meta-dolorite, amphibolite	Andesite	Not matching		
179773	717766	7665381	meta-Basalt,meta-dolorite, amphibolite	Andesite	Not matching		
179772	717831	7665473	meta-Basalt,meta-dolorite, amphibolite	Basalt	Matching		
179771	717850	7665511	meta-Basalt,meta-dolorite, amphibolite	Andesite	Not matching		
179770	718008	7665655	meta-Basalt,meta-dolorite, amphibolite	Basalt	Matching		
179767	718033	7665691	meta-Basalt,meta-dolorite, amphibolite	Basalt	Matching		
179766	717967	7665764	meta-Basalt,meta-dolorite, amphibolite	Basalt	Matching		
179768	718315	7665818	meta-Basalt,meta-dolorite, amphibolite	Basalt	Matching		
179769	718315	7665818	meta-Basalt,meta-dolorite, amphibolite	Basalt	Matching		
179765	717975	7666236	meta-Basalt,meta-dolorite, amphibolite	Basalt	Matching		
179764	717888	7666340	meta-Basalt,meta-dolorite, amphibolite	Basalt	Matching		
179763	717797	7666567	meta-Basalt,meta-dolorite, amphibolite	Basalt	Matching		
179762	717439	7666661	meta-Basalt,meta-dolorite, amphibolite	Basalt	Matching		
179761	717429	7666667	meta-Basalt,meta-dolorite, amphibolite	Andesite	Not matching		
179759	717632	7666885	meta-Basalt,meta-dolorite, amphibolite	Basalt	Matching		
179758	717652	7666983	meta-Basalt,meta-dolorite, amphibolite	Basalt	Matching		
179757	717584	7667193	meta-Basalt,meta-dolorite, amphibolite	Komatiite	Matching		
179756	717571	7667384	meta-Basalt,meta-dolorite, amphibolite	Komatiite	Matching		
179755	717572	7667394	meta-Basalt,meta-dolorite, amphibolite	Komatiite	Matching		
179753	717486	7667533	meta-Basalt,meta-dolorite, amphibolite	Basalt	Matching		
179754	717401	7667555	meta-Basalt,meta-dolorite, amphibolite	Basalt	Matching		
179752	717460	7667718	meta-Basalt,meta-dolorite, amphibolite	Basalt	Matching		
179751	717483	7667755	meta-Basalt,meta-dolorite, amphibolite	Komatiite	Matching	83.3%	

Appendix 3: XRF laboratory data

Sample_No	SAMPLNR	EW-Cor	NS-Cor	Litho_Geol_Map_summarized	Based on Spectroscopy	Lithology	Alt. Index	CCPI Index	Nb/Y	Zr/TiO2	SiO2	MgO
179791	BJ04/069	715722	7662818	Tholeiitic basalt		Andesite	27.72	67.02	0.413	0.023	56.60	3.41
179792	BJ04/067	715700	7662882	basalt	IntChlorite + Epidote	Andesite	33.36	71.00	0.438	0.023	53.44	4.27
179794	BJ04/066	715646	7662881	basalt	IntChlorite + Epidote	Andesite	31.22	70.31	0.434	0.023	54.79	4.02
179783	BJ04/074	716777	7664113	Andesite/basalt	IntChlorite + Actinolite + Hornblende	Andesite	24.30	66.72	0.328	0.024	58.33	2.64
179784	BJ04/075	716802	7664108	Andesite/basalt	Fe-Chlorite	Andesite	34.28	77.48	0.397	0.016	54.55	4.47
179777	BJ04/062	717157	7664736	Felsic Volcanic Rocks	IntChlorite + Epidote	Andesite	28.43	70.34	0.362	0.023	54.52	2.78
179778		717076	7664775	Felsic Volcanic Rocks	IntChlorite + Actinolite + Hornblende	Andesite	21.83	62.34	0.226	0.023	59.57	2.18
179775	BJ04/061	717208	7664864	Felsic Volcanic Rocks	IntChlorite + Actinolite + Hornblende	Andesite	28.13	67.59	0.301	0.026	60.03	3.17
179774	BJ04/101	717760	7665248	Meta-basalt,Meta-dolerite,Amphibolite	IntChlorite + Epidote	Andesite	23.86	70.22	0.307	0.019	59.35	2.74
179773	BJ04/100	717766	7665381	Meta-basalt,Meta-dolerite,Amphibolite	IntChlorite + Actinolite + Hornblende	Andesite	34.31	70.80	0.324	0.035	59.34	3.89
179771	BJ04/098	717850	7665511	Meta-basalt,Meta-dolerite,Amphibolite	IntChlorite + Actinolite + Hornblende	Andesite	28.15	75.07	0.329	0.015	53.67	4.25
179761	BJ04/092	717429	7666667	Meta-basalt,Meta-dolerite,Amphibolite	IntChlorite + Actinolite + Hornblende	Andesite	26.02	69.80	0.333	0.018	56.47	3.17
179795	NONE	715162	7660930	High Mg-basalt	IntChlorite + Epidote	Basalt	40.04	85.54	0.202	0.006	48.10	8.42
179796	NONE	715145	7660983	High Mg-basalt	Fe-Chlorite	Basalt	36.63	84.23	0.252	0.006	47.72	7.82
179797	NONE	715122	7661082	High Mg-basalt	Fe-Chlorite	Basalt	37.16	81.37	0.249	0.007	47.83	7.66
179798	NONE	715065	7661192	High Mg-basalt	IntChlorite + Epidote	Basalt	33.43	85.00	0.229	0.007	47.20	7.02
179799	NONE	715004	7661288	High Mg-basalt	IntChlorite + Epidote	Basalt	38.50	79.28	0.286	0.007	49.07	7.65
179800	NONE	714831	7661854	High Mg-basalt	IntChlorite + Actinolite + Hornblende	Basalt	27.45	72.43	0.214	0.006	49.39	4.26
179801	NONE	715001	7661921	High Mg-basalt	IntChlorite + Epidote	Basalt	33.63	81.91	0.177	0.006	47.61	5.86
179802	NONE	714983	7661983	High Mg-basalt	IntChlorite + Epidote	Basalt	31.45	79.11	0.134	0.006	45.41	5.47
179803	NONE	714973	7661991	High Mg-basalt	Fe-Chlorite	Basalt	48.68	84.25	0.365	0.007	48.58	5.01
179789	BJ04/070	715895	7663227	harzburgite	IntChlorite + Epidote	Basalt	41.33	84.76	0.314	0.006	46.47	7.22
179790	BJ04/071	715873	7663258	harzburgite	IntChlorite + Epidote	Basalt	41.60	93.95	0.323	0.010	45.85	6.15
179785	NONE	716702	7663911	Andesite/basalt	IntChlorite + Epidote	Basalt	30.40	78.22	0.319	0.014	53.69	4.58
179782	BJ04/076	716865	7664216	Andesite/basalt	IntChlorite + Epidote	Basalt	24.12	80.23	0.323	0.012	55.85	2.55
179780	BJ04/064	717066	7664492	Andesite/basalt	IntChlorite + Actinolite + Hornblende	Basalt	27.02	84.27	0.287	0.009	48.26	4.10
179776	BJ04/060	717205	7664869	Felsic Volcanic Rocks	IntChlorite + Actinolite + Hornblende	Basalt	28.68	75.69	0.244	0.012	53.88	4.38
179772	BJ04/099	717831	7665473	Meta-basalt,Meta-dolerite,Amphibolite	IntChlorite + Actinolite + Hornblende	Basalt	25.51	84.87	0.122	0.007	49.04	4.02
179770	NONE	718008	7665655	Meta-basalt,Meta-dolerite,Amphibolite	IntChlorite + Actinolite + Hornblende	Basalt	23.44	80.89	0.139	0.009	51.87	3.77
179767	BJ04/097	718033	7665691	Meta-basalt,Meta-dolerite,Amphibolite	Hornblende + Mg-Chlorite	Basalt	33.61	84.21	0.111	0.006	49.74	6.47
179766	NONE	717967	7665764	Meta-basalt,Meta-dolerite,Amphibolite	Hornblende + Mg-Chlorite	Basalt	31.73	86.83	0.129	0.005	48.80	6.32
179768	BJ04/081	718315	7665818	Meta-basalt,Meta-dolerite,Amphibolite	IntChlorite + Actinolite + Hornblende	Basalt	36.59	87.00	0.116	0.006	48.86	7.12
179769	NONE	718315	7665818	Meta-basalt,Meta-dolerite,Amphibolite	IntChlorite + Actinolite + Hornblende	Basalt	42.75	82.69	0.128	0.006	49.34	8.65
179765	BJ04/096	717975	7666236	Meta-basalt,Meta-dolerite,Amphibolite	Hornblende + Mg-Chlorite	Basalt	34.21	83.06	0.128	0.005	49.86	6.63
179764	BJ04/095	717888	7666340	Meta-basalt,Meta-dolerite,Amphibolite	IntChlorite + Actinolite + Hornblende	Basalt	31.78	85.35	0.166	0.006	48.54	6.02
179763	BJ04/094	717797	7666567	Meta-basalt,Meta-dolerite,Amphibolite	IntChlorite + Epidote	Basalt	63.82	88.56	0.291	0.007	48.20	6.74
179762	BJ04/093	717439	7666661	Meta-basalt,Meta-dolerite,Amphibolite	IntChlorite + Actinolite + Hornblende	Basalt	30.18	86.51	0.187	0.007	48.78	5.50
179760	BJ04/091	717618	7666836	Meta-basalt,Meta-dolerite,Amphibolite	IntChlorite + Actinolite + Hornblende	Basalt	31.54	87.53	0.186	0.007	49.38	5.54
179759	BJ04/090	717632	7666885	Meta-basalt,Meta-dolerite,Amphibolite	IntChlorite + Epidote	Basalt	21.59	77.52	0.199	0.006	53.26	2.85
179758	BJ04/089	717652	7666983	Meta-basalt,Meta-dolerite,Amphibolite	Hornblende + Mg-Chlorite	Basalt	45.18	83.97	0.164	0.007	51.83	7.72
179753	BJ04/085	717486	7667533	Meta-basalt,Meta-dolerite,Amphibolite	IntChlorite + Epidote	Basalt	26.27	83.19	0.158	0.006	48.74	3.97
179754	BJ04/084	717401	7667555	Meta-basalt,Meta-dolerite,Amphibolite		Basalt	24.81	86.48	0.181	0.007	49.22	3.94
179752	BJ04/083	717460	7667718	Meta-basalt,Meta-dolerite,Amphibolite	Hornblende + Mg-Chlorite	Basalt	50.98	94.63	0.149	0.007	47.80	13.65
179787	NONE	716716	7663784	Cherty banded Iron formation	IntChlorite + Epidote	Dacite	23.65	64.95	0.358	0.031	58.28	2.49
179779	BJ04/063 A+B	717084	7664667	Andesite/basalt	IntChlorite + Actinolite + Hornblende	Dacite	24.11	61.12	0.304	0.029	60.15	2.70
179757	BJ04/088	717584	7667193	Meta-basalt,Meta-dolerite,Amphibolite	Hornblende + Mg-Chlorite	Komatite	90.97	99.92	0.108	0.005	41.49	29.95
179756	BJ04/087	717571	7667384	Meta-basalt,Meta-dolerite,Amphibolite	Hornblende + Mg-Chlorite	Komatite	83.50	99.75	0.125	0.006	43.67	26.92
179755	BJ04/086	717572	7667394	Meta-basalt,Meta-dolerite,Amphibolite	Hornblende + Mg-Chlorite	Komatite	74.14	99.37	0.125	0.006	46.64	22.89
179751	BJ04/082 A+B	717483	7667755	MbMdAm	Hornblende + Mg-Chlorite	Komatite	75.65	99.19	0.138	0.007	45.63	21.95

Continued

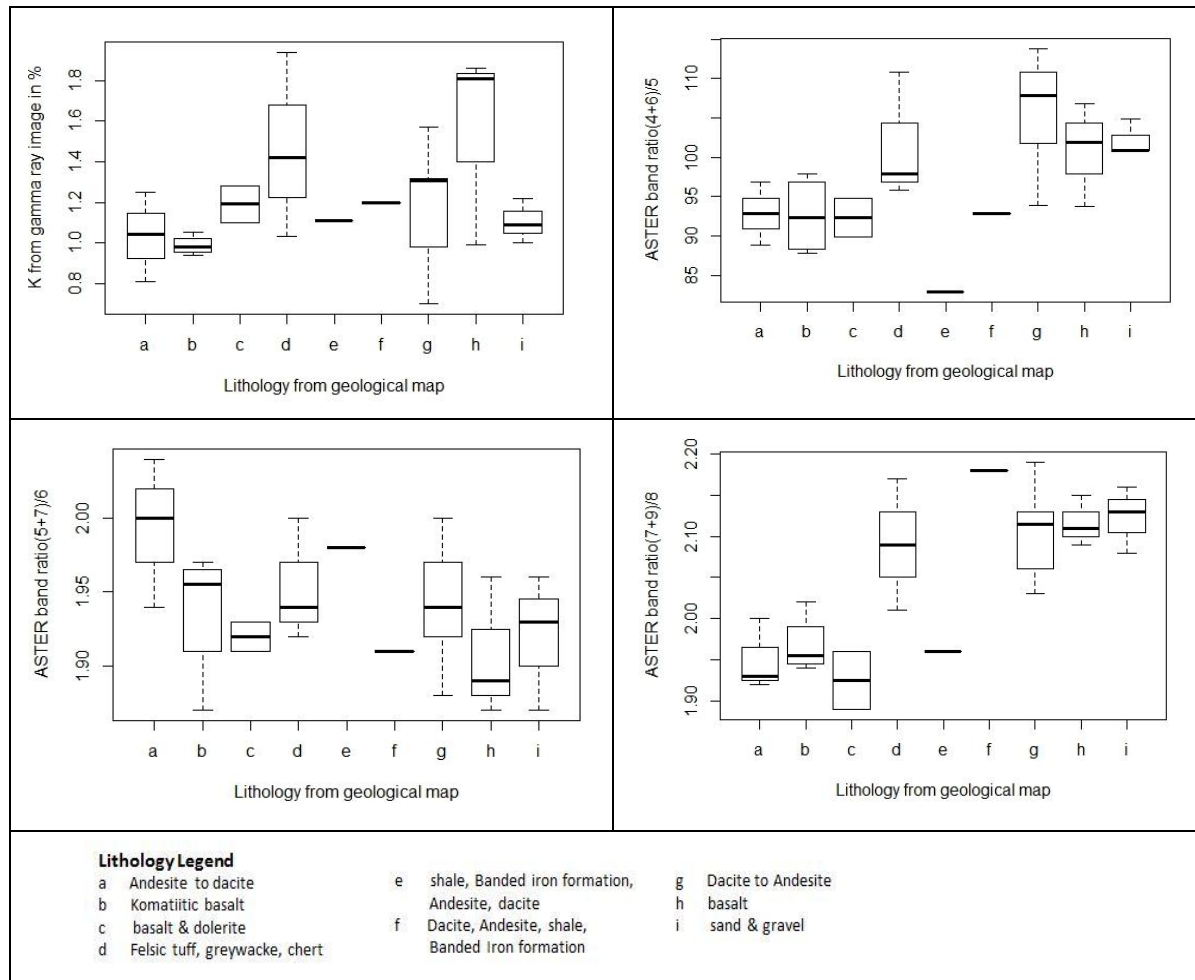
Sample_No	SiO2	TiO2	Al2O3	Fe2O3	FeO	MgO	CaO	MnO	K2O	Na2O	Na2O	P2O5	LOI_free	LOI	Total
179791	56.60	1.34	15.95	10.37	7.15	3.41	5.60	0.19	0.53	4.67	4.67	0.36	99.02	1.64	100.66
179792	53.44	1.43	15.24	10.74	7.41	4.27	5.38	0.19	0.54	4.23	4.23	0.44	95.91	4.82	100.73
179794	54.79	1.46	15.80	11.64	8.03	4.02	5.79	0.24	0.63	4.46	4.46	0.56	99.39	1.40	100.79
179783	58.33	0.92	16.17	8.60	5.93	2.64	6.86	0.18	0.71	3.56	3.56	0.23	98.19	2.38	100.57
179784	54.55	1.16	14.80	10.14	6.99	4.47	6.65	0.22	0.49	2.84	2.84	0.24	95.54	5.17	100.71
179777	54.52	1.30	15.55	11.34	7.82	2.78	6.36	0.15	1.09	3.38	3.38	0.42	96.89	3.96	100.85
179778	59.57	0.91	16.29	8.37	5.77	2.18	6.65	0.12	0.80	4.01	4.01	0.21	99.10	1.47	100.57
179775	60.03	0.76	15.61	7.40	5.10	3.17	6.61	0.11	0.70	3.27	3.27	0.17	97.82	2.67	100.49
179774	59.35	1.04	15.93	8.69	5.99	2.74	6.98	0.17	0.47	3.24	3.24	0.21	98.80	1.82	100.61
179773	59.34	0.66	14.11	7.88	5.43	3.89	6.13	0.13	0.87	2.98	2.98	0.20	96.17	3.82	99.99
179771	53.67	1.13	15.35	10.70	7.38	4.25	8.33	0.21	0.38	3.49	3.49	0.21	97.71	3.10	100.80
179761	56.47	0.82	17.64	7.70	5.31	3.17	8.21	0.13	0.75	2.92	2.92	0.15	97.96	2.53	100.49
179795	48.10	0.97	15.52	11.00	7.58	8.42	11.23	0.17	0.53	2.17	2.17	0.09	98.20	2.31	100.51
179796	47.72	0.89	15.41	10.80	7.45	7.82	11.45	0.16	0.28	2.58	2.58	0.08	97.20	3.42	100.61
179797	47.83	1.08	15.47	11.70	8.07	7.66	10.52	0.18	0.43	3.17	3.17	0.10	98.14	2.53	100.67
179798	47.20	1.16	15.44	11.61	8.00	7.02	12.44	0.18	0.37	2.28	2.28	0.11	97.81	2.76	100.56
179799	49.07	1.15	15.52	11.53	7.96	7.65	9.02	0.18	0.34	3.74	3.74	0.11	98.30	2.23	100.53
179800	49.39	1.37	13.30	13.51	9.31	4.26	7.53	0.22	0.39	4.78	4.78	0.14	94.87	5.82	100.69
179801	47.61	1.48	13.71	14.15	9.76	5.86	8.98	0.26	0.29	3.16	3.16	0.14	95.64	5.14	100.78
179802	45.41	1.40	13.48	13.51	9.32	5.47	8.75	0.23	0.23	3.68	3.68	0.14	92.30	8.70	101.00
179803	48.58	1.58	13.14	17.18	11.85	5.01	5.65	0.19	1.71	1.44	1.44	0.16	94.64	6.73	101.37
179789	46.47	2.00	14.97	15.35	10.59	7.22	9.24	0.24	0.91	2.30	2.30	0.14	98.85	2.20	101.04
179790	45.85	1.42	11.41	13.44	9.27	6.15	9.94	0.25	0.96	0.04	0.04	0.15	89.61	11.33	100.94
179785	53.69	1.50	14.70	12.74	8.78	4.58	8.59	0.24	0.56	3.17	3.17	0.33	100.07	0.85	100.92
179782	55.85	1.83	14.07	15.82	10.91	2.55	5.61	0.44	0.22	3.10	3.10	0.35	99.84	1.27	101.10
179780	48.26	1.36	15.08	14.87	10.26	4.10	10.68	0.27	0.62	2.06	2.06	0.21	97.49	3.64	101.13
179776	53.88	1.09	15.67	10.31	7.11	4.38	9.24	0.20	0.58	3.11	3.11	0.14	98.59	2.15	100.74
179772	49.04	1.51	13.71	17.16	11.84	4.02	9.93	0.32	0.26	2.56	2.56	0.15	98.66	2.67	101.33
179770	51.87	1.19	15.63	12.99	8.96	3.77	10.92	0.26	0.38	2.63	2.63	0.11	99.74	1.19	100.93
179767	49.74	1.04	14.38	14.49	9.99	6.47	10.41	0.24	0.24	2.85	2.85	0.08	99.94	1.12	101.05
179766	48.80	0.94	13.91	14.81	10.21	6.32	11.72	0.26	0.20	2.31	2.31	0.06	99.33	1.78	101.11
179768	48.86	1.01	14.19	13.46	9.28	7.12	11.40	0.23	0.56	1.90	1.90	0.08	98.80	2.17	100.96
179769	49.34	0.94	14.64	12.88	8.88	8.65	8.41	0.20	0.21	3.46	3.46	0.08	98.79	2.12	100.91
179765	49.86	0.97	13.83	14.88	10.27	6.63	10.03	0.28	0.25	3.20	3.20	0.06	99.99	1.11	101.10
179764	48.54	1.05	13.46	14.42	9.94	6.02	11.01	0.25	0.26	2.48	2.48	0.07	97.56	3.52	101.08
179763	48.20	1.33	15.95	18.66	12.87	6.74	1.64	0.14	0.22	2.31	2.31	0.12	95.31	6.17	101.48
179762	48.78	1.11	14.65	14.16	9.76	5.50	11.38	0.25	0.31	2.07	2.07	0.10	98.29	2.73	101.03
179760	49.38	1.50	14.13	16.46	11.35	5.54	10.41	0.31	0.25	2.16	2.16	0.14	100.28	0.98	101.26
179759	53.26	1.56	16.81	11.75	8.10	2.85	9.18	0.35	0.43	2.75	2.75	0.19	99.11	1.70	100.82
179758	51.83	1.36	14.35	14.74	10.16	7.72	6.08	0.26	0.06	3.36	3.36	0.13	99.87	1.26	101.13
179753	48.74	1.51	14.25	14.56	10.04	3.97	12.18	0.26	1.02	1.81	1.81	0.12	98.41	2.15	100.56
179754	49.22	1.61	14.15	15.51	10.70	3.94	12.35	0.33	0.67	1.62	1.62	0.15	99.54	1.54	101.08
179752	47.80	0.68	9.51	13.13	9.05	13.65	12.38	0.21	0.28	1.01	1.01	0.06	98.70	1.95	100.64
179787	58.28	0.84	15.70	8.17	5.63	2.49	6.59	0.12	0.70	3.69	3.69	0.27	96.83	3.71	100.54
179779	60.15	0.66	15.82	6.46	4.45	2.70	6.32	0.09	0.57	3.98	3.98	0.16	96.90	3.53	100.44
179757	41.49	0.22	5.03	10.18	7.02	29.95	2.95	0.15	0.01	0.02	0.02	0.02	90.02	9.71	99.74
179756	43.67	0.25	5.74	10.03	6.92	26.92	5.24	0.14	0.01	0.08	0.08	0.02	92.10	7.64	99.74
179755	46.64	0.27	6.48	9.76	6.73	22.89	7.82	0.17	0.02	0.17	0.17	0.02	94.23	5.89	100.12
179751	45.63	0.38	7.62	11.39	7.86	21.95	6.86	0.17	0.03	0.21	0.21	0.03	94.28	5.95	100.22

Continued

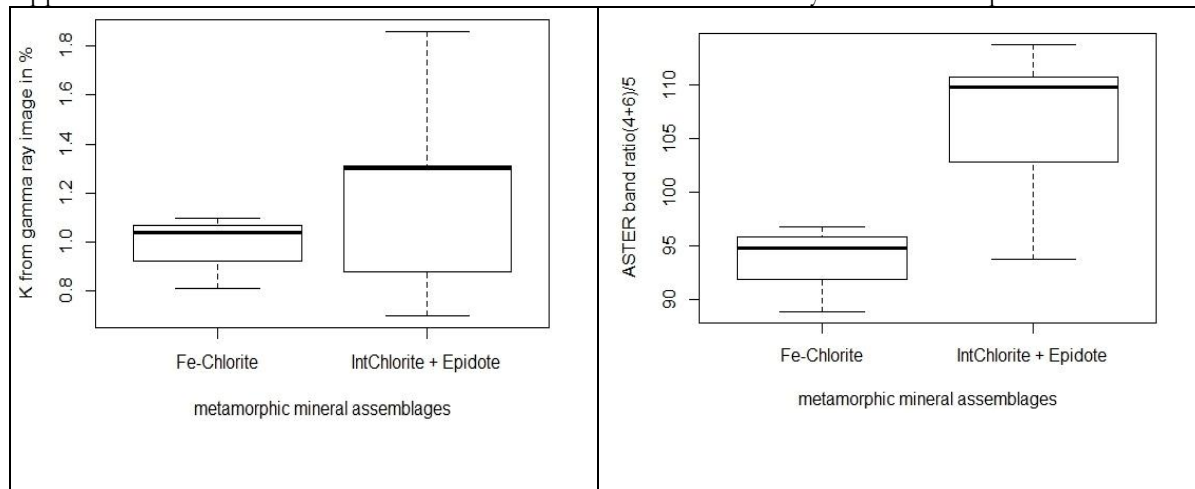
Sample_No	Th	U	Cr	Ni	Sc	V	Cu	Zn	Mo	Sn	Rb	Cs	Ba	Sr	Ga	Ta	Nb	Hf	Zr	Y	Th	U	Pb
179791	3.1	0.7	38	45	19	113	78	95	1.3	1	9.1	0.32	102	159	20.5	1.1	18	7.3	311	43.6	3.1	0.74	3
179792	2.7	0.6	80	57	20	114	10	96	1.4	0.9	9.5	0.19	94	140	20.2	1.2	20.9	7.7	329	47.7	2.7	0.62	3
179794	3.9	0.8	61	40	19	102	6	90	1.3	1.3	11.5	0.23	118	174	20.5	1.3	21.2	8	331	48.9	3.9	0.79	4
179783	5.0	1.0	21	35	18	114	36	98	1.1	2.2	16.8	1.07	119	179	20.2	0.7	11.2	4.7	219	34.1	5	1	5
179784	4.2	0.8	330	114	22	138	8	118	0.7	1.9	11.3	1.3	70	186	19.6	0.8	12.2	4.3	190	30.7	4.2	0.84	6
179777	4.5	0.9	35	41	19	129	9	145	1.1	2.3	33.2	0.98	247	218	21.1	1	19.9	6	294	55	4.5	0.92	5
179778	4.7	1.1	29	33	19	111	7	102	0.5	1.5	24.8	1.31	200	138	20.6	0.6	9.4	4.4	208	41.6	4.7	1.06	5
179775	5.1	1.1	130	72	19	109	10	86	0.7	2.4	28.1	1.02	168	170	18.7	0.6	9	4.4	198	29.9	5.1	1.11	5
179774	4.4	0.9	93	56	18	114	12	96	1.1	1.6	17.6	1.81	86	167	20.6	0.6	9.4	4.3	193	30.6	4.4	0.94	5
179773	6.1	1.2	307	106	18	92	9	116	0.8	2.1	32.4	1.77	225	156	18.5	0.7	11.2	4.8	227	34.6	6.1	1.18	5
179771	3.9	0.9	157	75	23	169	10	115	0.8	2	17	0.94	91	148	19.4	0.6	9.9	3.7	172	30.1	3.9	0.89	5
179761	4.5	0.9	91	67	19	123	38	104	0.9	1.8	37.1	1.76	122	178	20	0.5	8.1	3.4	151	24.3	4.5	0.87	5
179795	0.9	0.2	367	172	23	256	87	75	1	1.2	9.1	0.35	176	141	17.2	-0.1	3.6	2	62	17.8	0.9	0.21	5
179796	0.7	0.2	383	179	23	243	87	75	0.8	1.2	5.9	0.32	85	139	17.4	-0.1	3.4	1.8	56	13.5	0.7	0.18	4
179797	1.0	0.3	339	168	24	264	86	85	0.7	1.2	7.9	0.31	168	134	20	0.2	4.5	2.4	74	18.1	1	0.25	4
179798	1.4	0.3	343	165	26	284	84	78	0.8	1.5	7	0.29	159	143	20.6	0.2	5.1	2.6	83	22.3	1.4	0.34	4
179799	1.0	0.3	326	164	22	276	82	83	1	1.5	5.8	0.31	160	121	17.5	0.3	5	2.9	84	17.5	1	0.34	4
179800	0.5	0.2	278	78	30	362	106	112	0.9	1.4	7.9	0.37	27	59	18.6	0.2	4.4	2.9	82	20.6	0.5	0.16	4
179801	0.6	0.2	307	78	33	381	104	112	1.1	2	5.5	0.21	16	152	20.2	0.2	4.7	2.9	86	26.6	0.6	0.16	4
179802	0.7	0.2	325	80	33	396	104	126	0.8	1.6	4	0.54	30	44	18	0.1	4.1	2.7	82	30.6	0.7	0.17	3
179803	0.7	0.3	10	29	13	216	281	142	1.1	1.5	20.7	0.25	98	30	20.9	0.4	6.9	3.7	113	18.9	0.7	0.25	3
179789	0.4	-0.1	145	172	27	174	62	119	0.7	1.4	24.4	0.62	94	137	18.8	0.5	8.6	3.2	112	27.4	0.4	-0.1	3
179790	2.0	0.5	162	149	33	321	253	139	1.2	2.3	30.1	0.59	14	30	16.2	0.6	9.4	3.9	142	29.1	2	0.49	8
179785	2.8	0.6	32	24	33	250	10	98	1.2	1.9	14.5	0.45	76	197	19.6	0.7	9.9	4.8	203	31	2.8	0.63	4
179782	2.7	0.7	13	19	27	175	23	160	0.7	1.8	2.2	0.75	40	136	19.4	0.8	11.7	5.3	212	36.2	2.7	0.68	4
179780	1.4	0.4	207	90	35	245	21	137	0.6	2	15.8	0.47	51	107	19.1	0.5	7.8	2.6	120	27.2	1.4	0.36	5
179776	3.9	1.0	171	80	26	175	8	100	0.8	1.9	24.2	0.68	78	171	18.1	0.5	7.5	3	135	30.7	3.9	0.99	5
179772	0.6	0.1	132	61	46	351	10	148	0.2	1.6	1.5	0.07	37	104	20.4	0.3	4.8	2.5	100	39.2	0.6	0.12	5
179770	0.9	0.2	128	65	42	323	8	124	0.8	1.3	2.3	0.05	93	75	17.9	0.3	3.9	3.1	106	28	0.9	0.21	5
179767	0.3	-0.1	189	108	47	316	20	112	0.4	1.1	3.6	0.06	49	113	16	0.2	2.6	1.9	64	23.4	0.3	-0.1	4
179766	0.3	-0.1	188	94	46	298	9	125	1	1.2	1.6	0.06	41	91	15.3	0.1	2.2	1.5	48	17	0.3	-0.1	4
179768	0.3	-0.1	229	113	49	326	27	100	0.7	1.1	15.9	0.21	41	110	15.5	0.2	2.5	1.7	58	21.6	0.3	-0.1	3
179769	0.3	-0.1	424	156	44	298	48	100	0.6	1.1	2.3	0.22	50	99	13	0.2	2.5	1.7	58	19.5	0.3	-0.1	4
179765	0.3	-0.1	178	89	47	305	16	133	1.3	1.4	2.8	0.06	94	125	15.4	0.1	2.3	1.4	48	17.9	0.3	-0.1	3
179764	0.5	0.1	197	89	42	303	99	114	0.8	1	5.6	0.12	64	147	15.9	0.2	3	1.7	58	18.1	0.5	0.12	4
179763	0.5	0.1	309	110	53	339	65	228	0.5	0.9	8.6	2.87	24	56	17.4	0.3	4.3	2.6	92	14.8	0.5	0.11	5
179762	0.4	0.1	268	92	41	277	17	120	0.6	1.2	9	0.23	41	140	17.1	0.3	3.7	2	75	19.8	0.4	0.11	5
179760	0.8	0.2	131	60	43	322	11	166	0.7	1.4	3.5	0.07	37	96	18.3	0.3	5.1	3	105	27.4	0.8	0.18	3
179759	0.6	0.1	251	113	47	341	49	103	0.8	1.2	8.4	0.32	32	101	18.7	0.3	4.6	2.5	91	23.1	0.6	0.11	2
179758	0.5	0.1	85	33	46	278	70	165	0.6	1.5	-1	0.09	36	116	18.6	0.3	4.5	2.7	95	27.5	0.5	0.14	7
179753	0.6	0.1	185	74	46	361	11	178	0.7	1.3	36.8	0.37	4810	100	18	0.3	4.5	2.9	97	28.5	0.6	0.14	2
179754	0.7	0.2	157	72	46	333	10	159	0.8	1.4	16.7	0.19	294	80	18.2	0.3	5	3.1	112	27.6	0.7	0.17	4
179752	0.4	0.1	2223	571	35	218	35	115	0.9	1.5	14.2	1.27	86	71	12.7	0.1	2.2	1.3	46	14.8	0.4	0.13	4
179787	4.8	1.0	43	36	17	107	8	68	0.8	2.4	27.9	1.69	185	226	20.4	0.8	12.9	5.6	257	36	4.8	0.99	6
179779	5.8	1.3	80	55	15	92	7	80	0.3	1.3	21	1.02	176	187	19.2	0.6	9	4.1	192	29.6	5.8	1.28	5
179757	-0.1	-0.1	5034	1589	23	100	3	55	0.6	0.9	-1	0.04	25	23	4.7	-0.1	0.4	0.3	11	3.7	-0.1	-0.1	2
179756	-0.1	-0.1	4699	1286	25	99	-1	54	1.2	0.9	-1	0.07	18	53	5.2	-0.1	0.6	0.4	14	4.8	-0.1	-0.1	3
179755	-0.1	-0.1	3636	1005	27	112	45	58	0.5	1	-1	0.12	26	33	6.2	-0.1	0.7	0.5	16	5.6	-0.1	-0.1	2
179751	0.2	-0.1	3811	830	31	160	151	123	1.2	1.1	-1	0.2	38	45	7.8	-0.1	1.2	0.8	26	8.7	0.2	-0.1	3

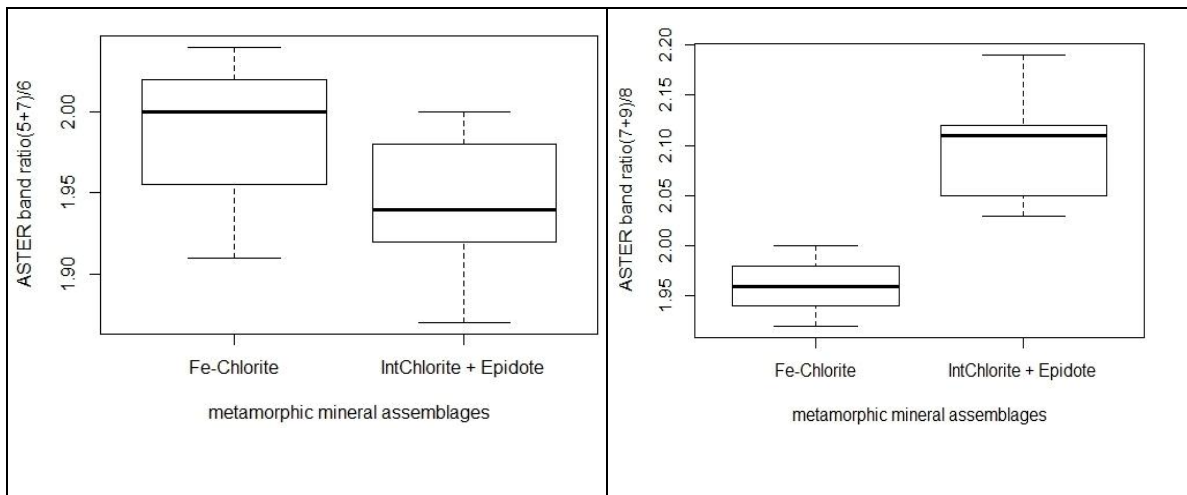
Duffer formation

Appendix 4: Potassium value and ASTER band ratio values variability with lithology



Appendix 4B: Potassium value and ASTER band ratio values variability with metamorphism





Appendix 5: Comparison of lithology from geological map and lithology from petrographic classification of Duffer Formation (Lith_geol_Map stands for lithology from geological map and Lith-Petro stands for lithology from petrographic classification)

Sample	Easting	Northing	Lith_geol	Litho_geoc	Matching	score
179726	804358	7680233	Andesite to Dacite	Rhyolite	similar	77%
179725	804395	7680881	basalt & dolerite	Basalt	matching	
179724	804427	7681032	Andesite to Dacite	Rhyolite	similar	
179723	804443	7681374	Dacite to Andesite	Dacite	matching	
179720	804838	7682147	Dacite to Andesite	Andesite	matching	
179716	804846	7682829	Dacite to Andesite	Dacite	matching	
179718	804753	7682544	Dacite to Andesite	Andesite	matching	
179722	804597	7681660	basalt	Andesite	not matching	
179714	804895	7682991	Dacite to Andesite	Andesite	matching	
179715	804891	7682940	Dacite to Andesite	Basalt	not matching	
179721	804612	7681754	Felsic tuff, graywacke, chert	Dacite	similar	
179717	804753	7682544	Dacite to Andesite	Basalt	not matching	
179719	804834	7682475	Dacite to Andesite	Andesite	matching	

Appendix 6 XRF laboratory data

Duffer Tractsect Data

Sample_No	Switties MR	EW-Cor	MS-Cor	Litho_geol_map	Mineral 1	Mineral 2	Mineral assemblage	Metamorphic grade	Lithology Alteration	CCPI Index	K from XRF	K Y-Ray	Th Y-Ray	Th XRF	U Y-Ray	U XRF	Magnetic Susceptibility	Bad Ratio_4	
19726	NONE	804358	7680233	Andesite to Diacite	Phengite	InChlorite	Fe-Chlorite	Greenschist	Phyllosite	29.21	618	0.86	6.37	9.6	1.47	2.44	None	88.86	
19725	B:004/107	804335	7680381	basalt & dolomite	Fe-Chlorite	NULL	Fe-Chlorite	Greenschist	Basalt	35.71	88.24	0.04	11	7.63	0.7	1.26	0.39	94.84	
19724	B:004/108	804427	7681032	Andesite to Diacite	Phengite	InChlorite	Fe-Chlorite	Greenschist	Phyllosite	33.93	24.18	1.08	1.04	6.57	10.4	1.06	2.74	5.49	96.80
19723	B:004/109	804443	7681574	Dolite to Andesite	InChlorite	Phengite	InChlorite + Epidote	Greenschist	Diacite	19.59	50.65	0.54	1.3	6.41	3	1.09	0.71	0.25	100.82
19720	B:004/104	804638	7682147	Dolite to Andesite	InChlorite	Epidote (v. little)	InChlorite + Epidote	Greenschist	Andesite	30.16	61.8	0.14	1.08	6.69	5.5	1.24	1.29	0.41	102.82
19716	B:004/112	804846	7682823	Dolite to Andesite	InChlorite	Epidote	InChlorite + Epidote	Greenschist	Diacite	29.88	52.37	0.55	0.88	6.29	6.8	0.95	1.54	0.18	103.80
19718	NONE	804755	7682544	Dolite to Andesite	InChlorite	Epidote (v. little)	InChlorite + Epidote	Greenschist	Andesite	53.03	81.49	0.42	1.31	8.32	5.4	1.24	0.97	None	100.82
19722	B:004/110	804537	7681660	basalt	InChlorite	Epidote	InChlorite + Epidote	Greenschist	Andesite	33.24	72.98	0.56	1.86	5.62	6.3	1.1	1.25	2.06	93.81
19714	B:004/105	804895	7682391	Dolite to Andesite	InChlorite	NULL	InChlorite + Epidote	Greenschist	Andesite	35.16	65.70	0.65	0.7	4.79	4.8	0.82	1.01	0.11	103.79
19715	B:004/113	804891	7682340	Dolite to Andesite	InChlorite	NULL	InChlorite + Epidote	Greenschist	Basalt	39.84	81.39	0.04	0.79	5.3	3.3	0.85	0.57	0.20	105.82
19721	B:004/111	804612	7681754	Felsic tuff/graywacke, chert	Phengite	InChlorite (v. little)	InChlorite + Epidote	Greenschist	Diacite	40.84	49.88	1.19	1.94	4.33	7.7	1.05	1.85	0.07	97.83
19717	B:004/102	804753	7682544	Dolite to Andesite	InChlorite	NULL	InChlorite + Epidote	Greenschist	Basalt	36.54	80.08	0.38	1.31	8.32	2.6	1.24	0.54	0.49	100.82
19719	B:004/103	804834	7682475	Dolite to Andesite	InChlorite	Epidote	InChlorite + Epidote	Greenschist	Andesite	43.13	66.13	1.15	1.32	8.04	5.2	1.17	1.13	0.29	113.82

Sample_No	Lithology petrography	SiO2	TiO2	Al2O3	MgO	CaO	Fe2O3	FcO	MnO	K2O	P2O5	LOI Total	LOI free	Total	
19726	Phyllosite	70.77	0.31	12.30	0.53	2.12	3.73	2.57	0.06	4.74	0.05	97.52	2.54	100.06	
19725	Basalt	47.17	2.17	12.30	5.15	7.59	15.99	11.03	0.19	1.85	0.10	92.70	8.40	101.10	
19724	Phyllosite	73.73	0.25	12.59	0.43	1.28	2.71	1.87	0.05	4.61	0.04	98.28	1.71	100.00	
19723	Diacite	60.79	0.70	18.28	1.22	6.50	5.97	4.12	0.10	3.89	0.14	96.89	3.28	100.16	
19720	Andesite	58.10	0.77	15.68	3.81	4.25	7.54	5.20	0.16	5.37	0.35	96.20	4.14	100.34	
19716	Dacite	53.95	0.67	15.94	2.77	4.65	6.06	4.18	0.09	4.99	1.34	96.61	3.59	100.20	
19718	Andesite	54.41	0.94	14.42	7.88	5.53	10.01	6.91	0.15	2.35	1.02	96.85	3.53	100.39	
19722	Andesite	56.50	1.14	15.56	3.12	6.31	11.18	7.71	0.14	2.67	1.34	96.19	2.14	100.33	
19714	Andesite	52.41	1.13	15.30	3.94	6.13	9.87	6.80	0.17	4.04	1.57	94.77	5.63	100.39	
19715	Basalt	48.31	1.16	14.41	6.83	7.15	11.75	8.10	0.20	3.31	0.10	93.36	7.36	100.72	
19721	Dacite	65.20	0.53	13.39	1.44	4.50	4.61	3.18	0.10	1.76	2.88	0.11	94.51	5.54	100.05
19717	Basalt	49.31	1.38	14.90	4.56	6.94	13.51	9.32	0.20	2.55	0.91	94.43	6.32	100.75	
19719	Andesite	54.41	1.02	16.10	4.18	6.72	8.88	5.99	0.14	2.45	2.77	96.68	3.39	100.07	

Sample_No	Lithology petrography	Cr	Ni	Sc	Y	Cu	Zn	Mo	Sn	Rb	Cs	Ba	Sr	Ga	Ta	Nb	Hf	Zr	Y	Pb
19726	Phyllosite	12	9	8	-3	4	49	14	1.9	51.6	1.38	802	126.6	19.1	1.1	14.9	9	316	42.4	7
19725	Basalt	48	56	41	503	109	101	0.7	1.6	-1	0.3	1001	193.1	19.1	0.5	6.8	4.5	146	33.4	7
19724	Phyllosite	9	10	5	-3	5	66	0.9	2.5	61.7	1.26	768	151.8	17.1	1.3	15.9	10.6	315	44.5	13
19723	Dacite	12	18	8	76	25	72	1.1	1.7	34.3	1.85	406	507.3	19.7	0.5	6.3	4	133	15.4	9
19720	Andesite	116	87	14	121	87	182	0.9	1.6	4.3	0.45	239	360.4	18.6	0.4	5.2	3.6	190	16.7	15
19716	Dacite	55	64	10	99	51	80	1.5	1.7	24.8	0.86	539	438.3	19	0.4	5.4	3.8	141	15.3	9.9
19718	Andesite	265	214	15	116	20	103	0.4	1.4	25.3	0.92	498	553.2	17.3	0.3	3.4	2.7	92	14.6	15
19722	Andesite	6	31	18	167	101	92	1.2	1.5	22	0.61	1015	647.3	19.8	0.5	7.7	4.3	147	26.5	13
19714	Andesite	77	48	22	202	53	94	0.8	1.4	26.8	1.33	1294	363.8	17.2	0.4	6.1	3.5	119	20.1	8.9
19715	Basalt	382	131	23	222	50	109	0.7	1.6	-1	0.39	173	334.1	17.4	0.2	3.7	2.5	82	18.8	5.4
19721	Dacite	4	12	7	38	18	78	2.8	3.2	107.1	4.85	1124	312.6	18.1	0.8	11.7	8.5	281	37.8	16
19717	Basalt	14	21	19	329	51	112	0.6	2.3	20.4	0.74	510	606.2	19.7	0.3	5.3	3	97	24.7	8.3
19719	Andesite	71	54	18	149	41	82	0.9	1.4	62.2	1.43	1960	839.5	17.9	0.4	6.3	3.3	120	18.9	12

Panorama Formation

Appendix 7: XRF laboratory data

SAMPLE	AI	CCPI	LITHOLOGY	TSA_Minera	SiO2	TiO2	Al2O3
203310	96.37	94.70	dacite	IntChlorite	64.25	0.55	9.21
207116	94.44	98.87	andesite	FeChlorite	63.68	0.84	11.50
207118	96.74	99.27	andesite-basalt	FeChlorite	57.60	1.46	11.71
207119	91.56	99.10	andesite-basalt	FeChlorite	58.45	1.49	11.38
207122	89.76	92.94	andesite	IntChlorite	67.90	0.82	11.26
207123	95.67	98.29	andesite-basalt	FeChlorite	60.83	1.36	11.39
207124	95.08	97.16	andesite-basalt	FeChlorite	59.11	1.50	11.80
207125	94.19	93.22	andesite	FeChlorite	62.52	0.90	12.11
207126	92.11	97.99	andesite-basalt	FeChlorite	62.16	1.41	10.65
207127	93.63	96.62	andesite-basalt	FeChlorite	59.15	1.63	11.48
207128	93.68	99.00	andesite-basalt	FeChlorite	56.64	1.63	11.73
207129	97.87	98.58	andesite-basalt	IntChlorite	57.21	1.50	12.31
207132	93.42	93.86	andesite	IntChlorite	64.34	0.87	11.78
207133	94.19	98.55	andesite-basalt	FeChlorite	60.89	1.53	11.46
207134	97.01	97.62	andesite-basalt	FeChlorite	60.37	1.48	11.59
207135	95.13	96.88	andesite-basalt	FeChlorite	59.09	1.50	11.67
207136	94.99	93.50	andesite-basalt	FeChlorite	58.58	1.61	12.48
207137	93.09	96.24	andesite-basalt	FeChlorite	60.51	1.49	11.41
207138	92.33	97.22	andesite-basalt	FeChlorite	61.61	1.35	10.85
207142	94.96	96.96	andesite-basalt	FeChlorite	61.74	1.32	11.28
207228	97.21	78.96	dacite	IntChlorite	71.94	0.56	11.00
207231	94.74	52.36	dacite	Muscovite	75.61	0.74	11.58
207232	97.60	86.16	dacite	IntChlorite	69.97	0.69	11.01
207233	97.46	86.84	dacite	IntChlorite	67.47	0.85	11.25
207493	94.58	93.67	andesite	FeChlorite	64.86	0.82	11.29
207497	94.52	81.44	andesite	FeChlorite	65.40	0.90	13.30

Continued

SAMPLE	Fe ₂ O ₃ (tot)	MnO	MgO	CaO	Na ₂ O	K ₂ O	P ₂ O ₅
203310	10.83	0.07	6.93	0.27	0.02	0.64	0.13
207116	11.16	0.03	6.35	0.35	0.03	0.10	0.28
207118	16.13	0.08	6.43	0.21	0.01	0.09	0.23
207119	16.94	0.06	5.54	0.50	0.02	0.10	0.43
207122	8.99	0.01	4.91	0.27	0.33	0.35	0.22
207123	13.33	0.07	6.64	0.30	0.01	0.21	0.24
207124	15.53	0.07	6.03	0.30	0.03	0.35	0.24
207125	12.02	0.03	5.73	0.34	0.06	0.75	0.28
207126	13.47	0.06	5.63	0.47	0.03	0.21	0.39
207127	15.12	0.07	6.06	0.40	0.04	0.41	0.33
207128	16.48	0.08	6.39	0.43	0.01	0.13	0.39
207129	14.50	0.06	8.06	0.17	0.01	0.20	0.14
207132	10.82	0.03	5.84	0.30	0.15	0.55	0.26
207133	12.55	0.05	7.28	0.45	0.01	0.18	0.36
207134	13.30	0.05	7.14	0.22	0.01	0.31	0.18
207135	15.67	0.08	5.68	0.28	0.03	0.38	0.23
207136	14.65	0.08	5.63	0.31	0.03	0.82	0.23
207137	14.52	0.07	5.75	0.43	0.03	0.45	0.35
207138	13.99	0.05	5.59	0.46	0.03	0.31	0.37
207142	13.41	0.07	6.41	0.34	0.02	0.37	0.26
207228	5.97	0.06	4.22	0.04	0.13	1.71	0.05
207231	2.96	0.01	2.02	0.25	0.03	3.02	0.21
207232	7.59	0.04	4.80	0.12	0.03	1.29	0.09
207233	8.38	0.09	5.20	0.14	0.03	1.33	0.12
207493	11.12	0.05	5.80	0.30	0.07	0.66	0.22
207497	10.32	0.06	3.65	0.30	0.02	1.87	0.22

LIST OF REFERENCES

- Abweny, M. S. M. (2012). *Near infrared spectroscopy of low grade metamorphic volcanic rocks of the east Pilbara granite greenstone terrane Australia*. MSc Thesis, University of Twente Faculty of Geo-Information and Earth Observation ITC, Enschede. Retrieved from http://www.itc.nl/library/papers_2012/msc/aes/abweny.pdf
- Be´dard, J. H. (2006.). A catalytic delamination-driven model for coupled genesis of Archaean crust and sub-continental lithospheric mantle. *Geochim. Cosmochim. Acta*, 70, 1188–1214.
- Blake, T. S. (2001). Cyclic continental mafic tuff and flood basalt volcanism in the Late Archaean Nullagine and Mount Jope Supersequences in the eastern Pilbara, Western Australia: Precambrian Research. 107 139–177.
- Blewett, R. S., & Champion, D. C. (2005). Geology of the Wodingna 1:100 000 Sheet: Western Australia Geological Survey, 1:100 000, Geological Series Explanatory Notes. 33.
- Brauhart, C. W. (1999). Regional alteration systems associated with Archean volcanogenic massive sulfide mineralization at Panorama, Pilbara, Western Australia: Unpublished Ph.D. thesis, Nedlands, WA, University of Western Australia. 194.
- Brauhart, C. W., Groves, D. I., & Morant, P. (1998). Regional alteration systems associated with volcanogenic massive sulfide mineralization at Panorama, Pilbara, Western Australia. *Economic Geology and the Bulletin of the Society of Economic Geologists*, 93(3), 292-302.
- Brauhart, C. W., Huston, D. L., Groves, D. I., Mikucki, E. J., & Gardoll, S. J. (2001). Geochemical mass-transfer patterns as indicators of the architecture of a complete volcanic-hosted massive sulfide hydrothermal alteration system, Pnorama District, Pilbara, Western Australia. *Economic Geology*, 96, 1263-1278.
- Brown, A. J., Cudahy, T. J., & Walter, M. R. (2006). Hydrothermal alteration at the Panorama Formation, North Pole Dome, Pilbara Craton, Western Australia. *Precambrian Research*, 151(3–4), 211-223. doi: 10.1016/j.precamres.2006.08.014
- Buick, R., Brauhart, C. W., Morant, P., Thornett, J. R., Maniw, J. G., Archibald, N. J., . . . Groves, D. I. (2002). Geochronology and stratigraphic relationships of the Sulphur Springs Group and Strelley Granite: a temporally distinct igneous province in the Archaean Pilbara Craton, Australia *Precambrian Research*, 114, 87–120.
- Cawood, P. A., Kroner, A., & Pisarevsky, S. (2006). Precambrian plate tectonics: criteria and evidence *GSA Today*, 16, 4–11.
- Cudahy, T. J., Okada, K., & Brauhart, C. (2000). Targeting VMS-style Zn mineralization at Panorama, Australia, using airborne hyperspectral VNIR-SWIR HyMap data. In: Environmental Research Institute of Michigan, International Conference on Applied Geologic Remote Sensing, 14th Las Vegas, Nevada, Proceedings. 395–402.
- Cullers, R. L., Dimarco, M. J., Lowe, D. R., & Stone, J. (1993). Geochemistry of a Silicified, Felsic Volcaniclastic Suite from the Early Archean Panorama Formation, Pilbara Block, Western Australia—an Evaluation of Depositional and Postdepositional Processes with Special Emphasis on the Rare-Earth Elements. *Precambrian Research* 60, 99–116.
- Davies, G. F. (1995). Punctuated tectonic evolution of the Earth. *Earth Planet. Sci.Lett.*, 36, 363–380.
- Davis, C., Wijbrans, J. R., & White, S. H. (1997). 40Ar/39Ar laserprobe ages of metamorphic hornblendes from the Coongan Belt, Pilbara, Western Australia: . *Precambrian Research*,, 83, 221–242.
- de Wit, M. J. (1998.). On Archean granites, greenstones, craton and tectonics: does the evidence demand a verdict? *Precambrian Res.*, 91, 181–226.
- Erdi-Krausz, G., Matolin, M., Minty, B., Nicolet, J. P., Reford, W. S., & Schetselaar, E. M. (2003). *Guidelines for radioelement mapping using gamma ray spectrometry data : also as e-book* (Vol. 1363). Vienna: International Atomic Energy Agency (IAEA).
- Glikson , A. Y., & Hickman, A. H. (1981). Geochemistry of Archaean volcanic successions, Eastern Pilbara Block, Western Australia: Australia BMR. (86/14), 83.
- Gomez, C., Delacourt, C., Allemand, P., Ledru, P., & Wackerle, R. (2005). Using ASTER remote sensing data set for geological mapping, in Namibia. *Physics and Chemistry of the Earth, Parts A/B/C*, 30(1–3), 97-108. doi: 10.1016/j.pce.2004.08.042

- Gozzard, J. R. (2006). Image processing of ASTER multispectral data: Western Australia Geological Survey, Record 2006/9. 51.
- Green, M. G., Sylvester, P. J., & Buick, R. (2000). Growth and recycling of early Archaean continental crust: geochemical evidence from the Coonterunah and Warrawoona Groups, Pilbara Craton, Australia: *Tectonophysics*, 322, 69–88.
- Hamilton, W. B. (2003). An alternative Earth. *GSA Today*, 13, 4–12.
- Hickman, A. H. (1977). New and revised definitions of rock units in the Warrawoona Group, Pilbara Block: Western Australia Geological Survey, Annual Review 1976 53
- Hickman, A. H. (1983). Geology of the Pilbara Block and its environs: Western Australia Geological Survey, Bulletin 127. 268.
- Hickman, A. H. (1990). Geology of the Pilbara Craton, in Third International Archaean Symposium, Perth, 1990. Excursion Guidebook No. 5: Pilbara and Hamersley Basin, edited by S. E. HO, J. E. Glover, J. S. Myers, and J. R. Muhling: University of Western Australia, Geology Department and University Extension, Publication, no. 21. 2–13.
- Hrouda, F., Chlupacova, M., & Chadima, M. (2009). The use of magnetic susceptibility of rocks in geological exploration. *Terraplus Geophysical Equipment Supplier*, 25.
- Ishikawa, Y., Sawaguchi, T., Iwaya, S., & M, H. (1976). Delineation of prospecting targets for Kuroko deposits based on modes of volcanism of underlying dacite and alteration haloes. *Min Geol.*, v26, 105-117.
- Kumar, P. T. K., Phoha, V. V., & Iyengar, S. S. (2008). Classification of radio elements using mutual information: A tool for geological mapping. *International Journal of Applied Earth Observation and Geoinformation*, 10(3), 305-311. doi: 10.1016/j.jag.2007.12.001
- Large, R. R., Gemmel, J. B., Paulick, H., & Huston, D. L. (2001). The alteration box plot: A simple approach to understanding the relationship between alteration mineralogy and litho-geochemistry associated with volcanic-hosted massive sulfide deposits. *Economic Geology and the Bulletin of the Society of Economic Geologists*(96(5)), 957-971.
- Lipple, S. L. (1975). Definitions of new and revised stratigraphic units of the eastern Pilbara Region: Western Australia Geological Survey, Annual Report 1974. 58–63.
- Parsons, S., Nadeau, L., Keating, P., & Chung, C.-J. (2006). Optimizing the use of aeromagnetic data for predictive geological interpretation: an example from the Grenville Province, Quebec. *Computers & Geosciences*, 32(5), 565-576. doi: 10.1016/j.cageo.2005.07.007
- Piche, M., & Jebrak, M. (2004). Normative minerals and alteration indices developed for mineral exploration. *Journal of Geochemical Exploration*, 82(1-3), 59-77.
- Reeves, C. (2005). Aeromagnetic surveys principles, practice & interpretation. 155.
- Richardson, L. M. (1996). Marble Bar (Marble Bar, Western Port Hedland, Eastern Roebourne and North Eastern Pyramid 1:250 000 Sheet areas) airborne geophysical survey. [Operations report]. *Australian Geological Survey Organisation*, 1997/63(1997/63), 61.
- Smithies, R. H., Champion, D. C., & Cassidy, K. F. (2003). Formation of Earth's early Archaean continental crust. *Precambrian Res.* (Vol. 127 pp. 89–101).
- Smithies, R. H., Champion, D. C., Van Kranendonk, M. J., & Hickman, A. H. (2007). Geochemistry of Volcanic rocks of the northern Pilbara Craton, Western Australia. *Geological Survey of Western Australia* 104, 47.
- Stern, R. J. (2005). Evidence from ophiolites, blueschists, and ultrahigh-pressure metamorphic terranes that the modern episode of subduction tectonics began in Neoproterozoic time. *Geology*, 33, 557–560.
- Theart, H. F. J., Ghavami-riabi, R., & Graser, P. (2011). Applying the box plot to the recognition of footwall alteration zones related to VMS deposits in a high-grade metamorphic terrain, South Africa, a litho-geochemical exploration application. *Chemie der Erde-Geochemistry*, 71(2), 143-154.
- Trendall, A. F. (1990). Pilbara Craton — introduction, in Geology and mineral resources of Western Australia: Western Australia Geological Survey, Memoir 3 128.
- Turner, F. J. (1981). *Metamorphic petrology*: New York, U.S.A., McGraw-Hill. 524.
- Van Kranendonk, M. J. (2004a). Archaean tectonics 2004: a review. *Precambrian Res.*, 131, 143–151.
- Van Kranendonk, M. J., Hickman, A. H., Smithies, R. H., Nelson, D. R., & Pike, G. (2002). Geology and tectonic evolution of the Archaean North Pilbara terrain, Pilbara Craton, Western Australia. *Economic Geology*, 97, 695–732.

- Van Kranendonk, M. J., Hickman, A. H., Smithies, R. H., Williams, I. R., Bagas, L., & Farrell, T. R. (2006). *Revised lithostratigraphy of archean supracrustal and intrusive rocks in the Northern Pilbara craton, Western Australia* (Vol. 2006-15). Perth: Geological Survey of Western Australia.
- Van Kranendonk, M. J., Hugh Smithies, R., Hickman, A. H., & Champion, D. (2007). secular tectonic evolution of Archean continental crust: interplay between horizontal and vertical processes in the formation of the Pilbara Craton, Australia. [Review]. *Terra nova : the European journal of geosciences*, 19(1), 1-38.
- Van Kranendonk, M. J., & Pirajno, F. (2004). Geological setting and geochemistry of metabasalts and alteration zones associated with hydrothermal chert ± barite deposits in the ca. 3.45 Ga Warrawoona Group, Pilbara Craton, Australia. *Geochemistry, Exploration, Environment, Analysis*, 4, 253-278.
- Van Kranendonk, M. J., Smithies, R. H., Hickman, A. H., & Champion, D. (2007). Secular tectonic evolution of Archean continental crust : interplay between horizontal and vertical processes in the formation of the Pilbara Craton, Australia. *Journal Terra nova : the European journal of geosciences*, 19(1), 1-38.
- Van Ruitenbeek, F. J. A., Cudahy, T. J., van der Meer, F. D., & Hale, M. (2012). Characterization of the hydrothermal systems associated with Archean VMS-mineralization at Panorama, Western Australia, using hyperspectral, geochemical and geothermometric data. *Ore Geology Reviews*, 45, 33-46. doi: 10.1016/j.oregeorev.2011.07.001
- Van Kranendonk, M. (2006). Volcanic degassing, hydrothermal circulation and the flourishing of early life on Earth: A review of the evidence from c. 3490–3240Ma rocks of the Pilbara Supergroup, Pilbara Craton, Western Australia. *Earth Science Reviews*, 74, 197–240.
- Van Kranendonk, M. J. (2000). Geology of the North Shaw 1:100 000 sheet: Western Australia Geological Survey, 1:100 000, Geological Series Explanatory Notes 86.
- Van Kranendonk, M. J. (2000). Geology of the North Shaw 1:100 000 sheet: Western Australia Geological Survey, 1:100 000, Geological Series Explanatory Notes. 86.
- Zegers, T. E., Wijbrans, J. R., & White, S. H. (1999). ⁴⁰Ar/³⁹Ar age constraints on tectonothermal events in the Shaw area of the eastern Pilbara granite–greenstone terrain (W Australia): 700 Ma of Archean tectonic evolution *Tectonophysics*, 311, 45–81.